

ALTERATION OF THE BOOTSTRAP LIMESTONE, NORTHERN CARLIN TREND,  
ELKO COUNTY, NEVADA

by

Catherine E. Morgan

A thesis submitted to the Faculty and the Board of Trustees of the Colorado  
School of Mines in partial fulfillment of the requirements for the degree of Master of  
Science (Geology).

Golden, Colorado

Date \_\_\_\_\_

Signed: \_\_\_\_\_  
Catherine E. Morgan

Signed: \_\_\_\_\_  
Dr. John D. Humphrey  
Thesis Advisor

Golden, Colorado

Date \_\_\_\_\_

Signed: \_\_\_\_\_  
Dr. John D. Humphrey  
Professor and Interim Head  
Department of Geology and  
Geological Engineering

## ABSTRACT

The Silurian-Devonian Bootstrap limestone unit hosts Carlin-type gold deposits. Although the structural controls for Carlin-type gold deposits can vary significantly, ore bodies located in the Bootstrap limestone occur predominately in silicified breccias. The objectives of this study were to describe in detail the alteration in the Bootstrap limestone, determine paragenesis of the different alteration events, and identify the pattern of alteration surrounding Bootstrap-hosted deposits. The objectives were met through detailed logging of drill-hole cores, as well as standard petrography, cathodoluminescence microscopy, and stable isotopic analysis.

The study area focuses on the northern Carlin trend, located approximately 27 miles (43 km) northwest of Carlin, NV. This area includes the deposits of Meikle, Ren, Dee-Rossi (Storm), and South Arturo. The relevant stratigraphy in the area consists of the massive Bootstrap limestone platform unit and the time-equivalent Roberts Mountains Formation and slope and basinal facies of the Popovich Formation.

Six major carbonate components of the Bootstrap limestone were recognized in the study area: limestone, diagenetic-planar dolomite, saddle dolomite, ferroan dolomite, zebra texture dolomite, and calcite. The limestone experienced pervasive early diagenetic calcite cementation that sharply lowered porosity and permeability of the unit. The resulting restriction of fluid flow resulted in a condensed sequence of later hydrothermal dolomitization.

The diagenetic-planar dolomite represents a regional dolomitization event that was localized along the lower contact of the Bootstrap limestone. The fluids necessary for dolomitization were probably sourced from compaction of the adjacent mud-rich Roberts

Mountains and Popovich Formations. The resulting dolostones extend from west of Meikle to the Ren area.

Non-planar saddle, ferroan, and zebra texture dolomites are the result of hydrothermal dolomitization. Curved boundaries of the dolomite crystals, associated sulfides, and calculated temperatures from isotopic data, support a hydrothermal source for these dolomites. Through cross cutting relationships between diagenetic planar dolomite and non-planar dolomites were not observed, the available evidence suggests non-planar dolomite post date planar dolomite. Non-planar, commonly ferroan dolomite at Meikle is spatially associated with a Paleozoic age base-metal mineralization event. Non-planar, generally non-ferroan at Storm and Dee-Rossi are spatially associated with Jurassic to Eocene intrusions suggesting they formed due to much later hydrothermal events. Thus, there are two possible generations of hydrothermal dolomite, one in the Paleozoic and another associated with Jurassic to Tertiary igneous activity.

In the study area, the complex nature of the breccia bodies and/or the permeability of the host rock limit the lateral extent of the carbonate alteration. However, based on the samples analyzed in this study, and recognition of the processes that form dolomite, a pattern of dolomitization can be predicted for Carlin-type deposits in this study area. Extending away from a fluid pathway, ferroan dolomite forms first, followed by saddle dolomite, which is in contact with unaltered limestone. Zebra texture dolomite forms at the transition between ferroan and saddle dolomites, or it can extend throughout the zone of ferroan dolomite. The dolomite zonation pattern, as well as the different generations of dolomite, should be considered in the exploration for Carlin-type deposits hosted in massive limestone units. Each dolomite generation may reflect the potential for gold

mineralization, with the Paleozoic iron-rich hydrothermal dolomite being the most favorable host.

## TABLE OF CONTENTS

ABSTRACT.....	iii
LIST OF FIGURES .....	viii
LIST OF TABLES.....	xi
ACKNOWLEDGMENTS .....	xii
INTRODUCTION .....	1
Objectives .....	3
Methods.....	3
GEOLOGIC BACKGROUND.....	5
Tectonic History.....	5
Stratigraphy .....	8
Structure .....	17
Paleozoic Mineralization Event .....	18
Cretaceous Mineralization Event.....	19
Tertiary Mineralization Event.....	20
Alteration .....	24
RESEARCH RESULTS .....	26
Limestone.....	26
Diagenetic-Planar Dolomite.....	31
Saddle Dolomite.....	41
Ferroan Dolomite .....	46
Zebra Dolomite .....	52
Calcite .....	59

DISCUSSION .....	67
Limestone Interpretation .....	67
Dolostone Interpretation .....	68
Saddle Dolomite and Ferroan Dolomite Interpretation .....	75
Zebra Texture Dolomite Formation .....	84
Calcite Generations .....	86
Generations of Silica Deposition .....	91
Hydrocarbon Migration .....	94
Paragenesis.....	94
Pattern of Dolomitization.....	97
SUMMARY AND CONCLUSIONS .....	104
REFERENCES CITED.....	109
APPENDIX A—GEOLOGIC MAP.....	117
APPENDIX B—DATA .....	118
APPENDIX C—CORE LOGS .....	127
APPENDIX D—STABLE ISOTOPE DATA .....	133

## LIST OF FIGURES

Figure 1: Location map of the Carlin trend .....	2
Figure 2: Summary of the tectonic history for western North America .....	6
Figure 3: Tectonostratigraphic column of the northern Carlin trend.....	9
Figure 4: Facies distribution map for the Bootstrap limestone.....	11
Figure 5: Cross section B-B' through the Bootstrap limestone shoal facies .....	12
Figure 6: Location of the study area along the northern Carlin trend.....	14
Figure 7: Cross sections across the Storm, Meikle, and South Arturo deposits .....	16
Figure 8: Genetic model for Carlin-type deposits.....	17
Figure 9: Map with the locations of drill holes.....	27
Figure 10: Core photo of Bootstrap limestone shoal facies.....	29
Figure 11: Photomicrographs of limestone.....	30
Figure 12: Cathodoluminescence photomicrograph of limestone .....	32
Figure 13: Isotopic data for limestone samples .....	33
Figure 14: Location map of drill holes with diagenetic-planar dolomite .....	34
Figure 15: Core photo of limestone and diagenetic-planar dolomite contact.....	35
Figure 16: Photomicrographs of diagenetic-planar dolomite .....	38
Figure 17: Cathodoluminescence photomicrographs of diagenetic-planar dolomite .....	39
Figure 18: Isotopic data for diagenetic-planar dolomite.....	40
Figure 19: Map with the locations of drill holes with saddle dolomite .....	42
Figure 20: Hand sample photos of saddle dolomite.....	43
Figure 21: Photomicrographs of saddle dolomite.....	44
Figure 22: Cathodoluminescence photomicrographs of saddle dolomite.....	45



Figure 23: Isotopic data for saddle dolomite .....	47
Figure 24: Location map of drill holes with ferroan dolomite.....	48
Figure 25: Hand sample photographs of ferroan dolomite .....	49
Figure 26: Photomicrograph of ferroan dolomite .....	50
Figure 27: Cathodoluminescence photomicrographs of ferroan dolomite .....	51
Figure 28: Isotopic data for ferroan dolomite .....	53
Figure 29: Location map of drill holes with zebra dolomite .....	54
Figure 30: Hand sample photographs of zebra dolomite .....	55
Figure 31: Photomicrographs of zebra dolomite .....	57
Figure 32: Cathodoluminescence photomicrographs of zebra dolomite .....	58
Figure 33: Isotopic data for zebra dolomite .....	60
Figure 34: Hand sample photograph of late calcite .....	61
Figure 35: Photomicrographs of late calcite .....	63
Figure 36: Cathodoluminescence photomicrographs of late calcite.....	65
Figure 37: Isotopic data for zebra texture dolomite.....	66
Figure 38: Isotopic data and associated photomicrographs for limestone.....	69
Figure 39: Burial compaction model for dolomitization .....	72
Figure 40: Schematic cross section of the dolostone horizon.....	75
Figure 41: Isotopic data and associated photomicrographs for diagenetic-planar dolomite.....	77
Figure 42: Isotopic data and associated photomicrographs for saddle dolomite .....	82
Figure 43: Isotopic data and associated photomicrograph for ferroan dolomite .....	83
Figure 44: Hand sample photo of Ex-21c, 1024', with saddle dolomite vein crossing ferroan dolomite .....	87

Figure 45: Isotopic data and associated photomicrographs for zebra dolomite.....	89
Figure 46: Photomicrographs of the white band in zebra dolomite.....	90
Figure 47: Isotopic data and associated photomicrographs for late calcite .....	93
Figure 48: Paragenetic sequence of the carbonate types .....	96
Figure 49: Map of the occurrences of different carbonate types .....	98
Figure 50: Schematic diagram of the pattern of hydrothermal dolomitization.....	100
Figure 51: Isotopic data averages for each carbonate type .....	102

## LIST OF TABLES

Table 1: Table of drill holes sampled and deposit descriptions for Meikle, Ren, Dee-Rossi, and South Arturo .....	28
Table 2: Summary of the three generations of dolomite and the common properties used for distinguishing each type.....	108

## ACKNOWLEDGEMENTS

I would like to thank the following individuals and companies for all the time and support they gave to me and this research:

- Dr. John D. Humphrey, my advisor, who not only taught me carbonate geology, but also how to enjoy graduate school, balance work and life, and that Friday afternoons are for postre.
- Dr. Murray W. Hitzman, my other advisor/committee member, thank you for setting up this project, your time in Nevada, and enthusiasm in working with students.
- Dr. Jeffrey W. Hedenquist, thank you for serving on my committee, your edits and comments greatly improved the final conclusions of this project.
- Barrick Gold Exploration, Inc. and Barrick Goldstrike Mines, Inc., without whose financial support and access to data, this project would not have been possible. In particular, I thank Paul Dobak for supporting this project and taking the time to get me started out at the mine, as well as Richard Hipsley, Bob Leonardson, John Katseanes, Al Lander, and Robert Malloy.
- Centerra Gold for providing access to core from the Ren deposit.
- Society of Economic Geologists, Hugh Exton McKinstry Fund, for providing financial support.
- The Department of Geology and Geological Engineering for financial assistance as well as an education beyond my expectations and to all the staff, including Debbie Cockburn, Marilyn Schwinger, Charlie Rourke, and John Skok.

- The graduate students, the undergraduate students, Jesse at Tequila's, and everyone who made graduate school fun.
- My parents for never questioning why I stayed in college 8 years and for giving me constant support.
- And especially Sean Horigan, whose friendship and love both aided and hindered my progress, but ultimately is the reason I finished.

## INTRODUCTION

The Carlin trend is a 60 km-long, northwest-trending linear alignment of approximately 42 disseminated gold deposits located in northeastern Nevada (Figure 1). The trend contains 5,000 Mt of gold and contributes ~9% of the world's annual gold production, with annual production of 4 M oz (Hofstra and Cline, 2000).

“Carlin-type” refers to sedimentary rock-hosted disseminated gold deposits. Though some deposits were mined in the early 1900s, this deposit type was first recognized with the 1961 discovery of the Carlin deposit. The deposits have a range of characteristics, including differing structural and stratigraphic controls. The variance between individual deposits in the trend results in varying Au tonnages and grades ranging from 100 t Au to >250 t Au (at >30 g/t), but Au deposits are also as small as 1 t Au or less (and grades as low as 1 g/t) (Cline et al., 2005).

There is evidence of three separate mineralization events in the northern Carlin trend, including a Paleozoic base-metal event with possible Au deposition, a Cretaceous porphyry related event, and the primary gold event that occurred from ~42 to 36 m.y. ago (Hofstra et al., 1999; Ressel et al., 2000; Arehart et al., 2003; Emsbo et al., 2003).

In the northern Carlin trend, calcareous rocks that comprise the Devonian-Silurian Roberts Mountains Formation and the Devonian Popovich Formation are the primary deposit hosts. Gold is typically associated with disseminated arsenic-rich pyrite. The alteration that extends laterally from these deposits through the carbonate host rocks is visually subtle. The intensity of the Au-bearing fluid interaction and porosity of the host rock control the extent of alteration (Cline et al., 2005).

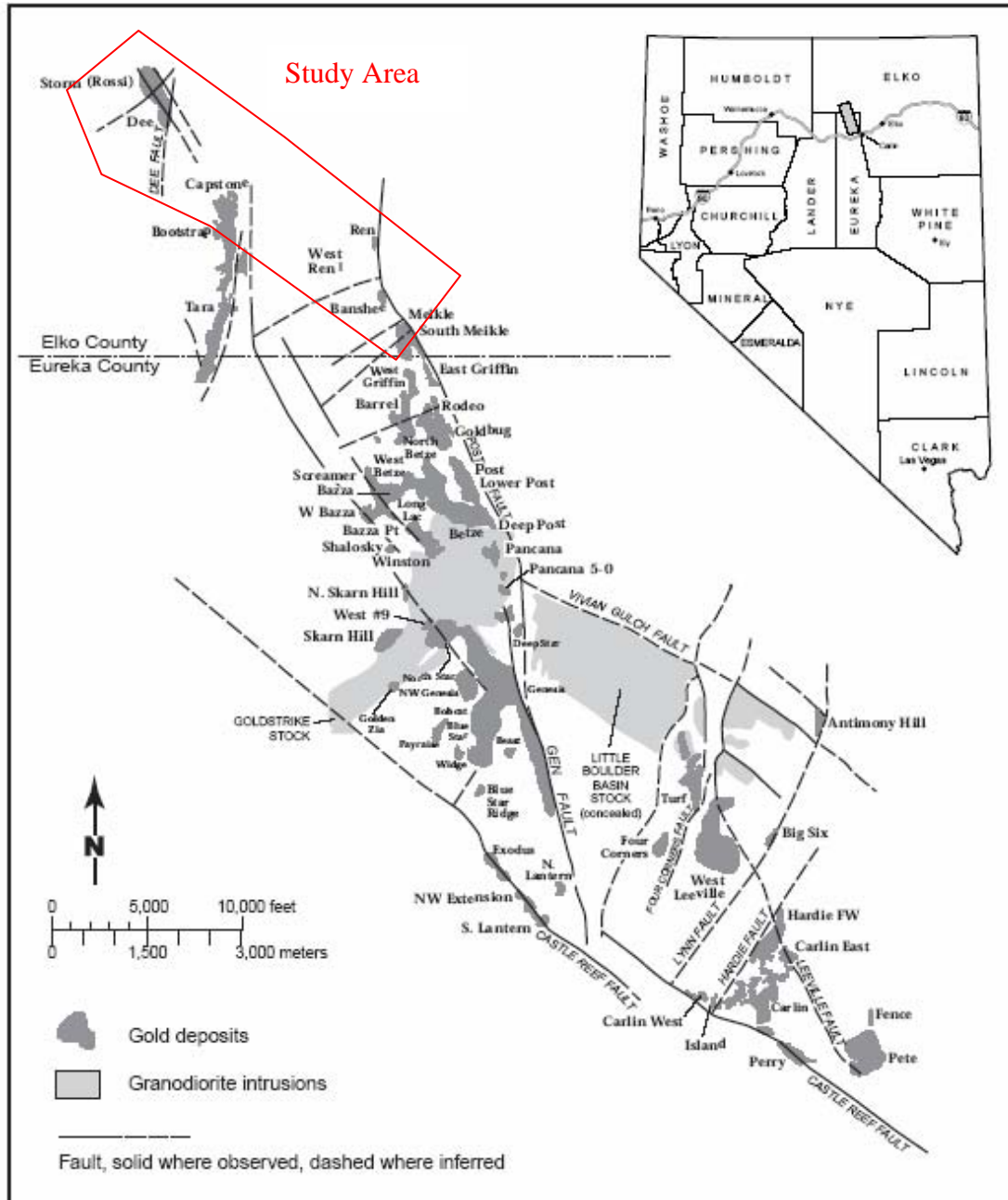


Figure 1: Location map of the Carlin Trend, Nevada showing deposit locations and fault occurrences. The study area is in Elko County and includes the Meikle, Ren and Dee-Rossi deposits (from Teal and Jackson, 2002).

The objective of this project is to describe the alteration associated with the pre- and syn-gold mineralization of the Bootstrap limestone subunit of the Roberts Mountains Formation, continuing the work on the Meikle deposit by Evans (2000). This project consists of detailed petrographic descriptions and isotopic analysis to describe and determine extent of the carbonate alteration in the Bootstrap limestone unit.

### **Objectives**

The objectives of this research are as follows:

- Describe the carbonate alteration in the Silurian-Devonian Bootstrap limestone (e.g., cementation, dolomitization, calcite precipitation, silicification)
- Determine the paragenesis of different alteration events and separate the Paleozoic and Tertiary events
- Identify alteration vectors for Carlin-type gold deposits in the Bootstrap limestone

### **Research Methods**

A combination of field and laboratory studies was used to meet the objectives of this project. Two summer field seasons, 2005 and 2006, were spent in the Barrick Exploration office in Elko, Nevada and at the Barrick Goldstrike Mine.

The fieldwork portion of this project involved the selection of drill holes that intersected Bootstrap limestone exhibiting varying alteration intensities. This included samples of Bootstrap limestone that were relatively fresh and unaltered, diagenetically dolomitized, and hydrothermally dolomitized. Seventeen drill holes were logged in detail and hand samples were collected for later petrographic analysis. Logging focused on identifying and sampling different areas of limestone and dolomite from the Bootstrap.



Carbonate staining of the core was employed to make field-based observations of carbonate composition.

The laboratory portion of the research consisted of petrographic and isotopic analysis. Ninety-seven thin sections were prepared and examined. Detailed petrographic descriptions utilizing standard transmitted light and cathodoluminescence microscopy were conducted. The detailed descriptions focused on the percentage, type, and texture of dolomite in the samples. Classification of the samples followed the carbonate rock classification scheme of Dunham (1962), and dolomite crystal fabrics were described using terminology of Sibley and Greg (1987).

Isotopic study was conducted on 78 samples from 11 drill holes. The samples represented limestone, diagenetic-planar dolomite, saddle dolomite, ferroan dolomite, light and dark bands of zebra texture dolomite, and late calcite. The isotopic data were used to separate and distinguish each carbonate phase. Approximately 90  $\mu\text{g}$  of carbonate was reacted on-line at 90°C and analyzed using traditional dual-inlet techniques on a GV Instruments IsoPrime mass spectrometer in the Colorado School of Mines Stable Isotope Laboratory. Standard ion corrections were made and data are reported as a per mil difference from the VPDB standard reference. External precision, based on blind duplicate samples is 0.05‰ for carbon and 0.08‰ for oxygen.

## GEOLOGIC BACKGROUND

### **Tectonic History**

The Carlin trend sits in an area with a complex geologic history. The tectonic events that occurred from the Proterozoic to Eocene (Figure 2) were responsible for developing the necessary fluid pathways and traps to form subsequent gold deposits in the region.

The early tectonic history includes rifting of the Archean and Proterozoic basement in the late Proterozoic (John et al., 2003). This rifting produced significant basement faults that served as the major controls on the north-northwest direction of the trend. Archean crust currently underlies the deposits in the northern Carlin trend (Tosdal et al., 2000).

A period of late Proterozoic rifting was followed by several compressional events associated with an east-dipping subduction zone from the middle Paleozoic to early Tertiary. The compressional events were related to the Antler, Humbolt, Sonoma, Nevadan, Elko, Sevier, and Laramide orogenies (John et al., 2003; Cline et al., 2005).

The late Devonian through early Mississippian Antler orogeny was responsible for forming the Roberts Mountains thrust. Eugeoclinal sedimentary rocks were thrust eastward onto sedimentary rocks of the continental shelf from the west (Roberts et al., 1958; Stewart, 1980), leading to the development of a foreland basin. The foredeep of the basin was filled with early Mississippian and Pennsylvanian sedimentary rocks (Poole et al., 1992).

Thrust faults are an important control on the location of deposits in the Carlin trend. Most giant deposits in the trend are found within 100 m of a thrust or its projection

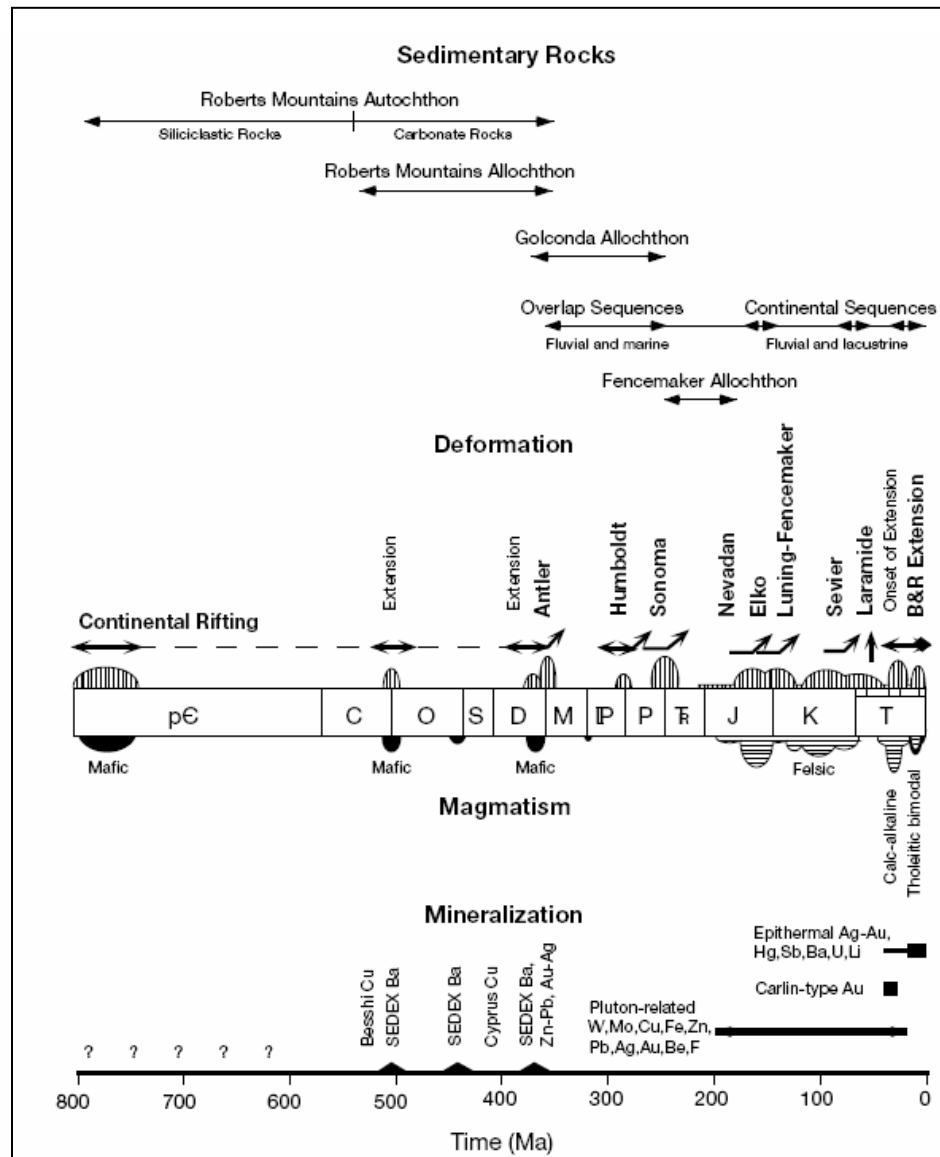


Figure 2: Summary of the tectonic history for western North America. Opposing arrows indicate periods of rifting and bent arrows indicate compressional events (from John et al., 2003).

(Cline et al., 2005). Synsedimentary faults that developed during the Paleozoic are probably a reactivation of earlier basement faults. These faults sometimes spatially control abrupt facies changes. They also appear to have formed significant fluid conduits that were sporadically utilized by diagenetic and hydrothermal fluids from the Paleozoic to the recent. Normal faulting uplifted the platform margin during deposition, creating shallow-water conditions resulting in carbonate sediments/rocks being exposed to dolomitization in a sabkha environment under arid conditions, or to karsting and collapse under more humid conditions. This exposure would have led to increased permeability and porosity, which are necessary for later fluid flow and mineralization (Armstrong et al., 1998; Cline et al., 2005).

The Humbolt and Sonoma orogenies occurred during the Pennsylvanian to early Triassic, resulting in shortening, extension and the emplacement of the Golconda allochthon (Ketner, 1977; Theodore et al., 2004).

By the middle Triassic, an east-dipping subduction zone was located along the western margin of North America, resulting in the beginning of volcanic activity in north-central Nevada (Stewart, 1980). As calc-alkaline, back-arc volcanic complexes and lamprophyre dikes were emplaced in the middle Jurassic, the Elko orogeny produced east-verging folds and thrusts (Thorman et al., 1991). Magmatism continued until 65 Ma and plutons evolved from I-type granitoids to S-type peralumininous granites in the late Cretaceous. The late Cretaceous Sevier and Laramide orogenies resulted in overall thickening of the crust (Barton, 1990).

Beginning in the late Eocene, extensional deformation was the dominant tectonic regime in the region. The direction of extension shifted from northwest-southeast in the

late Eocene to middle Miocene, to west-southeast-east-northeast in the middle Miocene. These changes were followed by another shift to the northwest-southeast in the late Miocene to present (Zoback et al., 1994).

High K calc-alkaline magmatism began ~42 Ma as the Farallon plate retreated and the hot asthenosphere mantle regained contact with the base of the North American lithosphere (Armstrong and Ward, 1991; Seedorff, 1991; Henry and Boden, 1998). This last extensional period resulted in the current Basin and Range province, as well as the crustal fluid flow responsible for the majority of gold mineralization in the Carlin trend between ~42 and 36 Ma (Evans, 1980; John et al., 2003).

## **Stratigraphy**

Sedimentary rocks located in the northern Carlin trend can be divided into two main sequences separated by the Roberts Mountains thrust: 1) the lower plate autochthonous rocks; and 2) the upper plate allochthonous rocks. The autochthonous rocks are the main hosts of gold deposits and include the Roberts Mountains Formation, the Popovich Formation, and the Rodeo Creek unit (Figure 3).

The Silurian-Devonian Roberts Mountains Formation ranges in thickness from 1100 to 1500 ft. (340 to 460 m) and has several members and units. The members include a Laminated Micritic Limestone member and an Apron Facies member (Furley, 2001).

The Laminated Micritic Limestone member consists of a thick sequence of alternating light and dark, laminated silty limestone to calcareous siltstone with the laminations ranging in thickness from less than one inch (2.5 cm) to several inches. The Apron Facies contains three units similar to the Laminated Micritic Limestone member

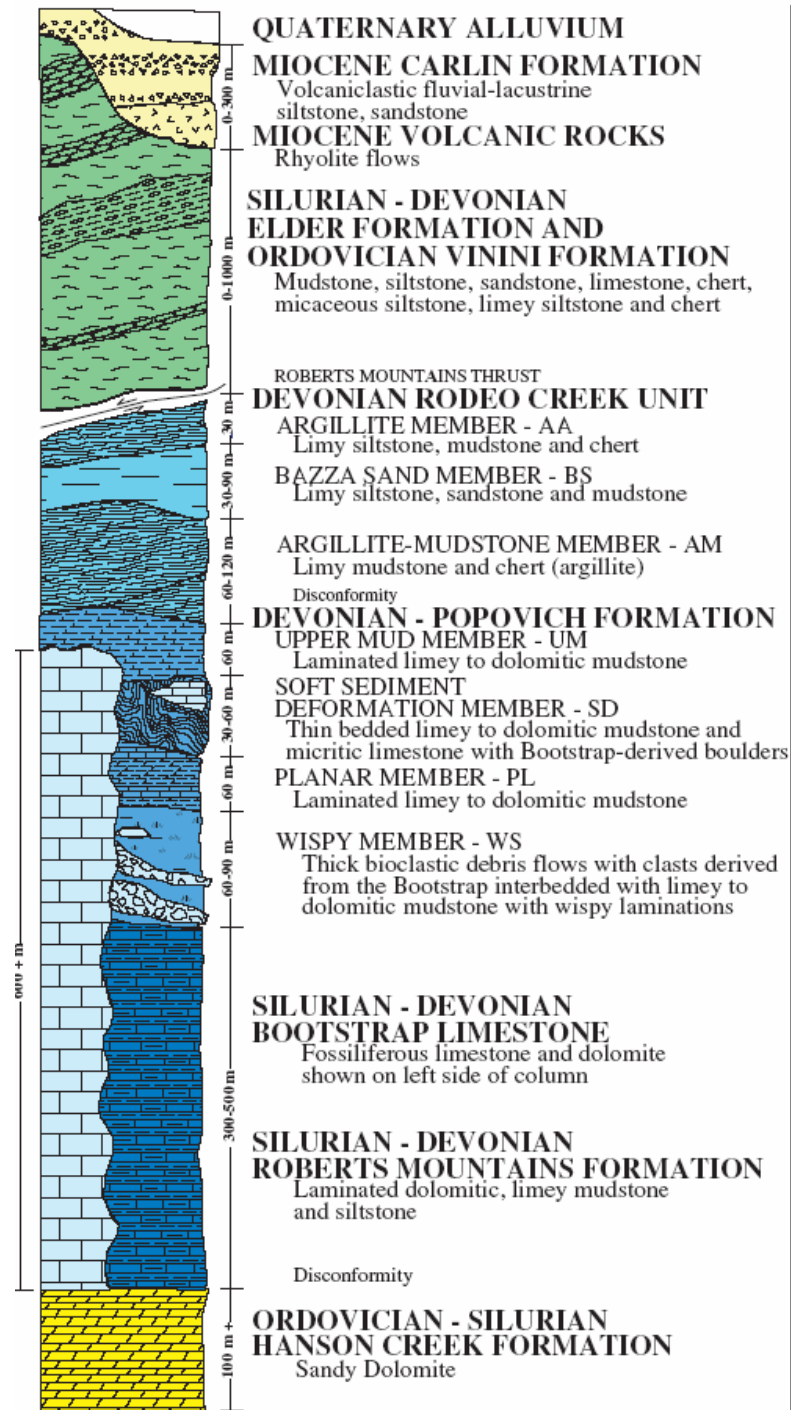


Figure 3: Tectonostratigraphic column of the northern Carlin trend illustrating the time-equivalent Bootstrap limestone unit and the Roberts Mountains and Popovich Formations (from Emsbo et al., 2003).

described above, but with increasing occurrence of thin to thick debris flows containing reef, shoal, and slope-derived sediments, along with interbedded wispy textures due to bioturbation and eventual loss of laminations (Furley, 2001).

The Bootstrap subunit, a massive, shallow-water limestone, is contemporaneous with the upper part of the Roberts Mountains Formation (Upper Silurian) and the Popovich Formation (Middle Devonian) (Jory, 2002). The Bootstrap limestone is composed of two facies representing deposition along a platform margin: a massive limestone with visible crinoids and ooids (shoal facies), and a massive light to dark gray limestone with visible crinoids, corals, bryozoans, mollusks, gastropods and algae (reef facies) (Figures 4 and 5) (Furley, 2001). The Bootstrap limestone is up to 2000 feet (610 m) thick at the northern end of the Carlin trend and thins to the south (Jory, 2002).

This project focuses on the Bootstrap limestone, with samples collected from around four deposits (Figure 6). This unit can be a significant ore host as the Meikle, Bootstrap-Capstone, Storm (Dee-Rossi) and recently discovered South Arturo deposits are all hosted in a silicified breccia within the Bootstrap limestone or at the upper contact of the Bootstrap (sections, Figure 7).

The Bootstrap was chosen for study because of its low original porosity and permeability that should have restricted the flow of hydrothermal fluids. Such restricted flow should have resulted in a condensed sequence of hydrothermal alteration in comparison to coeval units with higher porosities and permeabilities (i.e., Roberts Mountains and Popovich Formations).

The Devonian Popovich Formation is a 500 to 800 foot (150 to 250 m) thick unit containing several members. Overall, the unit is a dark gray to black mudstone to

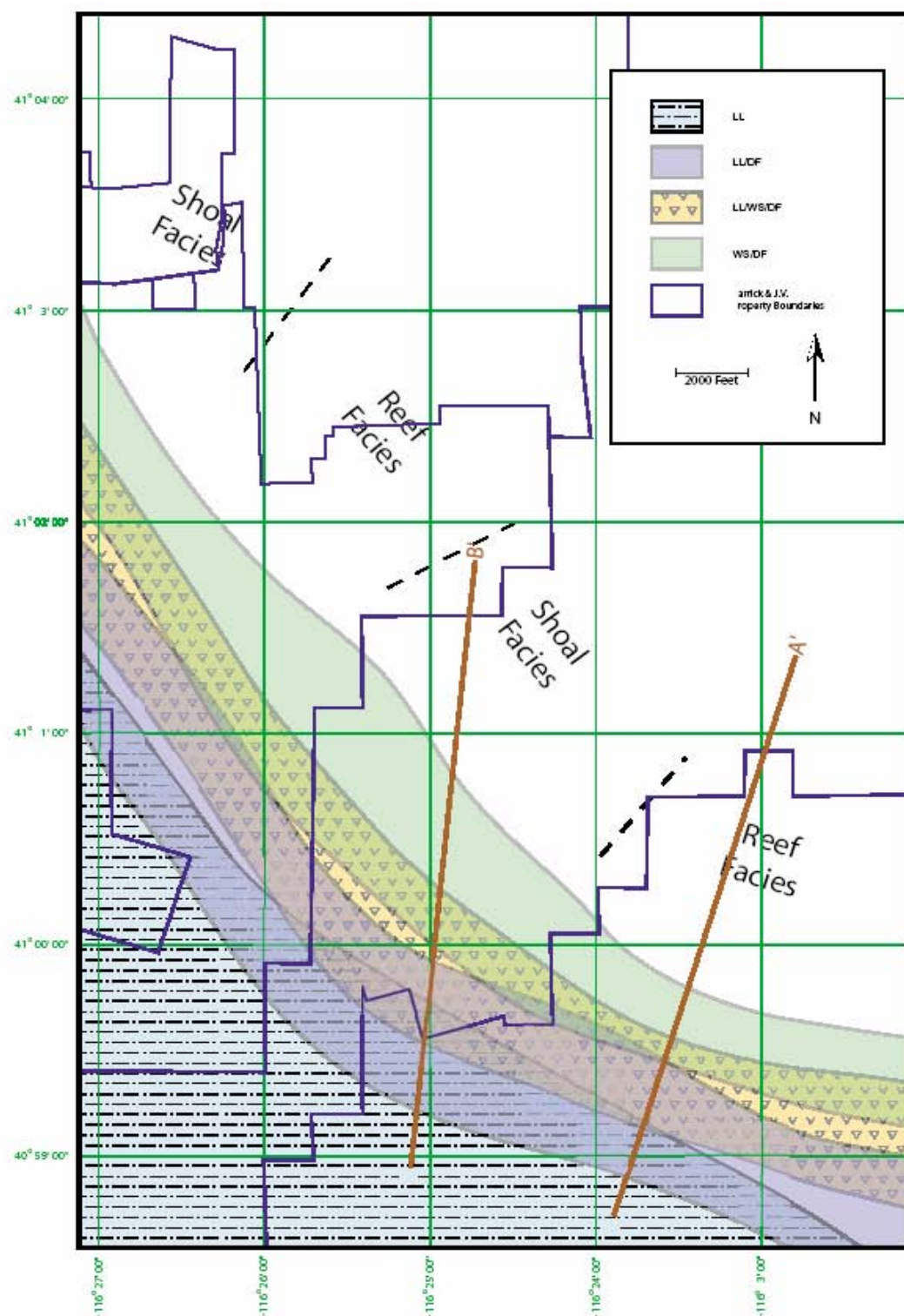


Figure 4: Distribution map of shoal and reef facies illustrating facies changes within the Bootstrap limestone (shown as white area on map) (from Furley, 2001).



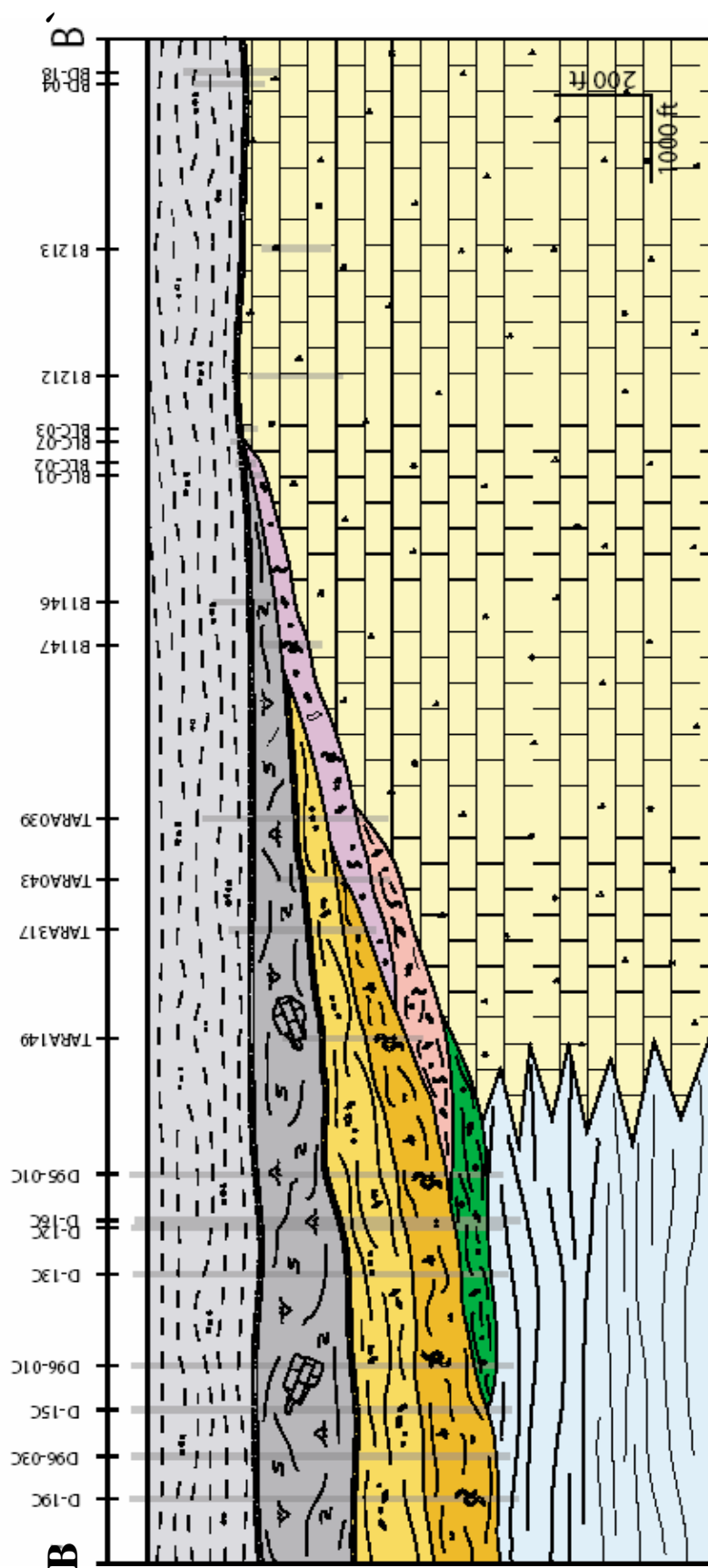


Figure 5: Cross section B-B' through the shallow sloping Bootstrap shoal facies illustrating the relationship between the Bootstrap limestone unit and the Roberts Mountains Formation (from Furley, 2001). The majority of samples in this study come from the shoal facies.

Figure 6: Geological map of the Carlin trend with an enlarged area indicating the study area and a simplified map illustrating deposit locations (Moore, 2002; Barrick Gold Corporation, 2005). Purple circles on the geologic map show the locations of drill holes logged for this study. Main units of the geologic map include Miocene Carlin Formation (tan), Devonian Slaven Chert and Silurian Elder Formation (light purple), and Ordovician Vinini Formation (purple). This study focuses on the region near the deposits of Meikle, Ren, South Arturo, and Dee-Rossi (Storm).

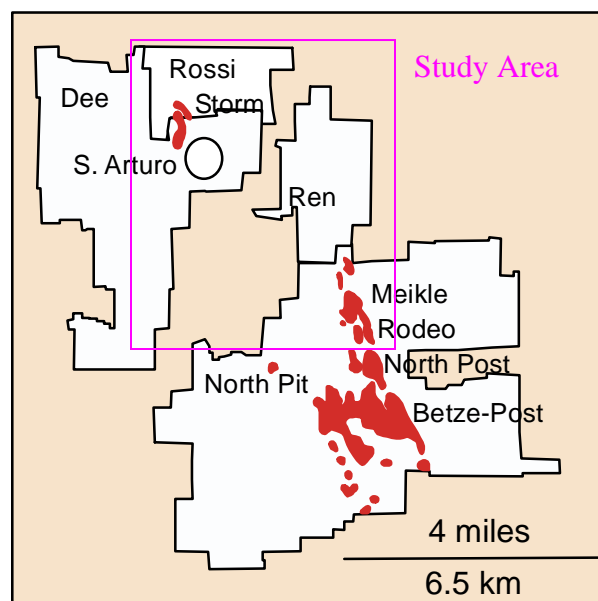
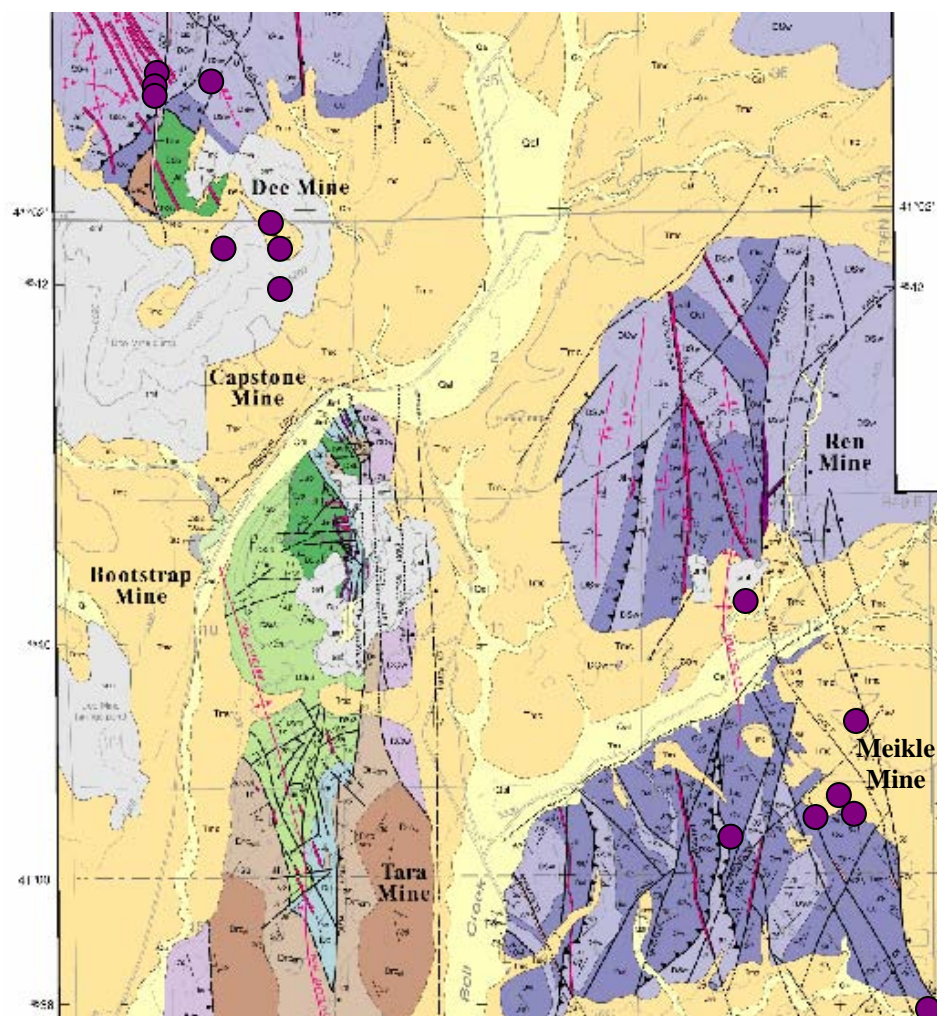


Figure 6

Figure 7: Cross sections from three deposits near which samples were collected. Cross sections show the relationship of the Bootstrap limestone unit relative to mineralization (a) Storm deposit (modified from Dobak et al., 2002); (b) Meikle deposit (modified from Emsbo et al., 2003); (c) South Arturo deposit (modified from Barrick Gold Corporation, 2005).

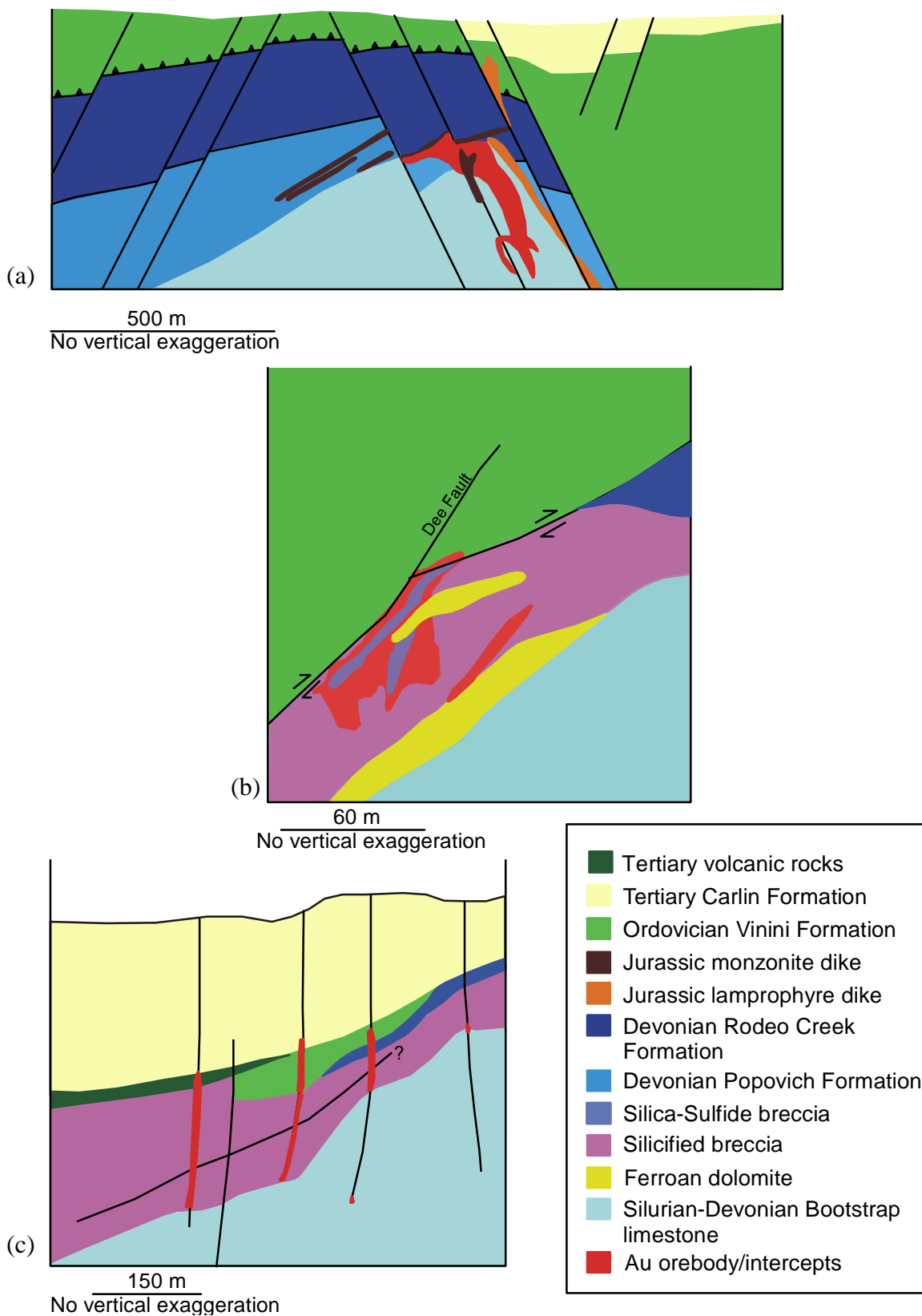


Figure 7

siltstone with textures varying from wispy to thinly interbedded with debris flows containing fossil hash to soft-sediment deformation to very common thinly laminated units. The sequence of units indicates deepening throughout deposition (Furley, 2001).

Conformably overlying the Popovich is the dark gray Devonian Rodeo Creek unit composed of gray siltstone, mudstone, chert and argillite along with upper units composed of siliceous mudstone, siltstone and calcareous siltstone. The unit is 800 feet (250 m) thick, although there are areas where the entire upper part of the unit has been removed by the Roberts Mountains thrust (Teal and Jackson, 1997).

Above the thrust, the allochthonous sequence is primarily composed of the 5,000 foot (1500 m) thick Vinini Formation consisting of Lower Ordovician to Middle Silurian sedimentary chert, mudstone, siliceous mudstone, and minor greenstone. This unit hosts small, fault-controlled, vein deposits (Jory, 2002).

## **Structure**

The north-northwest trend in mineralization reflects the young north-trending Basin and Range topography intersecting a pre-existing zone of crustal weakness. These structures controlled mineralization throughout the Carlin trend in various forms. The dominant controlling structures are northwest faults, northeast faults, anticlinal folds, and collapse breccia bodies.

In the Carlin trend, northwest-striking, high-angle structures are the dominant feature and served as primary fluid conduits for the Tertiary hydrothermal systems. Lamprophyric and monzonitic dikes commonly fill these faults (Teal and Jackson, 2002). In the study area, the Ren, Post, Dee, and Hinge structures are the main faults.

Northeast-striking faults are particularly important where they intersect northwest-striking faults, as they acted as structural fluid traps, focusing gold mineralization. Dikes rarely fill these faults (Teal and Jackson, 2002).

The general trend of folds in the region is northwest, although some are north- or northeast-trending (Volk et al., 1996; Teal and Jackson, 2002). The north-south trending faults are less common and are related to thrust faulting. Folds have broad to moderate amplitudes with mesoscopic northwest-southeast-trending hinges. These folds are well developed in the Rodeo Creek and Vinini Formations, possessing intensely fractured and veined fold hinges (Volk et al., 1996). These mesoscopic folds are associated with northwest-trending anticlines and synclines that acted as traps for migrating fluid on a regional scale (Teal and Jackson, 2002).

Collapse breccia bodies have various interpretations, but mainly are responsible for an increase in permeability for gold-bearing fluids, regardless of the formation mechanism for the breccia (Teal and Jackson, 2002). Evans (2000) explored progressive brecciation events at the Meikle deposit, where five separate brecciation events occurred, including brecciation related to early karsting of the massive limestone by meteoric water, followed by hydrothermal dissolution and subsequent collapse.

### **Paleozoic Mineralization Event**

Following initial diagenesis and brecciation of the Bootstrap limestone, a Paleozoic mineralization event resulted in early ferroan dolomitization and silicification of the limestone. The base-metal event at Meikle is fault controlled and is interpreted as

being a Mississippi Valley-type deposit. This alteration was followed by late base-metal mineralization and barite precipitation (Evans, 2000).

Ferroan dolomite alteration occurred with minor disseminated pyrite  $\pm$  sphalerite along with silicification of the early dolomite. Zebra texture, alternating white and black bands of dolomite, formed during this event. The black bands are typically ferroan and the white bands can range from non-ferroan to ferroan. Silicification was pervasive during this stage, replacing the majority of limestone with quartz. The location of this jasperoid indicates that silicification was peripheral to dolomite alteration (Evans, 2000).

Base-metal mineralization preferentially replaced ferroan dolomite with sphalerite, minor galena, chalcopryite, and pyrite. Following base-metal mineralization, the formation of veins of barite  $\pm$  dolomite, calcite, quartz, and honey-colored sphalerite veins occurred (Evans, 2000).

The base-metal event was followed by silicification, hydrocarbon migration, and stylolitization. Veins that contain bitumen, quartz and/or calcite cross-cut massive limestone, dolomitized limestone, and jasperoids. The timing of these brecciation and mineralization events are constrained by cross-cutting relationships with Jurassic dikes (Evans, 2000).

### **Cretaceous Mineralization Event**

During the late Jurassic there was a period of igneous activity, polymetallic mineralization and alteration of intrusive rocks. Mineralization included quartz veins with galena, bournonite, freibergite, pyrite, sphalerite, chalcopryite, covellite, minor bismuthinite, and illite (Emsbo et al., 2003).



The alteration associated with this event is principally preserved in the intrusive rocks. Alteration in the monzonite dikes was most pervasive, and included feldspar altering to illite and kaolinite, quartz precipitation, and replacement of sphalerite by pyrite. Lamprophyre dikes contain calcite, dolomite, magnesite, chlorite, quartz, illite, and talc as alteration products (Evans, 2000; Emsbo et al., 2003).

A second Cretaceous hydrothermal event is more common in southern portions of the Carlin trend and is characterized by Cu mineralization and sericitic alteration (Arehart et al., 1993; Drews-Armitage et al., 1996; Teal and Branham, 1997).

### **Tertiary Mineralization Event**

Gold in the Carlin trend occurs primarily in the lattices of pyrite and arsenian pyrite as submicron particles with concentrations as high as ~9,000 ppm (Wells and Mullens, 1973; Emsbo et al., 2003; Palenik et al., 2004; Reich et al., 2005). The gold-bearing pyrite and marcasite typically occur as discrete grains a few micrometers in diameter or as rims on earlier-formed pyrites. The types of deposits in the trend vary greatly with structural controls to lithologic controls to breccias with great range in terms of grade and deposit size (Emsbo et al., 2003).

The mineralizing fluids that precipitated gold were probably low to moderate temperature (180-240°C), low salinity (~2-3 wt % NaCl equivalent), aqueous fluids containing CO<sub>2</sub> (<4 mol %) and CH<sub>4</sub> (<0.4 mol %), and 10<sup>-1</sup>-10<sup>-2</sup>m H<sub>2</sub>S (Cline and Hofstra, 2000; Hofstra and Cline, 2000; Lubben, 2004). Precipitation of Au and formation of pyrite are considered to have been controlled by the reaction of sulfur in the fluid with Fe in the host rocks. Though sulfidation is commonly described as the most

important control on Au mineralization, the presence of bitumen in high-grade ore indicates a reaction between the bitumen and Au-bearing fluids (Kuehn and Rose, 1992; Stenger et al., 1998; Hofstra and Cline, 2000; Fortuna et al., 2003). However, alternate possibilities for the precipitation mechanism are necessary because the sulfidation of Fe-rich host rocks does not produce enough acid to be responsible for the intense mineralization in high-grade ore (Emsbo et al., 2003).

Varying  $\delta D_{H_2O}$  values of the ore fluid indicate three possible origins. Possible sources include meteoric, magmatic or metamorphic fluids (Hofstra et al., 1999; Cline and Hofstra, 2000; Emsbo et al., 2003; Lubben, 2004). The range of values may be explained by mixing among all three or that different regions of the trend have different sources. Sulfur in the ore-stage fluid has a broad range of isotopic values, indicating a sedimentary source that utilized several pathways to derive  $H_2S$  (Hofstra and Cline, 2000; Emsbo et al., 2003).  $H_2S$  could have been produced by dissolution of pyrite, destruction of organosulfur compounds, thermochemical sulfate reduction, and/or desulfidation of pyrite to pyrrhotite. As the principle transporter of Au in fluid, the source of S could give insight to the source of Au (Cline et al., 2005).

The timing of mineralization has been cautiously agreed upon as Eocene (~42 Ma to 36 Ma), although constraining the age has been a subject of debate (Ressel et al., 2000; John et al., 2003; Cline et al., 2005). Some authors suggest that the varying ages from the region indicate multiple periods of gold mineralization (Teal and Jackson, 1997).

The lack of evidence for fluid boiling and ore-fluid phase-equilibria parameters constrain the possible depth for ore deposition. Depth of gold deposition is thereby

constrained to a minimum depth between ~1.7 km and 6.5 km and a maximum depth no greater than 5 to 8 km (Hofstra and Cline, 2000).

The multiple possibilities for the origin of the ore-bearing fluid and source of gold create several possible genetic models. These include a meteoric water model with lateral flow of meteoric water or deep crustal meteoric convection (Ilchik and Barton, 1997; Emsbo et al., 2003); an epizonal intrusion model that relates Carlin deposits to epizonal plutons (Sillitoe and Bonham, 1990; Johnston and Ressel, 2004); and a deeply sourced ore-fluid model that requires a magmatic or metamorphic water source (Seedorff, 1991; Hofstra and Cline, 2000). Although still debated, the genetic model for these deposits probably consists of a combination of elements from the previously mentioned three models (Cline et al., 2005).

Cline et al. (2005) suggested a genetic model for Carlin-type deposits that involves hydrothermal fluids exsolved from lower crustal melts formed by mafic magmas injected into the lower crust during the Eocene. This hydrothermal fluid, along with possible metamorphic fluids, scavenged Au and other trace metals from the Neoproterozoic rocks as it moved upward.

Aqueous hydrothermal ore fluids became enriched in  $\text{H}_2\text{S}$  through interactions with wall rocks as they flowed along faults, causing the scavenging of Au. These ore fluids were then diluted by deeply convecting meteoric waters (Figure 8). The ore fluids collected along the boundaries of stocks and in structural traps. The fluids increased permeability through decarbonatization and argillization of wall rocks through which they flowed. This interaction with the wall rocks also exposed available Fe, which led to

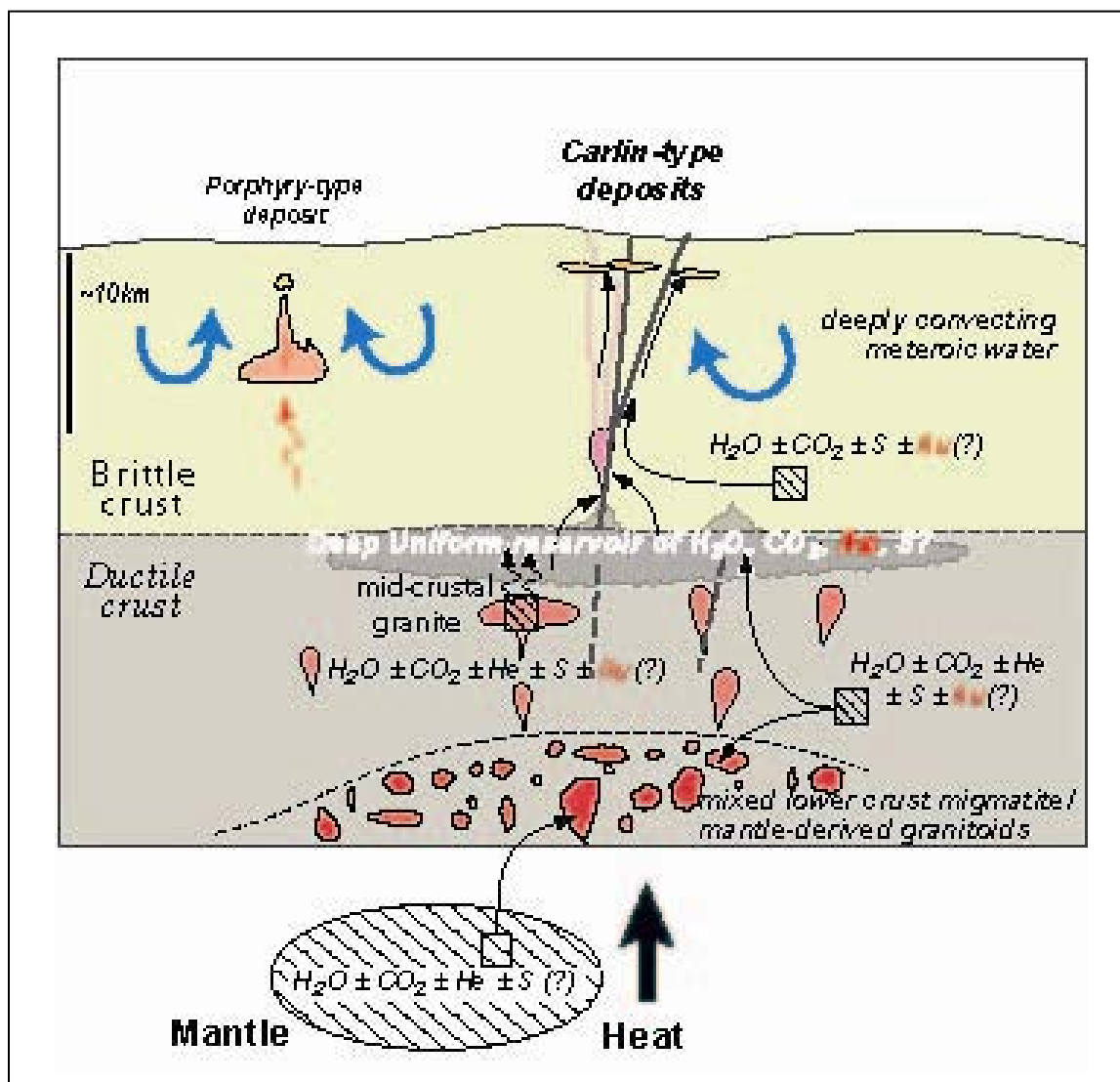


Figure 8: Genetic model for Carlin-type deposits combining elements from magmatic and meteoric models to explain how hydrothermal fluids evolve to become ore fluids and possible sources for Au (from Cline et al., 2005).

sulfidation and pyrite precipitation. Precipitation of pyrite decreased the  $a_{\text{H}_2\text{S}}$  in the ore fluids and Au was co-precipitated with pyrite.

The final stages of fluid flow in the Carlin trend included a reduction in ore fluids and mixing and cooling of fluids caused by the collapse of unexchanged meteoric fluids into the system (Cline et al., 2005).

### **Alteration**

Characteristic alteration of Carlin-type deposits includes decarbonatization, argillization, silicification, and sulfidation. Alteration of the carbonate host rocks includes dolomitization, ferroan dolomitization, cement precipitation, and silicification.

Decarbonatization is common for all deposits in the trend and the degree of decarbonization was controlled by the fluid acidity, the amount of cooling, and the degree of fluid-rock interaction (Hofstra and Cline, 2000; Cline et al., 2005). Dissolution of carbonate host rocks possibly led to collapse breccias prior to gold mineralization to form high-grade ore in some deposits (Emsbo et al., 2003).

Assemblages of kaolinite  $\pm$  dickite  $\pm$  illite formed where older alumino-silicate minerals and acidic ore fluids interacted. Argillization is uncommon in the carbonate rocks, but is intense in basalts, lamprophyres, and other igneous rocks (Hofstra and Cline, 2000).

Silicification is widespread in the form of jasperoids and drusy quartz-lined vugs. The occurrence of jasperoids appears to be associated with the presence of ore, although jasperoids can range from barren to high-grade ore (Bakken and Einaudi, 1986; Ye et al., 2002). The vugs that are later lined by quartz formed by dissolution of the carbonate host

rocks. The lack of quartz as an ore-stage mineral probably reflects the low temperature of mineralizing fluids, given that quartz precipitation is inhibited below ~180 °C (Rimstidt, 1997; Cline et al., 2005).

## RESEARCH RESULTS

This study compiled detailed hand specimen, petrographic, cathodoluminescent (CL), and isotopic descriptions of carbonate alteration occurring within the Bootstrap limestone formation. Samples from 11 drill holes throughout the study area were used in the descriptions (Figure 9; Table 1). Six carbonate phases were found to be important variations in the Bootstrap limestone. This included original limestone, diagenetic-planar dolomite, saddle dolomite, ferroan dolomite, zebra texture dolomite, and late calcite.

### **Limestone**

Two facies are recognized within the Bootstrap limestone unit: a shoal facies and a reef facies. Samples for this study came from a large area, but are predominantly from the shoal facies. The best samples of least-altered limestone are from near the Meikle deposit. Completely unaltered limestone was unavailable in the study area because of the presence of early diagenetic cementation.

In core, the Bootstrap limestone shoal facies is a massive, light- to medium-gray limestone with visible ooids and crinoids (Figure 10). The reef facies is also medium-gray, but with visible crinoids, corals and reported mollusks, bryozoans, and gastropods (Furley, 2001).

Thin-section analysis shows the shoal facies is dominated by coarse-grained, well-sorted oolitic to peloidal grainstone with low porosity (<3%), 3-5% early dolomite, and rare stylolites. The matrix is a coarsely crystalline equant calcite spar cement (Figure 11).

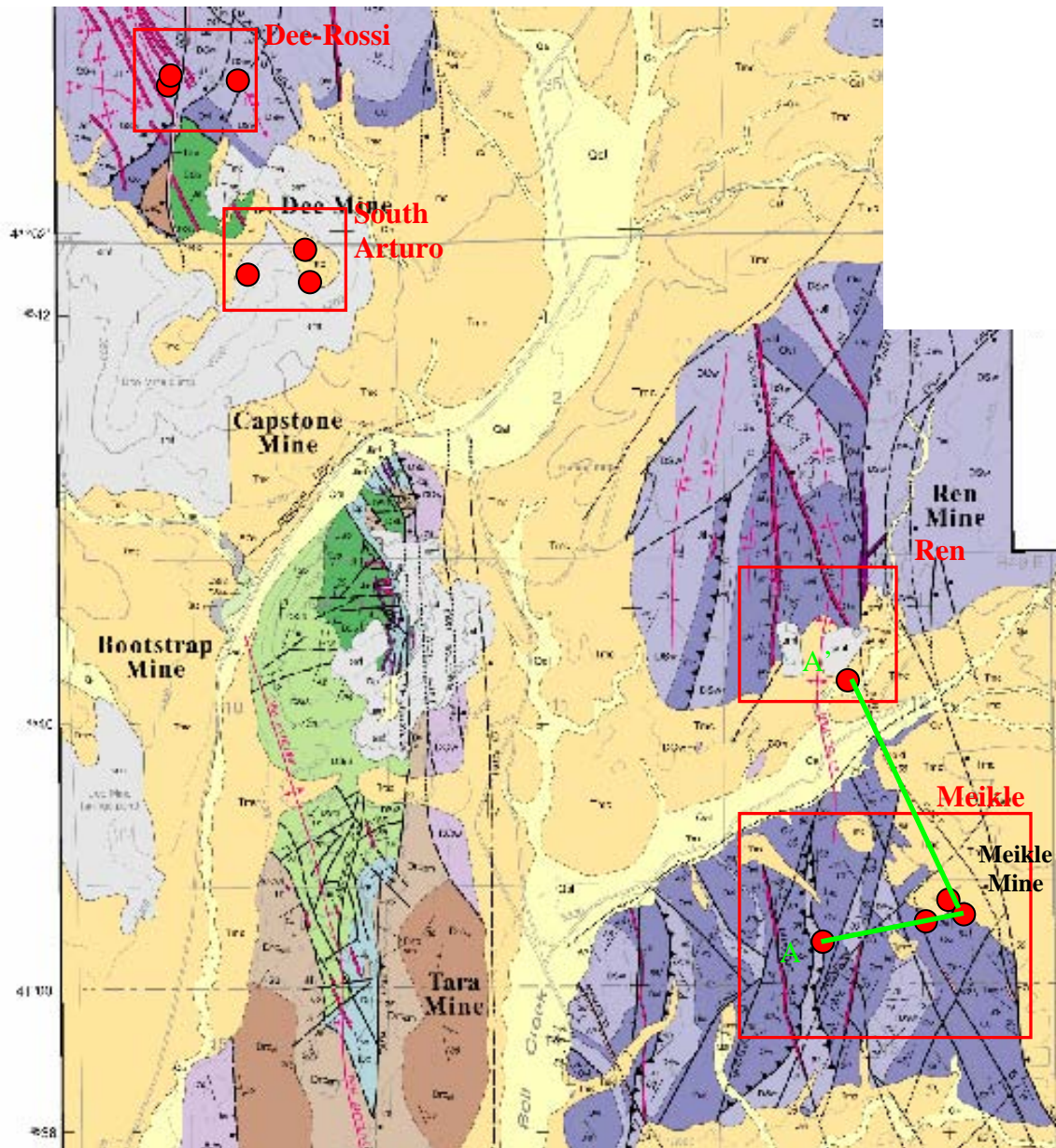


Figure 9: Locations of the 11 drill holes sampled are marked by green circles (modified from Moore, 2002). The drill holes were selected for their intervals of Bootstrap limestone. All samples in this study come from these drill holes and four deposit areas.

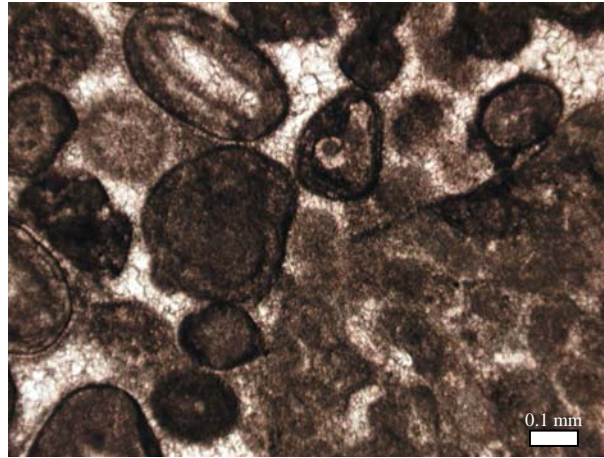


Deposit	Description	Logged Drill Holes
Meikle	Silicified breccia-hosted deposit (Emsbo et al., 2003)	Ex-21c; MST-1; GA-65c; U17-M05-3
Ren	Active exploration: possible breccia-hosted similar to Meikle, historically, mineralized dike, stratabound mineralization in Popovich Formation (Farquharson et al., 2004)	RU-8
Dee-Rossi (Storm)	Silicified heterolithic breccia-hosted (Dobak et al., 2005)	D2-100-2; D0-100-1
South Arturo	Active exploration: Breccia-hosted, oxide gold deposit (Hipsley et al., 2007)	BD-131; BD-181; BD-177; BD-178

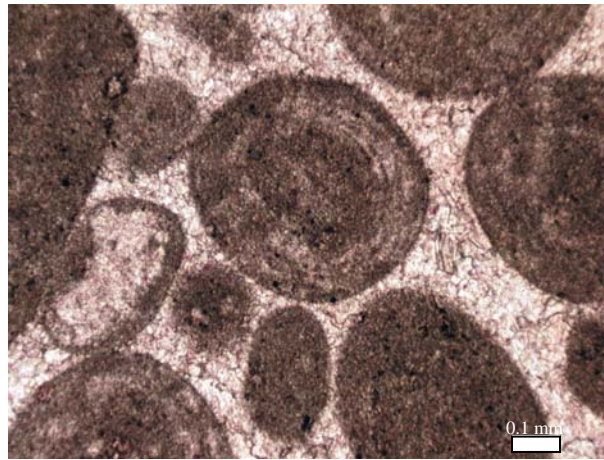
Table 1: Deposit areas, type of deposit, and drill holes that were used in this study. The four deposits are similar in that they are hosted in breccia bodies within or at the top contact of the Bootstrap limestone. South Arturo and Ren deposits are still being actively explored and deposit types are not fully established.



Figure 10: Core of the massive, gray, oolitic grainstone with calcite veining from the shoal facies of the Bootstrap limestone.



(a)



(b)

Figure 11: Typical limestone samples from the Bootstrap limestone. (a) Sample from Evans (2000), Photomicrograph showing a peloidal grainstone with micritized peloidal grains and early equant calcite cement; plane-polarized light. (b) U17-M05-3, 382', Photomicrograph of an oolitic grainstone with early calcite cement; plane-polarized light.

The reef facies is a coarse-grained, moderately sorted oolitic grainstone to fossiliferous boundstone with possible skeletal grains including crinoids, bryozoans, gastropods and brachiopods (Furley, 2001).

Cathodoluminescence imaging shows dull luminescent grains with locally brightly luminescent rhombohedral dolomite crystals along the edges of grains, dull early calcite cement, and destructive, brightly luminescent calcite veins (Figure 12).

Stable isotopic data for limestone samples mainly fall between  $\delta^{18}\text{O}$  values of -11.0 to -6.7 ‰PDB (mean -8.8 ‰PDB) and  $\delta^{13}\text{C}$  values of 0.7 to 2.3 ‰PDB (mean 1.4 ‰PDB) (Figure 13).

### **Diagenetic-Planar Dolomite**

Complete replacement of the limestone by diagenetic-planar dolomite only is seen in the deeper drill holes near the Meikle and Ren deposits (Figure 14). These drill holes do not intersect any degree of mineralization, but do extend through a thick section of the Bootstrap limestone unit. In vertical drill holes GA-65c, U17-M05-3, and RU-8, the top of the Bootstrap is limestone with the percentage of dolomite increasing with depth. In GA-65c diagenetic-planar dolomite begins at an elevation of ~2450 ft, in U17-M05-3 at ~2950 ft., and in RU-8 at ~1950 ft.

In core, there is very little variation between the appearance of limestone and diagenetic-planar dolomite (Figure 15). Diagenetic-planar dolomite is typically non-mimetic, although locally ooids are still visible in hand specimens. Overall, diagenetic-planar dolomite is medium-gray, giving it a slightly darker appearance than the

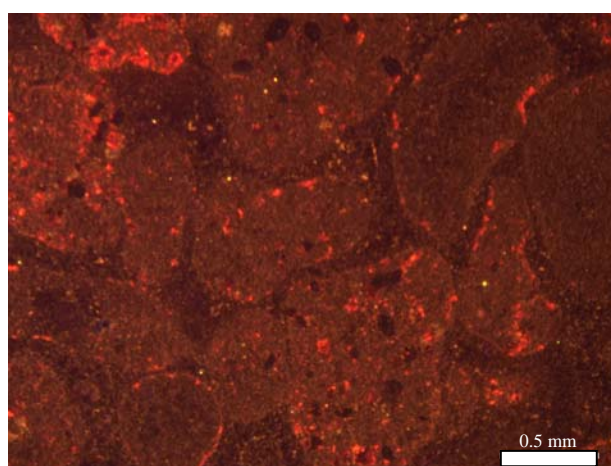


Figure 12: U17-M05-3, 6', Cathodoluminescence image of limestone showing dull luminescent calcite cement and peloids, and brightly luminescent dolomite crystals.

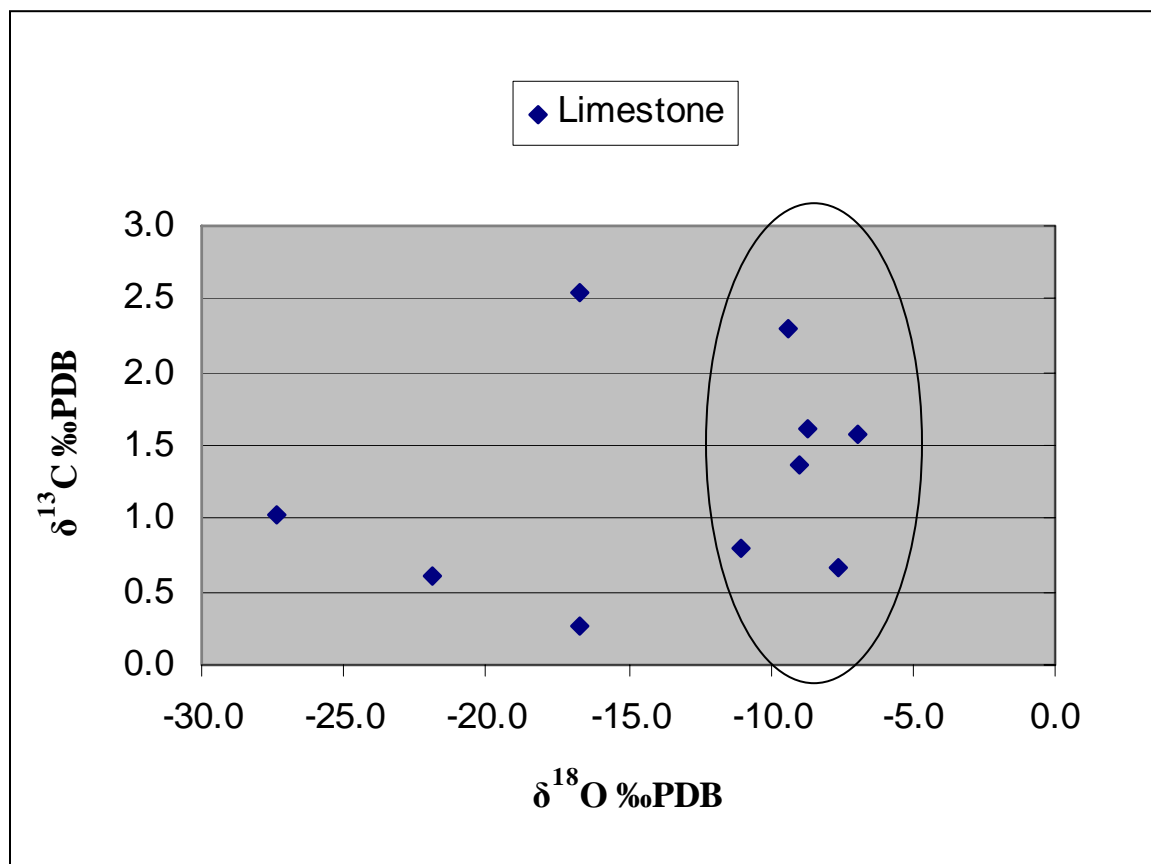


Figure 13: Plot of isotopic data for limestone samples. Samples representing the end-member limestone values are circled.



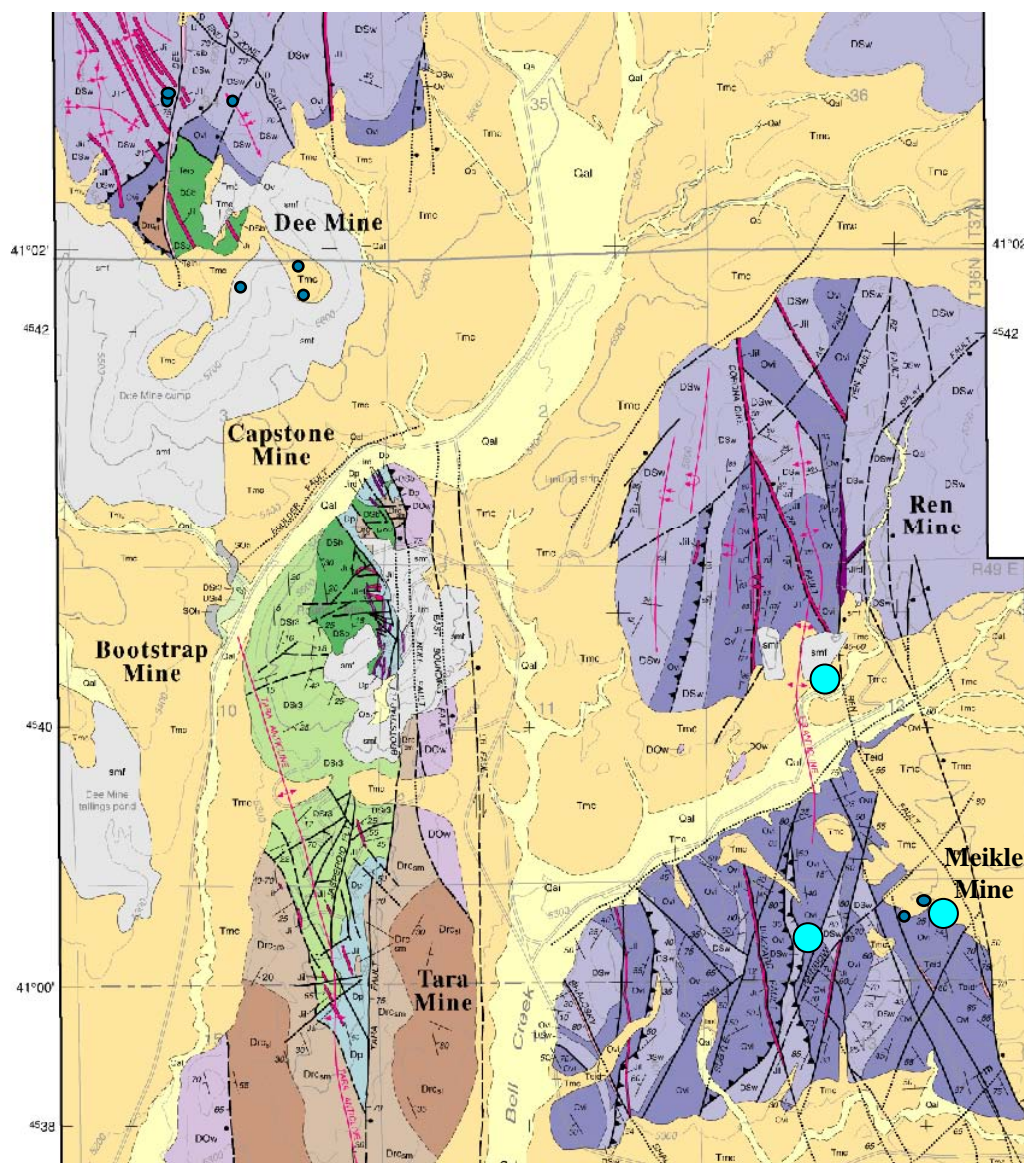


Figure 14: Location map for drill holes with diagenetic dolomite occurrences marked by blue circles (modified from Moore, 2002). Notice that diagenetic dolomite is not encountered near South Arturo or Dee-Rossi.

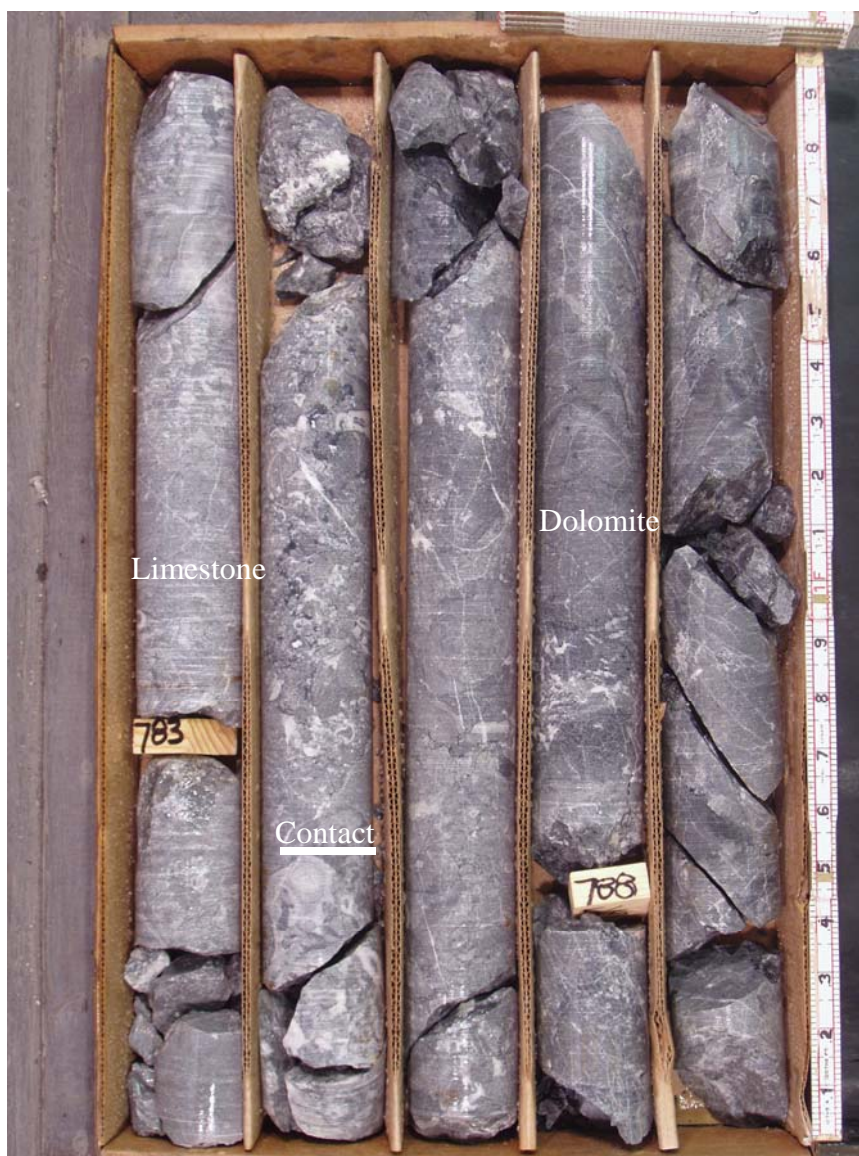


Figure 15: Core of the contact between limestone and diagenetic dolomite in U17-M05-3. There is a slight color change to darker gray, but otherwise limestone and diagenetic dolomite look very similar in core.



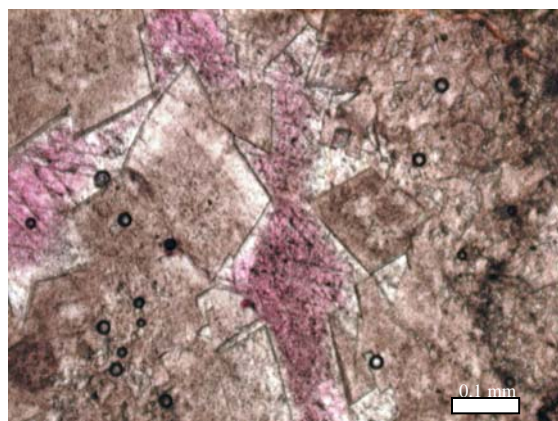
limestone. The dolomite is also commonly stylolitic. In hand sample, use of HCl is the easiest way to distinguish between limestone and diagenetic-planar dolomite.

The dolomite that occurs in these holes is rhombohedral (planar-e) with cloudy to clear centers, and is medium to finely crystalline with low porosity (2-3%), and stylolites occurring locally to commonly (Figure 16). Most limestone samples have at least a small, scattered occurrence of dolomite crystals that do not have a preference to replace grains or cement. The dolomite also occurs as very finely crystalline replacement in the original grains. Overall, this dolomite replacement is destructive of the original fabric, but sample U17-MO5-3, 820.5' is completely dolomitized with the ooid structure clearly preserved (Figure 16c).

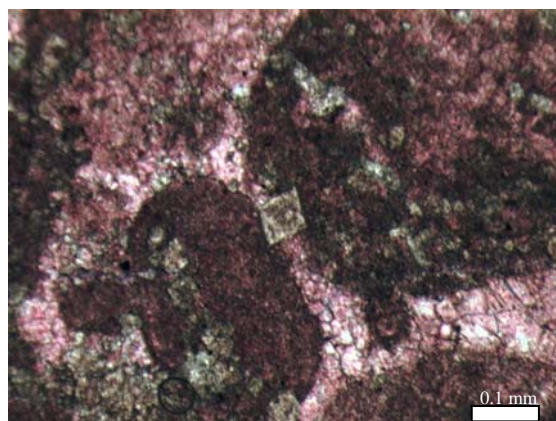
Cathodoluminescence imaging reveals consistently brightly luminescent dolomite. In limestone that has not been completely replaced by dolomite, dolomite rhombs are concentrated primarily around the edges of original grains as seen in limestone samples discussed above (Figure 17).

Diagenetic-planar dolomite isotopic data have a moderate range for  $\delta^{18}\text{O}$  from -11.8 to -4.2 ‰PDB (mean -8.4 ‰PDB) and  $\delta^{13}\text{C}$  from -0.4 to 1.6 ‰PDB (mean 0.8 ‰PDB). There are three apparent groupings in the data. The three clusters of data have similar  $\delta^{13}\text{C}$  values, and  $\delta^{18}\text{O}$  averages for each group are about -5.0 ‰PDB, -8.0 ‰PDB, and -11.0 ‰PDB (Figure 18). These clusters reflect, respectively, samples with complete recrystallization, partial recrystallization and those trending towards saddle dolomite.

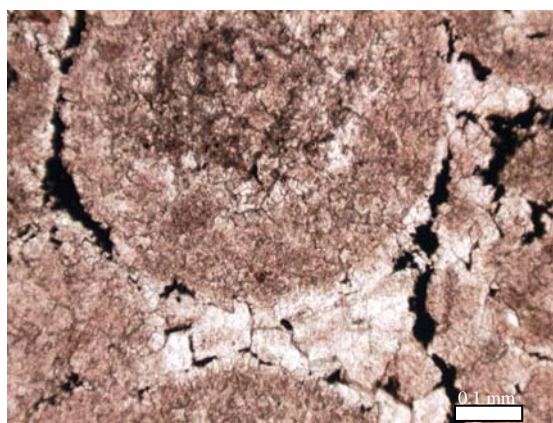
Figure 16: Photomicrographs of diagenetic samples illustrating partial (a, b, d) and complete replacement (c, e) of limestone. (a) U17-M05-3, 785', Photomicrograph of planar-e diagenetic dolomite with cloudy centers filling space occupied by calcite cement (stained pink); plane-polarized light; (b) GA-65c, 3703', Photomicrograph of planar-e dolomite rhombs with cloudy centers in limestone with original grains and calcite cement (stained pink); plane-polarized light; (c) U17-M05-3, 820', Photomicrograph of mimetic, planar-s to planar-e dolomite replacing oolitic grainstone, with dead oil in pore space; plane-polarized light; (d) RU-8, 3502', Photomicrograph of a contact between finely crystallized, planar-s to planar-e dolomite and calcite (stained pink); plane-polarized light; (e) U17-M05-3, 1380', Photomicrograph of complete replacement of limestone with medium to finely crystalline, planar-s to planar-e dolomite; plane-polarized light.



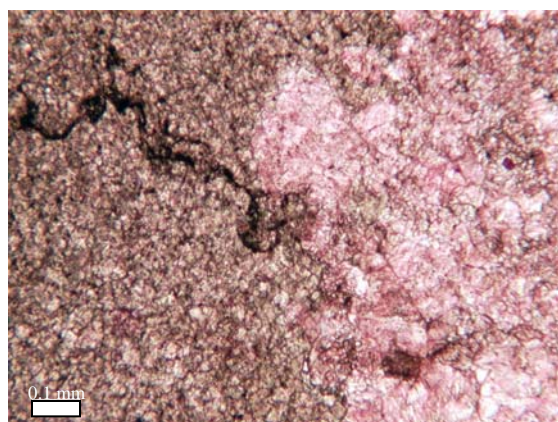
(a)



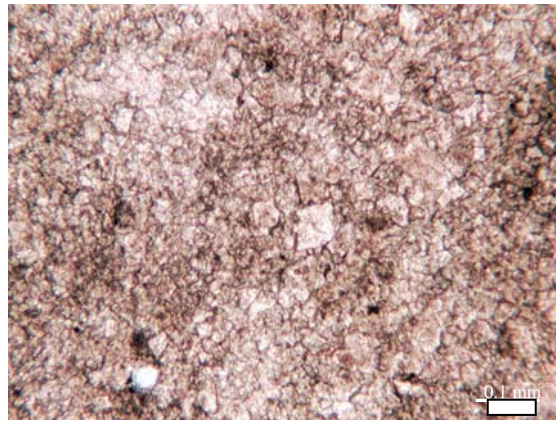
(b)



(c)



(d)



(e)

Figure 16

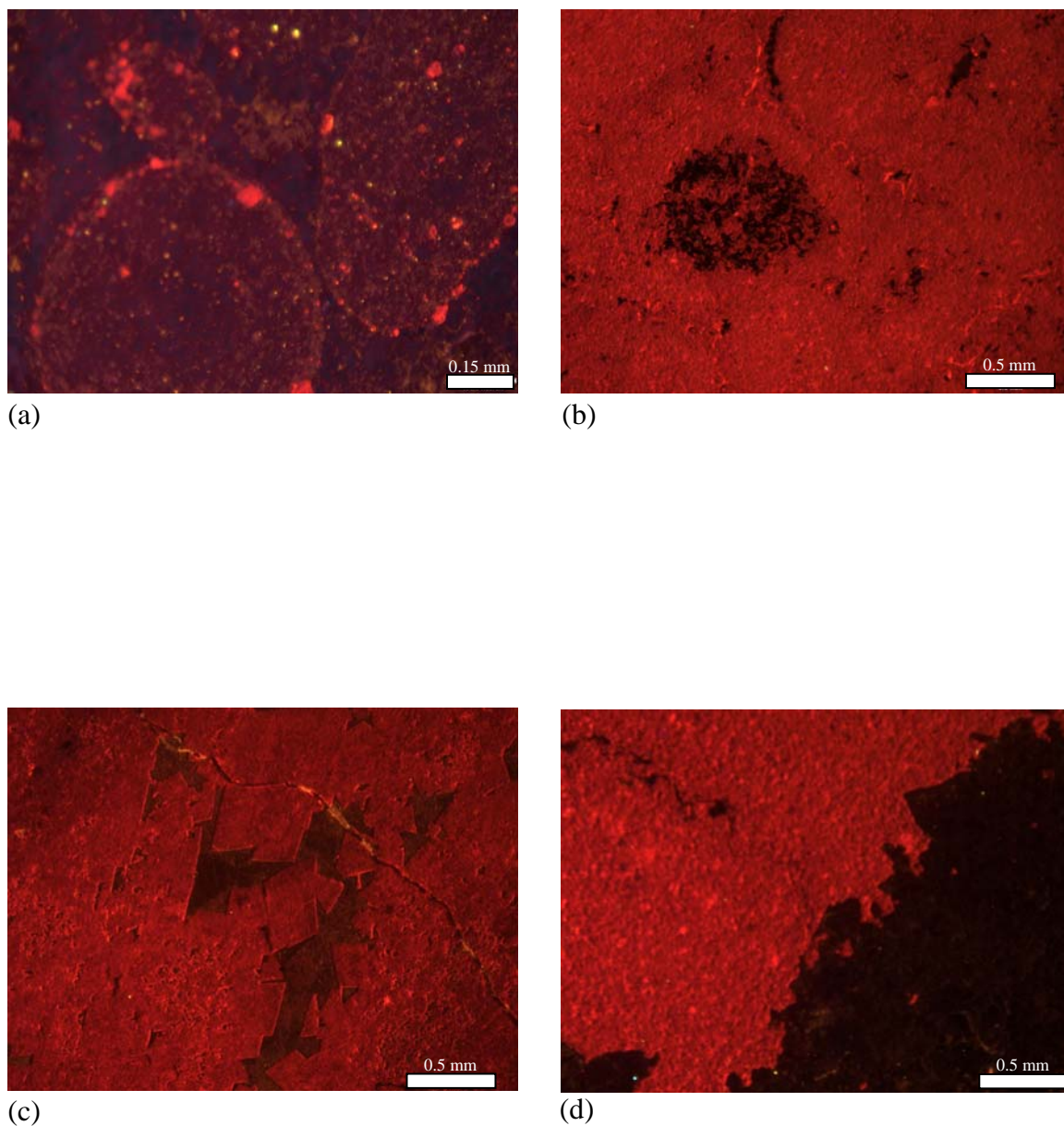


Figure 17: Cathodoluminescence images of uniformly, brightly luminescent diagenetic dolomite. (a) U17-M05-3, 382', CL image showing diagenetic dolomite brightly luminescent crystals along the edges of peloids and calcite cement as dull luminescent; (b) U17-M05-3, 820', CL image of mimetic dolomite brightly luminescent and dead oil in the center of a relic ooid; (c) U17-M05-3, 785', CL image of planar-e dolomite rhombs moderately to brightly luminescent; (d) RU-8, 3502', CL image of dolomite brightly luminescent; calcite dull luminescent.

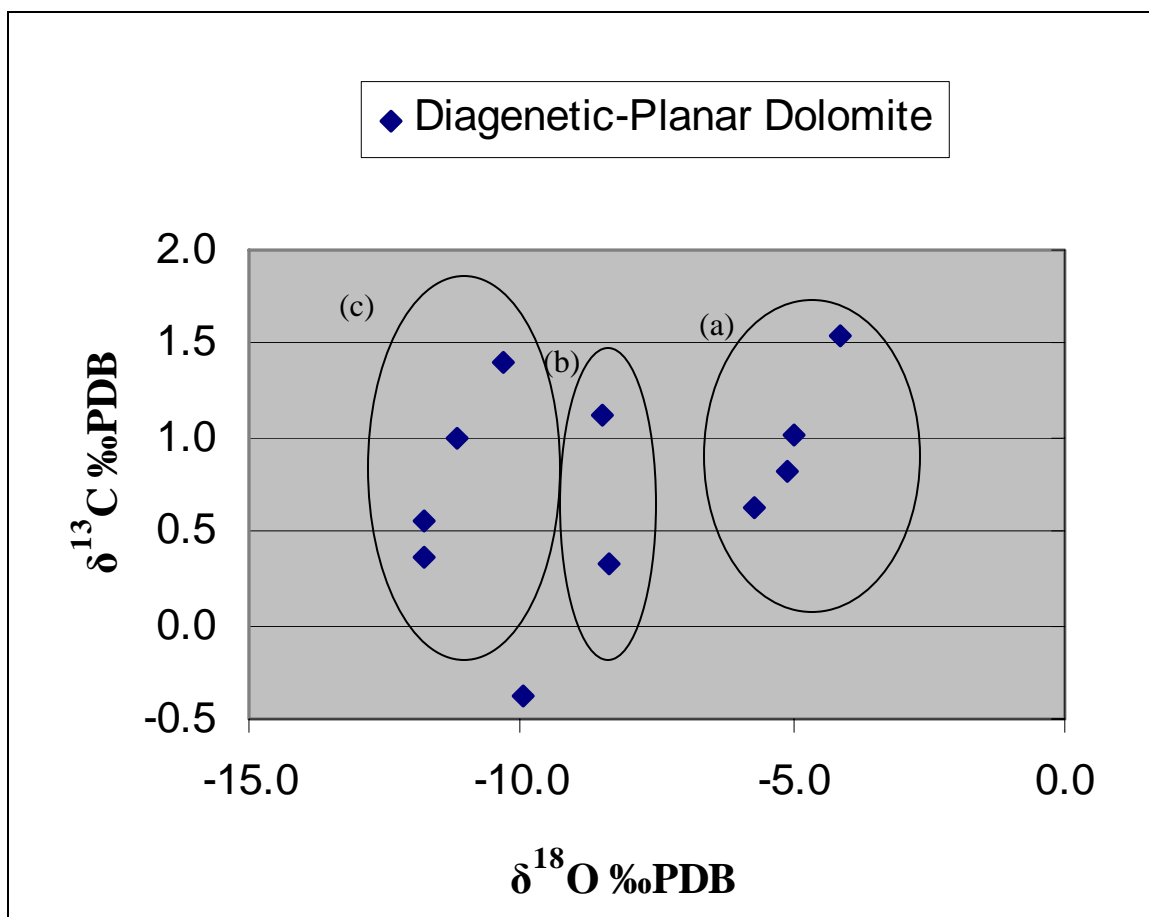


Figure 18: Isotopic data for diagenetic dolomite samples with three clusters of values circled. Circle (a) are samples with complete replacement of limestone; circle (b) are samples with partial replacement of limestone and circle (c) are samples with curved crystal boundaries (saddle-type dolomite).

## Saddle Dolomite

Saddle (or baroque) dolomite occurs in drill holes near the Dee-Rossi, Meikle, and South Arturo deposits (Figure 19). The amount of saddle dolomite observed in each drill hole increases in brecciated areas and areas proximal to Jurassic igneous intrusions. Saddle dolomite can occur as cement or as a replacement of precursor carbonate.

In core, coarse saddle dolomite ranges in color from white to gray to light pink. Core containing saddle dolomite is pervasively fractured or occurs in breccias with thin (<1 mm wide) black, sooty sulfide fracture fill or 1 mm wide calcite veins with vugs common in the center of the veins (Figure 20). Saddle dolomite occurs commonly in close proximity to igneous clasts.

In thin-section, samples of saddle dolomite from the study area range from clear to light brown in plane-polarized light, and contain polymodal, non-planar, saddle dolomite with strong sweeping extinction, to planar-s saddle dolomite with weak sweeping extinction. Rock samples with abundant saddle dolomite display low porosity (~5%) and very few stylolites (Figure 21).

Cathodoluminescence analysis shows dissolution areas of the saddle dolomite and moderately to brightly luminescent saddle dolomite with common calcite veining (Figure 22).

Isotopic data for saddle dolomite shows values from the Dee-Rossi area in ranges of  $\delta^{18}\text{O}$  from -14.1 to -9.5 ‰PDB with a mean of -11.2 ‰PDB and  $\delta^{13}\text{C}$  from 0.3 to 1.1 ‰PDB with a mean of 0.6 ‰PDB. Outliers on the plot are from near Meikle and Ren



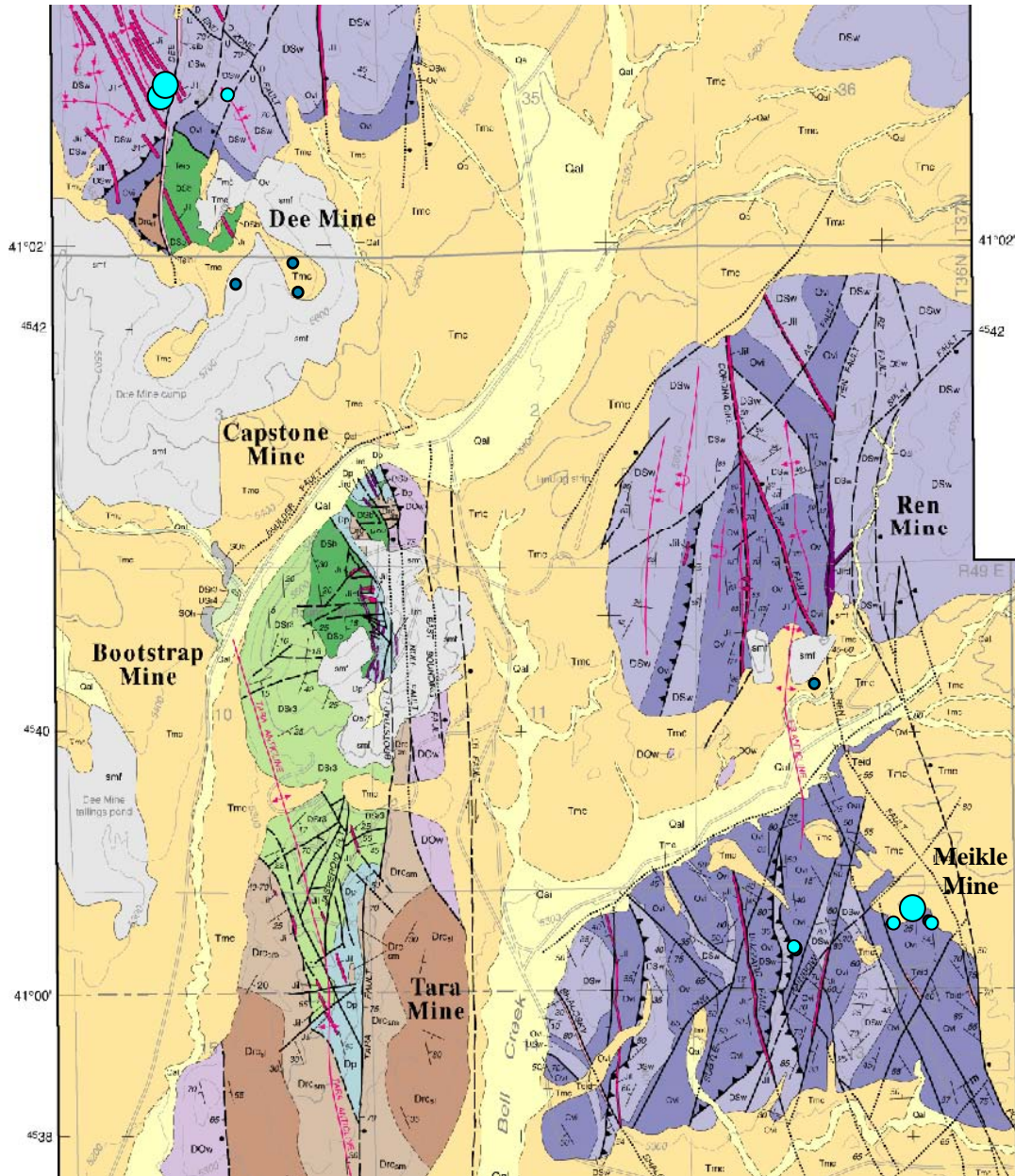


Figure 19: Locations of saddle dolomite are marked by blue circles proportionally sized to amount of saddle dolomite recognized in the core (modified from Moore, 2002). The largest circles are closest to structures and/or ore bodies with the smallest circles representing occasional occurrences in drill holes that are not near structures or ore bodies.

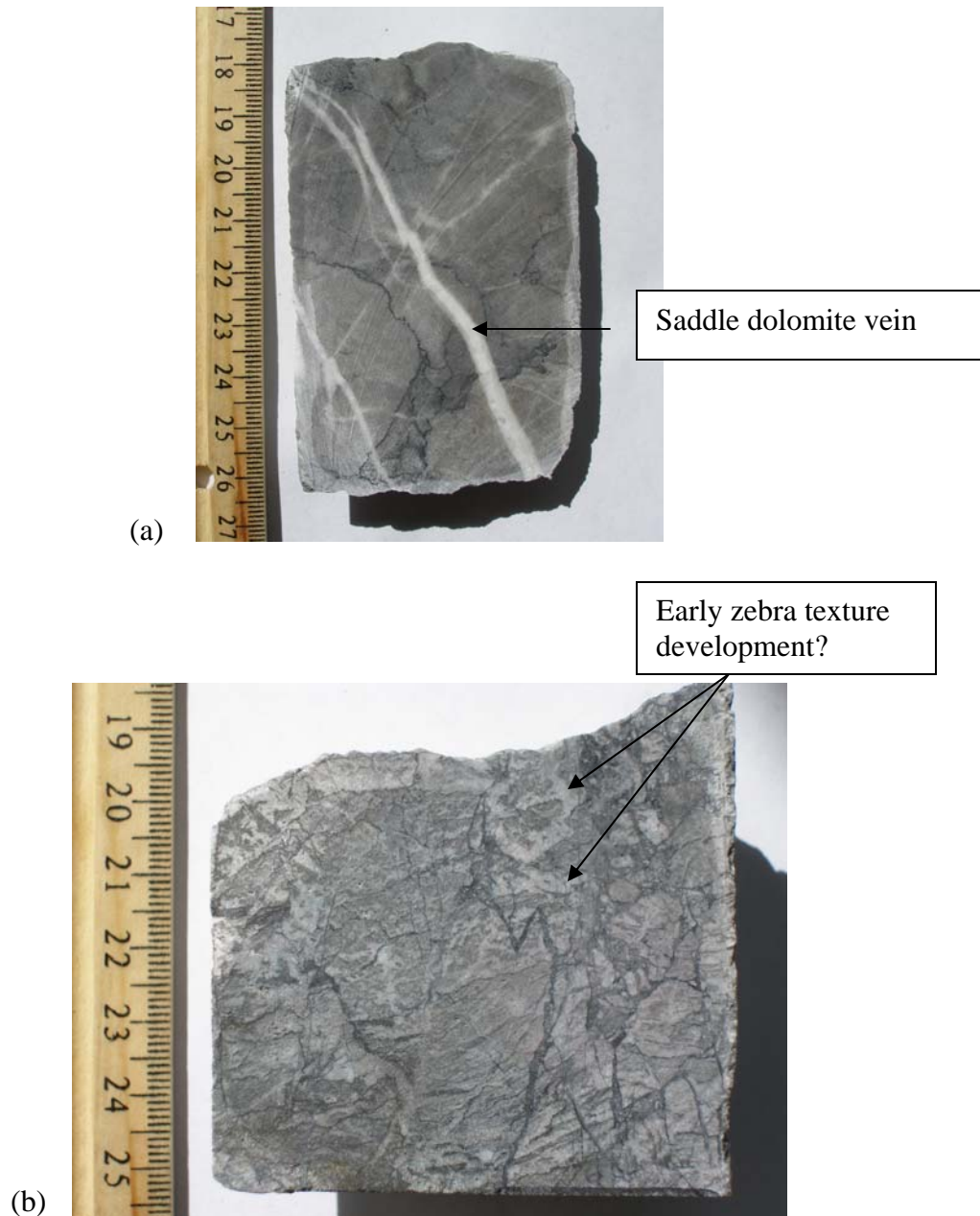


Figure 20: Hand samples of saddle dolomite occurring as a vein (a) or pervasively fractured (a) Core of GA-65c, 1825', massive, gray styolitic limestone with white saddle dolomite vein; (b) Core of U17-M05-3, 116', intensely fractured saddle dolomite with the beginning of zebra texture and sooty fracture fill.



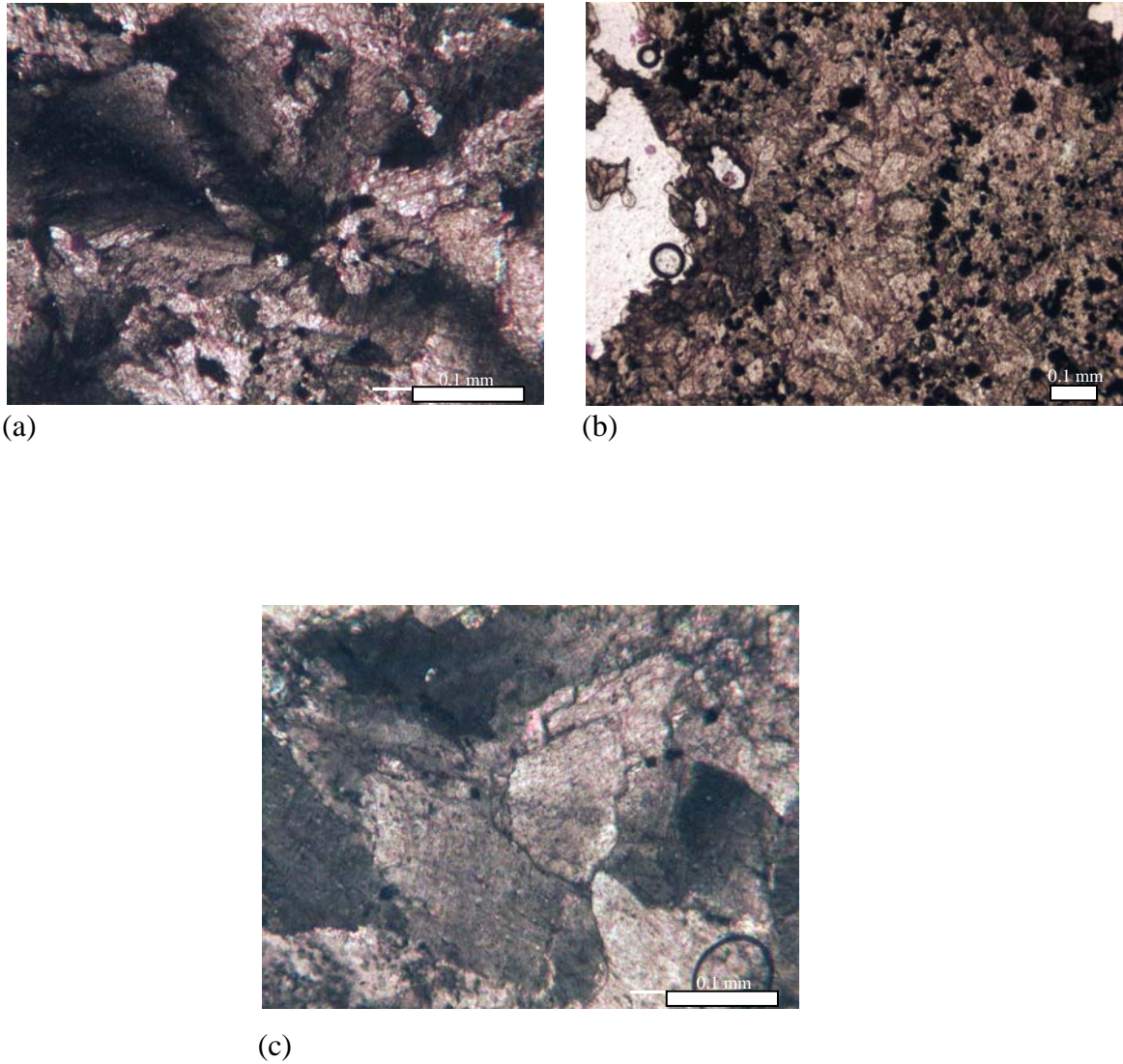


Figure 21: Photomicrographs illustrating the texture of saddle dolomite. (a) U17-M05-3, 116', Photomicrograph of non-planar, polymodal saddle dolomite with strong sweeping extinction; crossed-polarized light; (b) U17-M05-3, 116', Photomicrograph of weak development of coarse and finely crystalline bands of saddle dolomite occurring with sulfides; plane-polarized light; (c) D2-100-2 150.3', Photomicrograph of planar-s to non-planar, polymodal saddle dolomite with weak sweeping extinction; Typical example from Dee-Rossi area; crossed-polarized light.

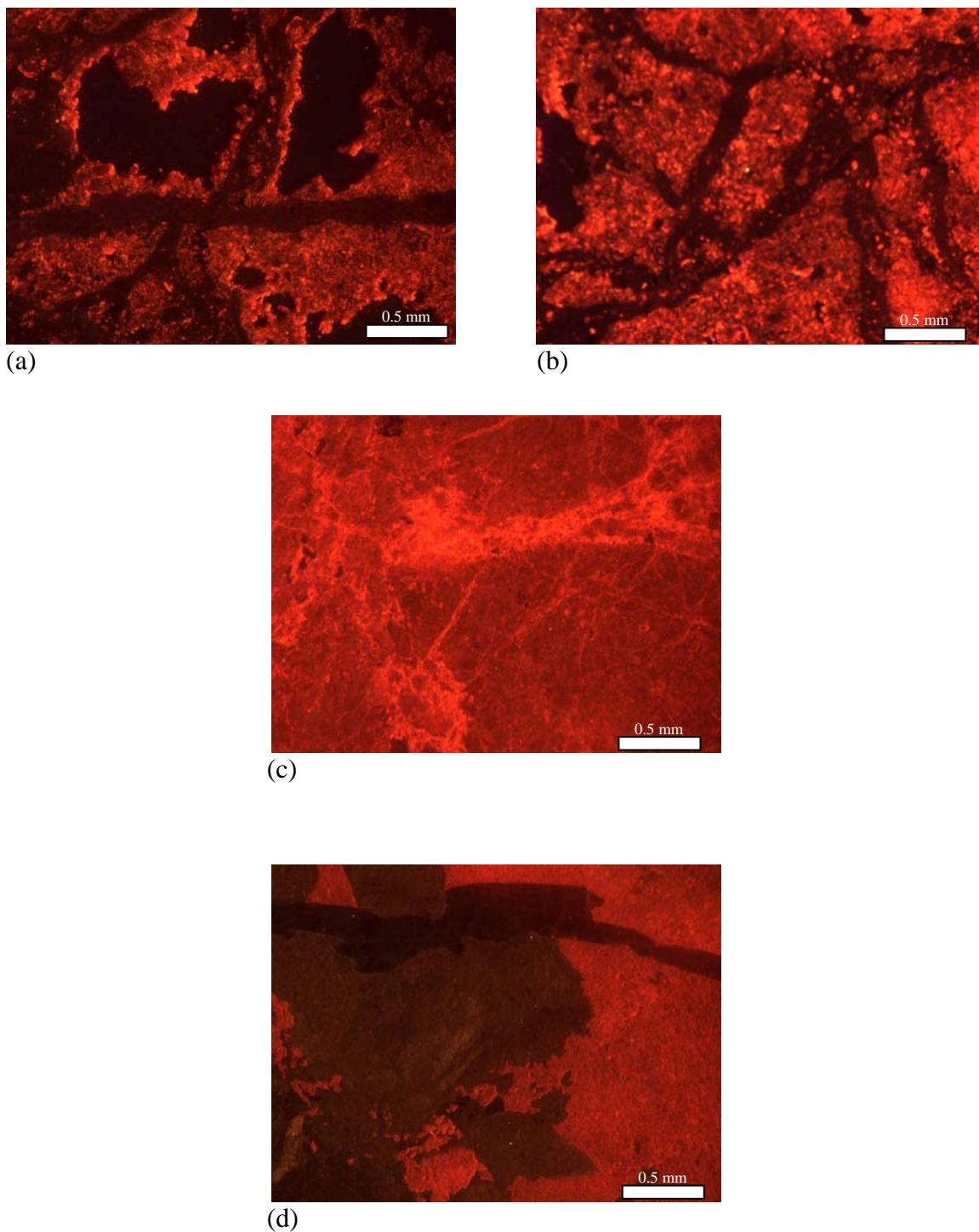


Figure 22: Cathodoluminescence microscopy reveals dissolution textures and intense calcite veining of saddle dolomite. (a, b) U17-M05-3 116', CL images showing dissolution texture and veining in a moderately to brightly luminescent saddle dolomite; (c) U17-M05-3, 150.3', Moderately luminescent saddle dolomite with bright calcite veining; (d) MST-1 1214: CL image of moderately to brightly luminescent saddle dolomite and dull calcite, which is replacing the saddle dolomite.

and have  $\delta^{18}\text{O}$  ‰PDB values averaging -16.4 ‰PDB and light  $\delta^{13}\text{C}$  values average -2.7 ‰PDB (Figure 23).

### **Ferroan Dolomite**

Ferroan dolomite occurs in drill holes intersecting or near the Meikle or Dee-Rossi deposits (Figure 24). Ferroan dolomite is discontinuous in the drill holes sampled for this study and most occurs in or within several feet of brecciated zones. Such breccia zones can be one or two hundred feet in vertical extent.

In core, ferroan dolomite is similar in texture and in color to saddle dolomite. However, ferroan dolomite is most common in rocks with quartz flooding. Zones containing ferroan dolomite are commonly intensely fractured with sooty black sulfide fracture fill. Ferroan dolomite in these zones is white to pink in color and is commonly intergrown with quartz (Figure 25).

Thin-section analysis shows the ferroan saddle dolomite is texturally very similar to saddle dolomite. Ferroan dolomite is non-planar, polymodal and has sweeping extinction, but tends to occur with quartz (up to 60% quartz) more commonly than non-ferroan saddle dolomite. Rocks containing ferroan dolomite have 5-10% porosity and few stylolites (Figure 26).

Cathodoluminescence images for ferroan dolomite are almost identical to CL images taken of saddle dolomite. Ferroan dolomite is moderately luminescent with pervasive dissolution and corroded crystal edges (Figure 27).

Ferroan dolomite isotopic data show most samples clustering between  $\delta^{18}\text{O}$  values -10.2 and -13.5 ‰PDB (mean -12.9 ‰PDB) and  $\delta^{13}\text{C}$  values -2.0 to 1.6 ‰PDB (mean -

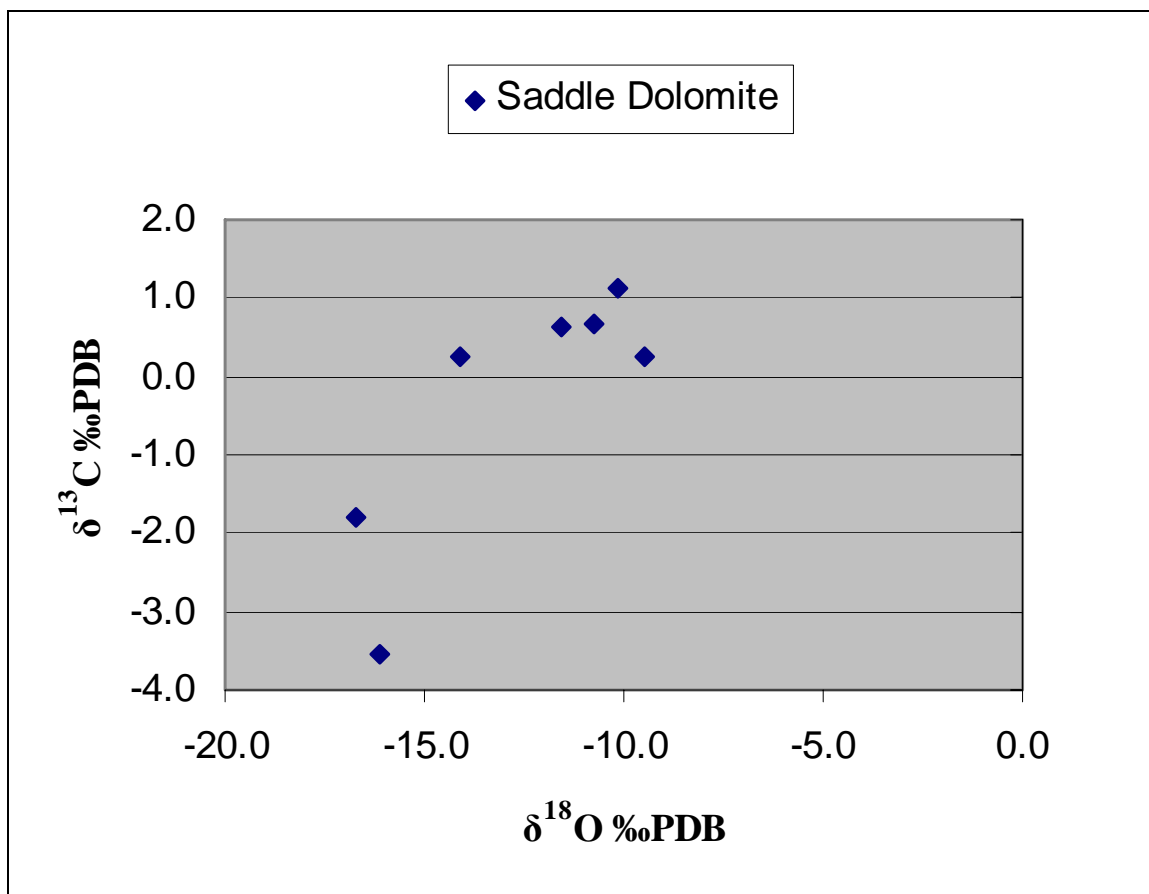


Figure 23: Plot of values for saddle dolomite isotopic data illustrating the close clustering of the majority of samples with a trend towards depleted  $\delta^{13}\text{C}$  values.



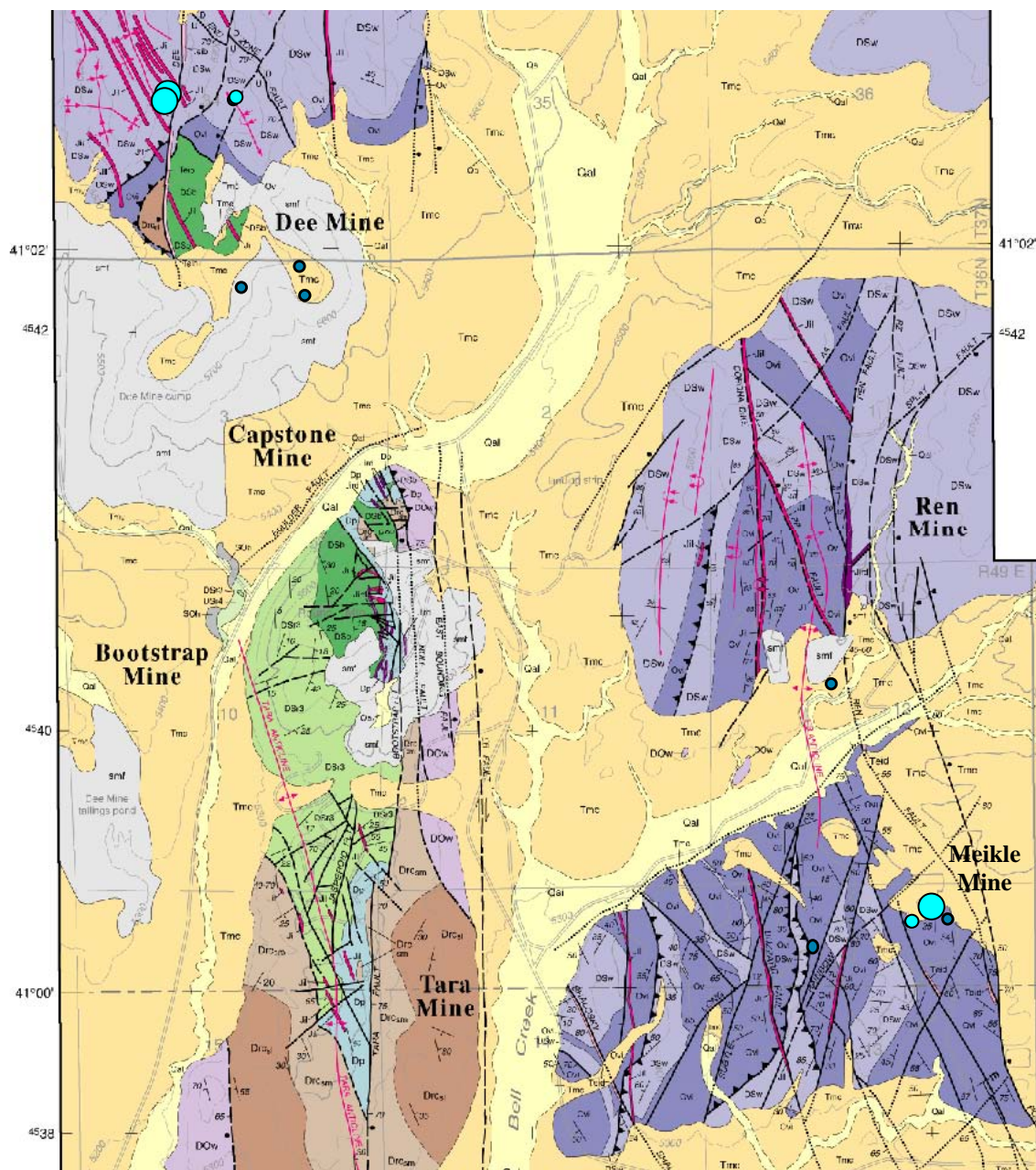


Figure 24: Locations of ferroan dolomite occurrences recognized in this study are marked by blue circles proportional to amount of ferroan dolomite observed (modified from Moore, 2002). Similar to saddle dolomite, ferroan dolomite only occurs near structures or ore bodies.

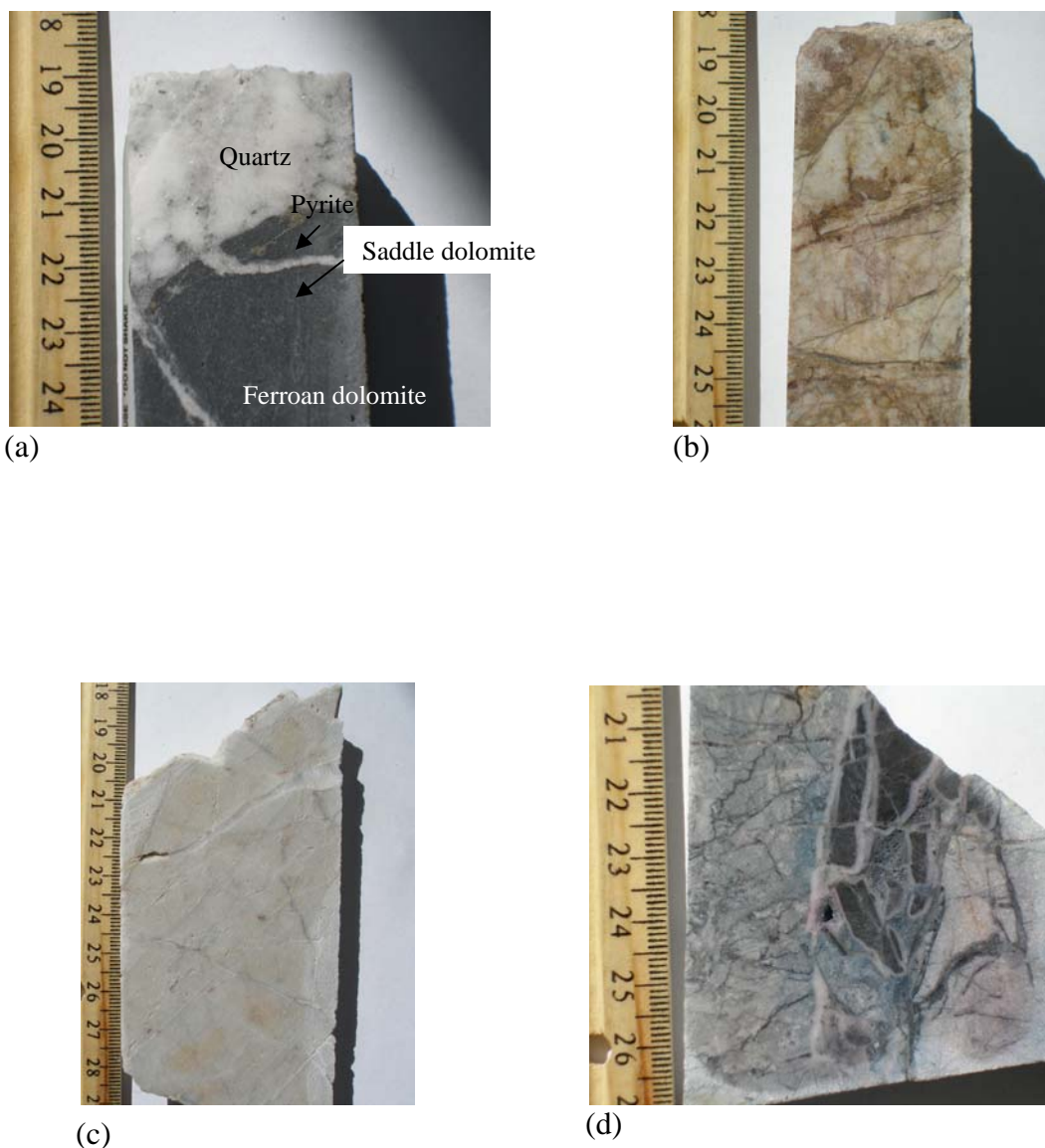


Figure 25: Hand samples of various ferroan dolomite samples. The samples vary significantly in color from gray to pink to white and in fracture intensity. (a) Ex-21c, 1024', Core of finely crystalline, dark ferroan dolomite, coarse, white quartz, and gray to white saddle dolomite vein; (b) D0-100-1, 109', Core of fractured ferroan dolomite with iron oxidation of the fractures; (c) D2-100-2, 266.4', Core of off-white ferroan dolomite with calcite veining; (d) D2-100-2, 4', core of fractured, stylolitized, breccia ferroan dolomite with muddy clasts and silica flooding (blue coloring is stain).

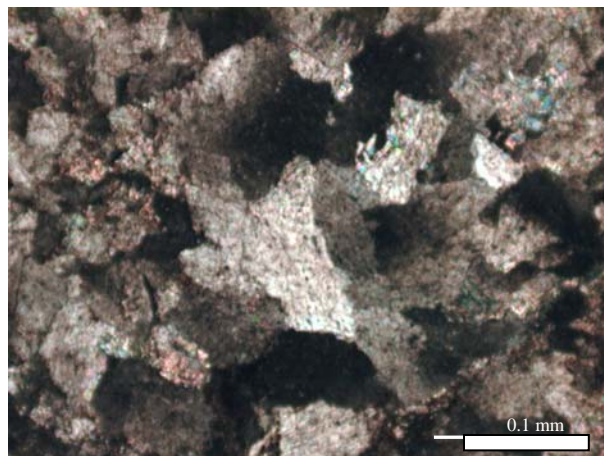


Figure 26: An example of the fabric and texture of ferroan dolomite. D0-100-1, 109', Photomicrograph of planar-s to non-planar, polymodal ferroan saddle dolomite; cross-polarized light.



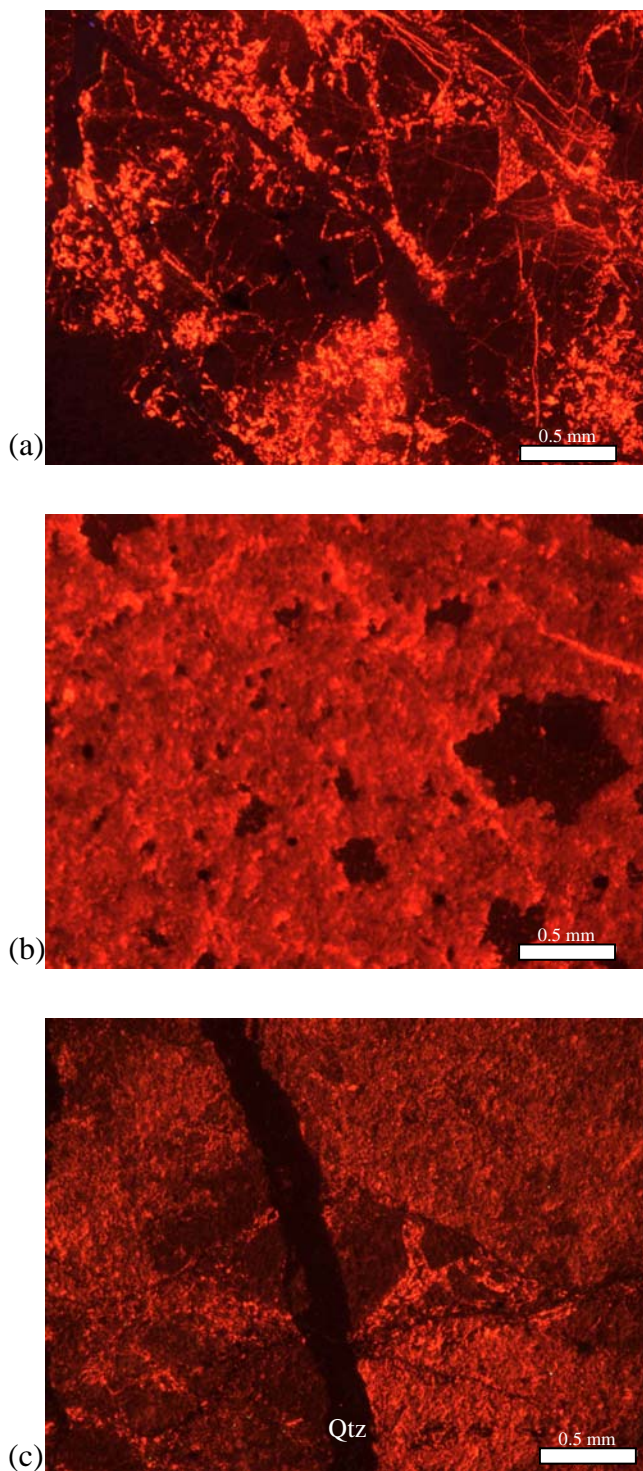


Figure 27: Cathodoluminescence analysis illustrates the dissolution and fracturing of ferroan dolomite. (a) D2-100-2, 4', CL image of ferroan dolomite, moderately luminescent, brightly luminescent material is calcite; (b) BD-52, 1238', CL image of moderately luminescent ferroan dolomite with dissolution vugs; (c) D0-100-1, 109', CL image of moderately luminescent ferroan dolomite with quartz vein (nonluminescent)



0.8 ‰PDB) (Figure 28). A few samples from the Meikle area show depleted values for both  $\delta^{13}\text{C}$  and  $\delta^{18}\text{O}$ .

### **Zebra Dolomite**

Zebra dolomite is not well represented by the samples in this study. Only two samples were collected: one from the Dee-Rossi area and the other from Meikle (Figure 29). In these samples, zebra texture is not particularly well developed. To supplement isotopic data, samples from Dane Evans' master's thesis (Evans, 2000) on the Meikle deposit were used.

The alternating white and gray bands that characterize zebra dolomite are typically irregular and vary in width. The dolomite is coarse, non-planar saddle dolomite in the white bands, and is fine, non-planar dolomite occurring with sulfides and organic matter in the gray bands. In the sample with poorly developed zebra texture, the bands are thin and irregular (gray bands <0.5 mm; white 1 mm wide), and the saddle dolomite is finer, planar-s with weak sweeping extinction. The zebra dolomite that is better developed has thicker bands (gray up to 4 mm; white up to 5 mm wide) and is non-planar with strong sweeping extinction and void space associated with the white bands. Rocks containing zebra dolomite samples have 10% quartz, ~3% porosity and typically have few stylolites, although stylolites are common in the poorly developed zebra texture from Dee-Rossi (Figures 30 and 31).

Cathodoluminescence images show the gray bands with gray, non-luminescent material and the white bands as brightly luminescent with bright crystal edges on the dolomite filling the vugs (Figure 32).

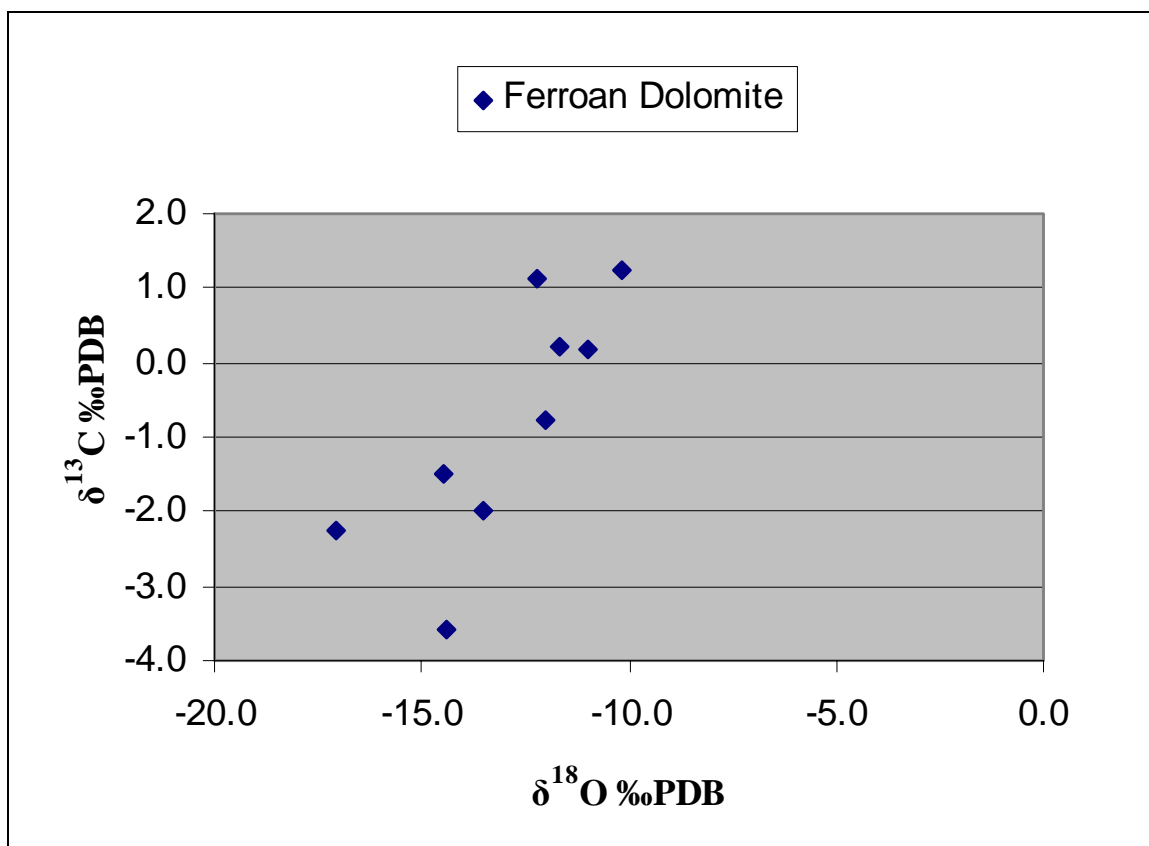


Figure 28: Isotopic data for ferroan dolomite samples showing a trend from more enriched  $\delta^{13}\text{C}$  values to depleted values.

Figure 29: Location of zebra dolomite in drill hole core indicated by blue circles proportional to amount of zebra texture observed (modified from Moore, 2002). Zebra texture is only observed in drill holes directly penetrating ore bodies.

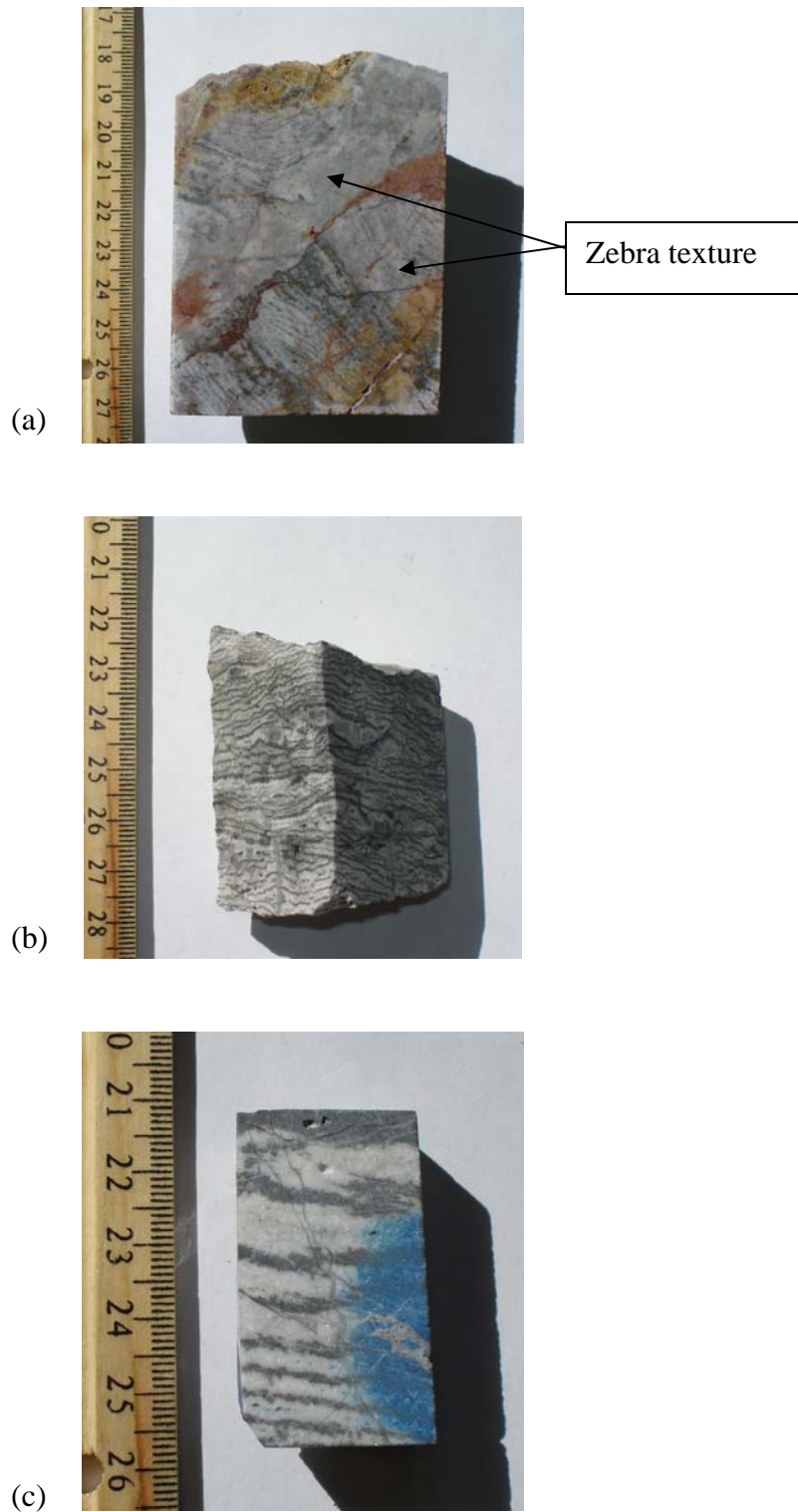


Figure 30: Hand samples of zebra texture dolomite samples illustrate the variation in band thickness and continuity. (a) D0-100-1, 312', Core of poorly developed zebra texture bounded by stylolites with iron oxides, (b) Ex-21c, 1065', Core of zebra texture with irregular banding, (c) Sample from Evans (2000), Core of zebra dolomite with thick gray and white bands of saddle dolomite.

Figure 31: Photomicrographs of zebra textures illustrate the range of fabric and texture seen between poorly developed zebra texture (a, b) and well-developed zebra texture (e, f). (a, b) D0-100-1, 312', Photomicrograph of poorly developed zebra dolomite with coarse, planar-s saddle dolomite and finely crystalline planar-s saddle dolomite occurring with sulfides; (a) plane-polarized light; (b) crossed-polarized light; (c,d) Ex-21c, 1065', Photomicrograph of zebra dolomite with non-planar, coarsely and finely crystalline saddle dolomite; (a) plane-polarized light, (b) cross-polarized light; (e,f) Sample from Evans (2000), photomicrograph of well-developed bands of coarse and fine, non-planar, saddle dolomite with high percentages of sulfides and bitumen occurring with the finely crystalline; (a) plane-polarized light, (b) cross-polarized light.



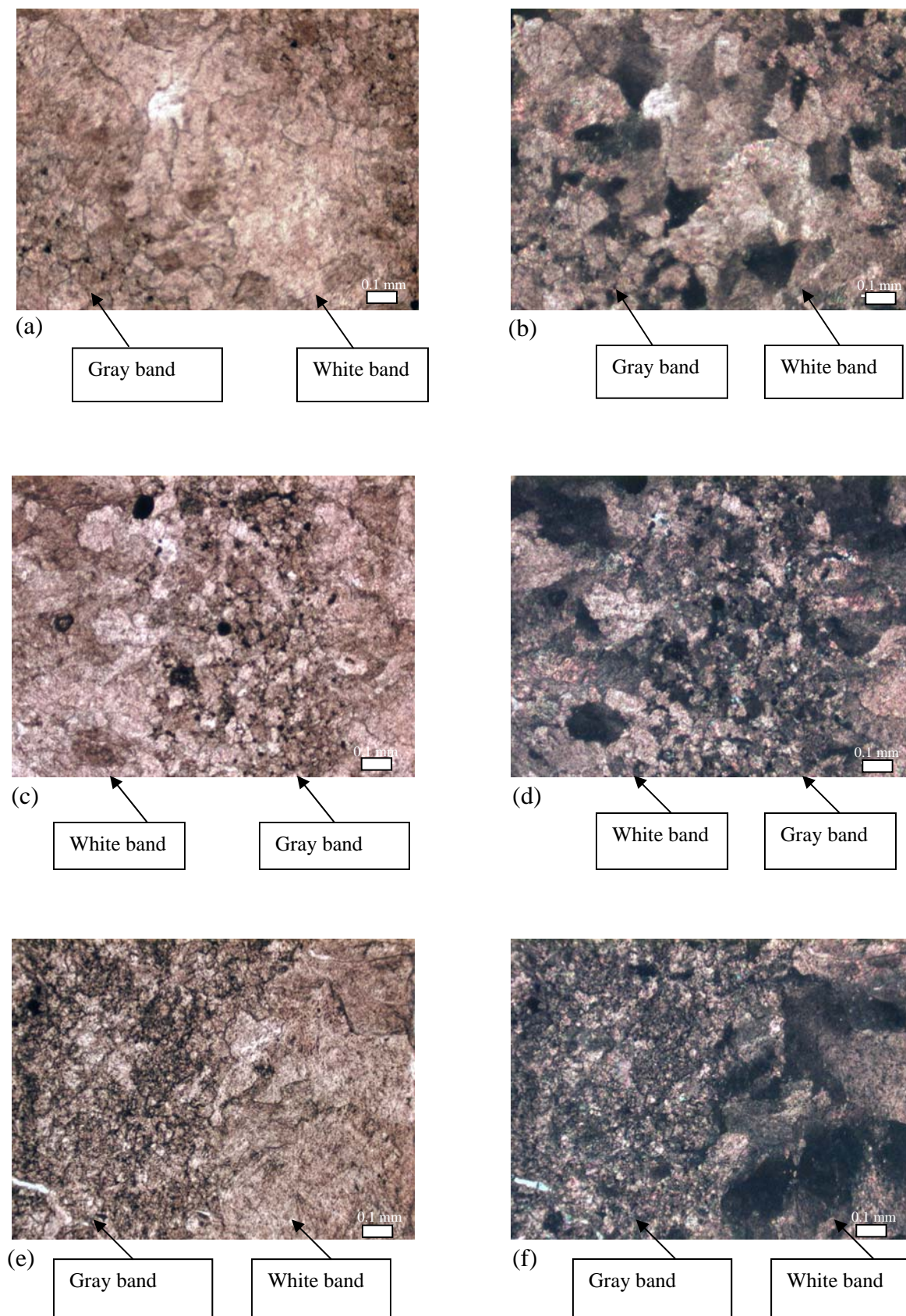


Figure 31

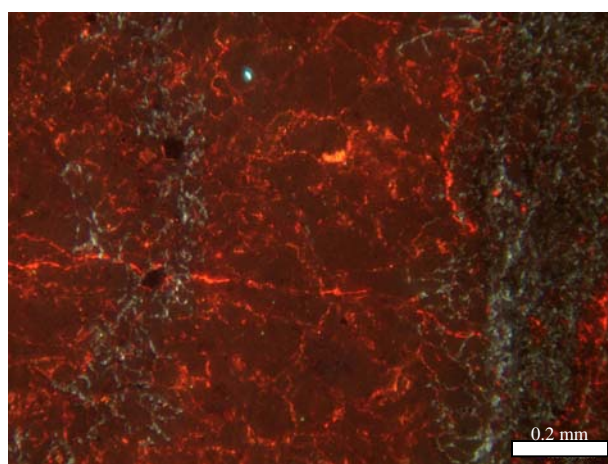
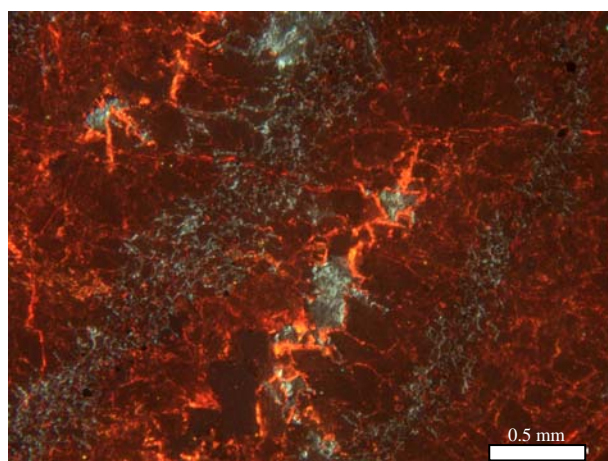


Figure 32: Ex-21c, 1065', CL images of zebra dolomite: white bands are moderately luminescent with bright edges on the saddle dolomite crystal as the crystals extend into void spaces. The gray bands are the non-luminescent gray areas.

Isotopic data for each zebra dolomite sample are divided between light and dark bands. The data for each band of one sample plot very closely to each other (Figure 33). The range of  $\delta^{18}\text{O}$  values is small (-15.9 to -11.9, mean -14.2 ‰PDB), but the values for  $\delta^{13}\text{C}$  have a wide range from -3.8 to -0.09 ‰PDB (mean -2.2 ‰PDB). Depleted  $\delta^{13}\text{C}$  values correspond to the samples with well-developed zebra texture.

### **Calcite**

There are several calcite precipitation events evident from petrographic observations and isotopic data. The earliest calcite is related to early cementation of the limestone, with bladed to equant calcite cementation of grains; this is discussed under the limestone section.

Two more calcite generations are recognized following the early cementation event, and both consist of coarsely crystalline sparry calcite. These generations of calcite occur throughout the study area, although calcite veining is most common in limestone as compared to the dolomites.

In core, calcite fills vugs with crystals up to 5 mm in size, forms large veins several mm wide, and can be the matrix of breccia where coarse calcite supports clasts of limestone (Figure 34).

Thin-section analysis shows that calcite can occur as a cement of coarsely crystalline calcite spar overprinting or destroying original grains. The calcite can also form in veins, fill void spaces and replace skeletal grains (Figure 35a). However, there is significant variation in appearance of calcite veins at this scale. In some samples, the calcite spar is twinned or has clearly defined crystal edges (Figure 35d). In other calcite



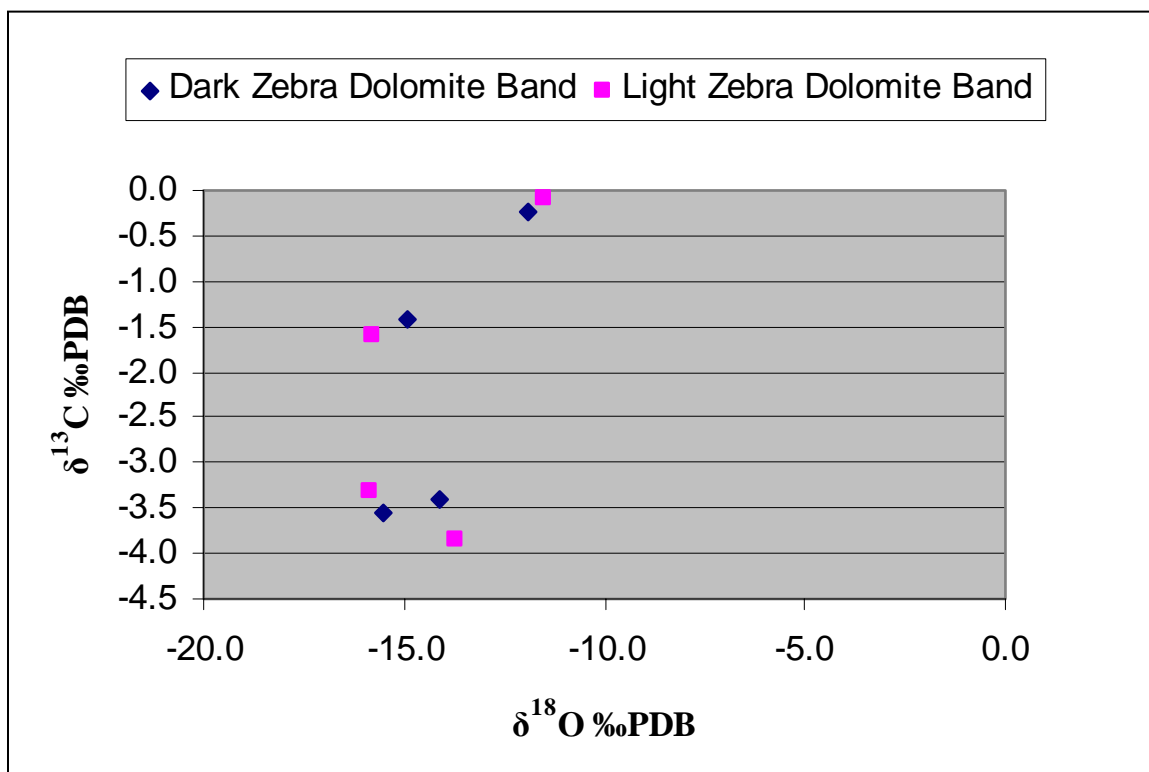


Figure 33: Zebra texture dolomite isotopic data plot illustrates that the samples with the most developed zebra texture have the most depleted  $\delta^{18}\text{O}$  and  $\delta^{13}\text{C}$  values. For each sample, there is a value for white (light) bands and for gray (dark) bands, which plot directly next to each other.



Figure 34: Hand sample illustrating the void-filling late calcite event. U17-M05-3, 122', Core of vug filling late calcite in gray limestone. Calcite is also replacing the crinoid fossils in the limestone.

Figure 35: Late calcite photomicrographs show a wide range of fabrics. (a) BD-178, 1436', Photomicrograph of an edge of a fossil replaced by sparry calcite; crossed-polarized light; (b) GA-65c 3703, Photomicrograph of crossing veins of sparry calcite stained pink; plane-polarized light; (c) U17-M05-3, 122', Photomicrograph of a calcite vein stained pinked and the surrounding fine-grained quartz; cross-polarized light; (d) U17-M05-3, 580', Photomicrograph of twinned sparry calcite filling space between grains as well as destroying original limestone texture; cross-polarized light; (e) D2-100-2, 266', Photomicrograph of a calcite vein stained purple and saddle dolomite; plane-polarized light; (f) BD-178, 1318', Photomicrograph of a calcite vein (stained purple) and quartz; crossed-polarized light.

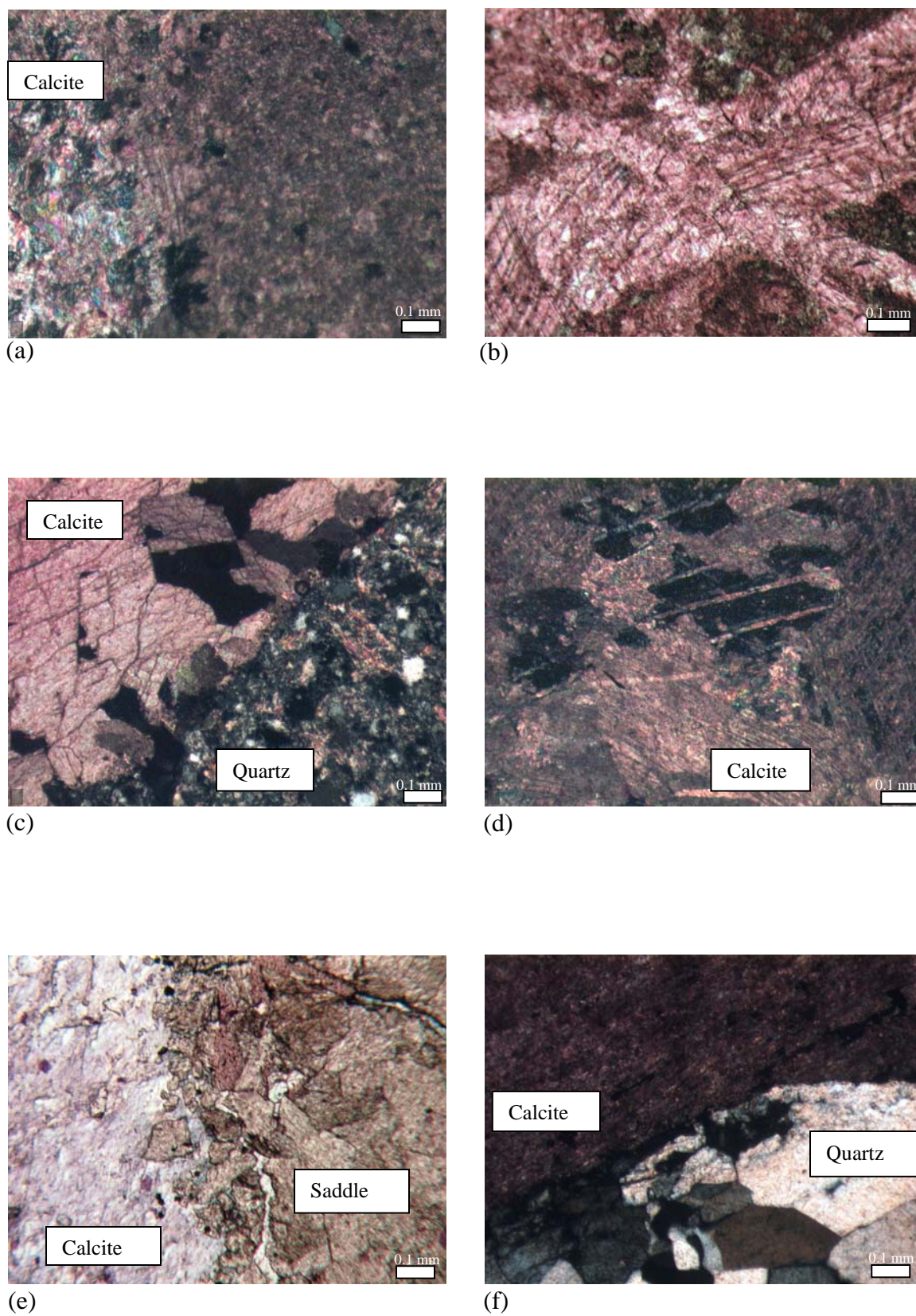


Figure 35

samples, the veins of calcite appear to have undergone partial dissolution that has created irregular crystal shapes (Figure 35c). Calcite can also occur as a replacement of saddle dolomite (Figure 22d).

Cathodoluminescence images of calcite samples show a great variation in CL appearance of individual samples. Calcite is present as brightly to dully luminescent, and can vary from red to yellow in color. CL analysis reveals compositionally zoned cavity-filling calcite, zoned veins, and dissolution features (Figure 36).

Calcite isotopic data show two clusters of values (Figure 37). The first cluster ranges in  $\delta^{18}\text{O}$  values from -13.6 to -4.7 ‰PDB (mean -10.0 ‰PDB) and  $\delta^{13}\text{C}$  values from -0.9 to 2.2 ‰PDB (mean 0.5 ‰PDB). The second cluster has more depleted values with  $\delta^{18}\text{O}$  values from -28.7 to -21.0 ‰PDB (mean -24.5 ‰PDB) and  $\delta^{13}\text{C}$  from 0.4 to 3.3 ‰PDB (mean 0.9 ‰PDB). The cluster of enriched values represents a cement that is commonly twinned. The depleted group of calcite samples appears to have undergone more dissolution or is vug-filling.



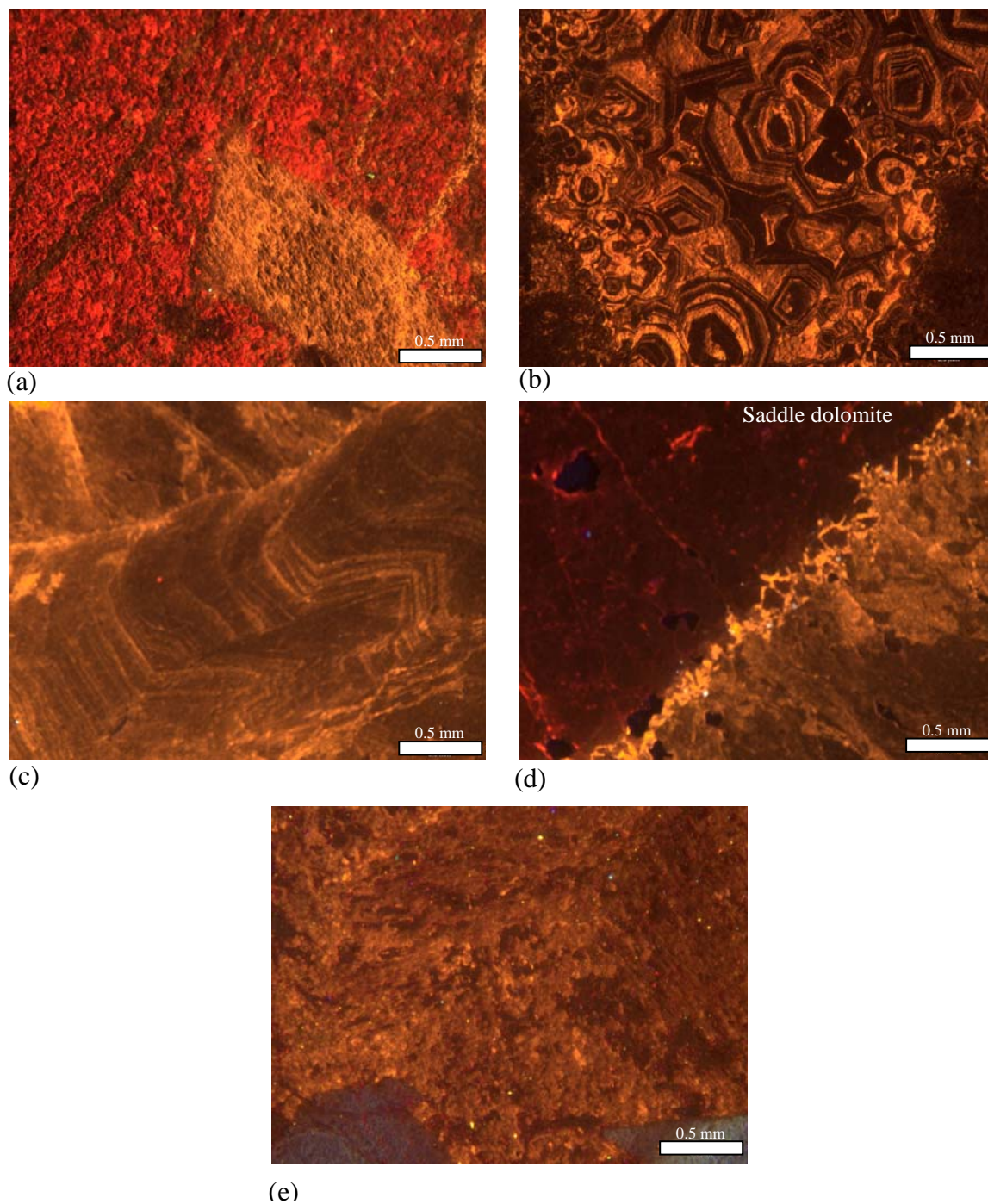


Figure 36: CL images show a wide range of luminescence colors and zoning patterns, reflecting the fabric variations seen in plane-polarized light. (a) GA-65c 3703', CL image of brightly luminescent red and yellow late calcite; (b) BD-177, 1133', CL image of void filling late calcite with compositional zoning; (c) D2-100-2, 266.4', CL image of late calcite vein with zoning; (d) D2-100-2, 266.4', CL image of the edge of a late calcite vein (yellow) and saddle dolomite; (e) BD-178, 1318', CL image of late calcite vein with possible zoning that is now destroyed.

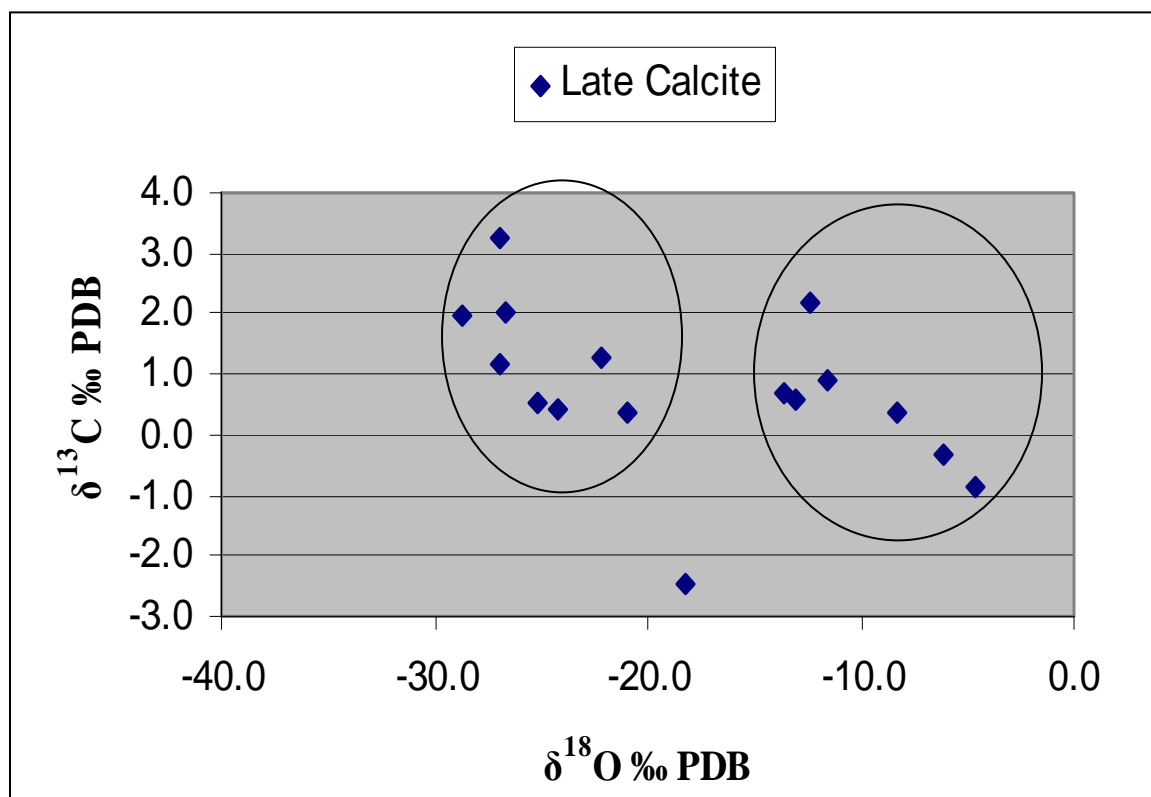


Figure 37: Calcite isotopic data plot in two distinct groups of values, each is circled.



## DISCUSSION

The detailed petrographic and analytical work described in the previous section provides insight to the formation of Carlin-type gold deposits. Most notably, data from this study indicate that (1) the majority of the limestone was not altered to a dolostone before hydrothermal dolomitization and precipitation, (2) there may be two hydrothermal dolomitization events within the area: a Paleozoic dolomitization event at Meikle and a Jurassic-Tertiary hydrothermal dolomitization event at Dee-Rossi, and (3) a pattern of hydrothermal dolomitization can be predicted for Carlin-type deposits.

### **Limestone Interpretation**

Field and laboratory studies show that samples of the Bootstrap limestone are not truly unaltered because of the occurrence of early cementation. The oolitic grainstones have bladed calcite on the surfaces of grains and a blocky, equant calcite cement between grains. These calcite cements are interpreted to represent precipitation from marine fluids penecontemporaneous with deposition, and precipitation in the meteoric phreatic zone or shallow burial environment shortly after deposition, respectively (James and Choquette, 1990; Tucker and Wright, 1990). These early cements would have significantly reduced porosity and permeability in the Bootstrap limestone unit.

Authigenic quartz and dolomite are also present in the limestone. The quartz and dolomite occur as disseminated crystals in the limestone, crosscutting both grains and cement. These disseminated dolomite crystals were likely precipitated deep in the subsurface by formation fluids (e.g., Cantrell and Walker, 1985).

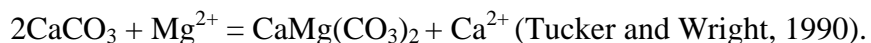
Isotopic data from limestone samples (Figure 38) reflect early cementation of the oolitic grainstones and subsequent calcite precipitation events. These subsequent calcite events caused slightly depleted  $\delta^{18}\text{O}$  values because of precipitation under higher temperatures or from depleted meteoric waters. Using the calcite equation from Friedman and O'Neil (1977), a Devonian seawater range of 0 to -1‰ SMOW Gao (1993), and assuming a normal temperature range for the seawater (20-30 °C), the limestone  $\delta^{18}\text{O}$  values before calcite cementation range from -4.0 to -0.9 ‰PDB.

Four isotope samples have  $\delta^{18}\text{O}$  values of -15.0 ‰PDB or lower, and have either been recrystallized and/or have contamination from a later sparry calcite event (Figure 38). Recrystallization and late sparry calcite events would be related to higher temperature fluids which are reflected by the depleted  $\delta^{18}\text{O}$  values.

### **Dolostone Interpretation**

Diagenetic-planar dolomite occurs in two distributions in the Bootstrap limestone: (1) as disseminated dolomite rhombs as described in the previous section, and (2) as medium-crystalline replacement of limestone.

Dolomite is formed by the addition of  $\text{Mg}^{2+}$  into  $\text{CaCO}_3$ .



The formation of dolomite is not well understood mainly because ordered dolomite is slow growing, making it difficult to precipitate in laboratory studies at surface temperatures and one atmosphere pressure. The main discussions regarding dolomitization models focus on the source of  $\text{Mg}^{2+}$ . Seawater is  $\text{Mg}^{2+}$ -rich, but kinetic parameters prevent dolomite precipitation in normal marine environments (Tucker and

Figure 38: Isotopic plot with associated photomicrographs illustrating the textural differences between samples with varying  $\delta^{18}\text{O}$  values. Two samples (a) and (b) have depleted values reflecting a late calcite event and recrystallization, respectively. The third sample (c) is a typical calcite cemented, peloidal limestone. (a) D0-100-1, 358.5', Photomicrograph of destructive late calcite spar (stained pink); plane-polarized light; (b) U17-M05-3, 291', recrystallized limestone (stained pink) surrounding a saddle dolomite rhomb, plane-polarized light; (c) Sample of Evans (2000). Photomicrograph of peloidal grainstone with equant, blocky calcite cement, plane-polarized light.

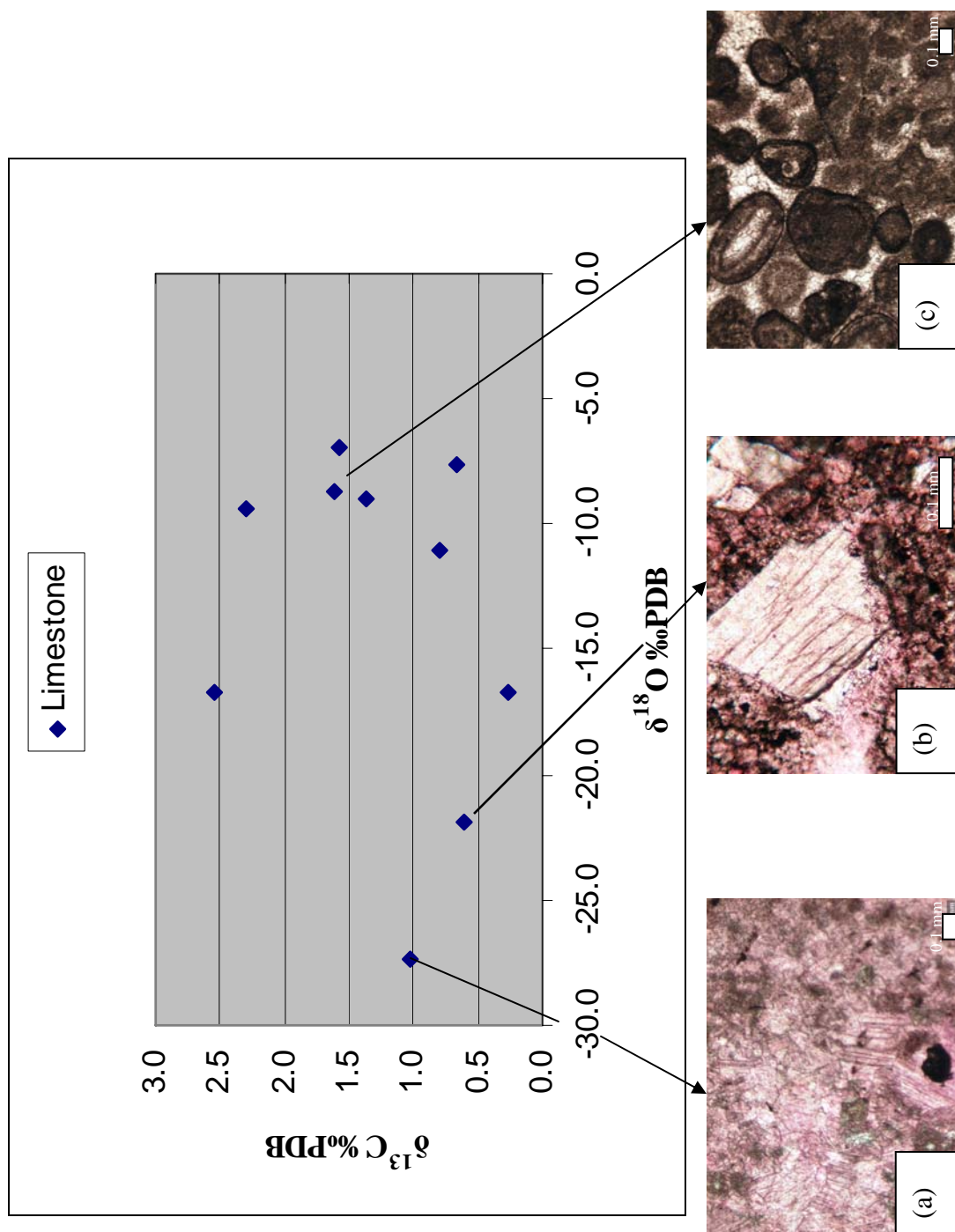


Figure 38

Wright, 1990). There are several models for dolomitization, including a sabkha reflux model, a seepage-reflux model, a marine-freshwater mixing zone model, a burial compaction model and a hydrothermal convection model (Tucker and Wright, 1990).

Armstrong et al. (1998) suggested that the Bootstrap dolostones formed in either an evaporative environment, from burial, or from hydrothermal fluids. Although sabkha structures, such as algal mat laminations, rip-up clasts and intraformational conglomerates, are recognized in limestone portions of the Bootstrap limestone in the Ren area, the dolostones described below the sabkha structures were not likely the result of sabkha-style dolomitization. The location of the dolomite below the sabkha structures does not fit the description of dolomite occurring as a surficial deposit in supratidal zones. The dolomite also does not have evidence of intertidal-supratidal facies or features, such as evaporate pseudomorphs, although these are not always preserved (Tucker and Wright, 1990). In addition, the limestone contains fossils such as corals and bryozoans that represent an open-water environment, not a sabkha depositional environment. The fabric of the dolomite with planar crystal boundaries and lack of high-temperature minerals likewise suggest that a predominantly hydrothermal event was not responsible for this dolomitization.

The burial compaction model is consistent with data from this study. In this model,  $Mg^{2+}$ -rich dolomitizing fluids are expelled from adjacent basinal mudrocks and they flow through platform-margin limestones. The temperature of the limestone and associated fluids increases with burial. Many dolomites form between 80-90 °C because higher temperatures reduce kinetic inhibition for dolomitization (Usdowski, 1994). Proximity of the mudrocks of the Silurian-Devonian Roberts Mountains Formation and

the Devonian Popovich Formation relative to the platform fits the burial compaction model as the source for the necessary  $\text{Mg}^{2+}$ -rich fluids expelled by compaction (Figure 39). The Roberts Mountains and the Popovich Formations represent deeper water deposition along the slope of the shelf. The Roberts Mountains Formation contains laminated, silty limestone representing slope to base-of-slope to distal deposition whereas the Popovich Formation contains debris flows and is dominated by calcareous mudstones and represents deposition in an anoxic, deep-water environment (Furley, 2001).

In the study area, the elevation of the top of the dolostones recognized in the three drill holes is fairly uniform (Figure 40). The percentage of dolomite in each drill hole slowly increases with depth until complete replacement of the limestone is present. This likely represents a diagenetic front whereby ascending fluids expelled from the basin penetrated the Bootstrap limestone. The graditioanl increase of diagenetic dolomite down section in the Bootstrap limestone probably resulted from increasing amount of available fluid and increasing temperatures. The transition from limestone to complete replacement by dolomite extends over a stratigraphic interval approximately 300 feet (92 m) in thickness. The apparent regional distribution of dolomite fits the predicted dolomite pattern in the limestone unit in a burial compaction model (Machel, 2004, 2005). The predicted pattern for burial dolomitization on a regional scale is a broad area of dolomitization near the base of a limestone unit with a limited vertical extent. The location of the dolostones at depth in the drill hole GA-65c, which intercepts the top and bottom contact of the Bootstrap unit, supports that it is the base of the limestone that is dolomitized. The continuation of the dolostone from three drill holes extending west of Meikle to north of Meikle suggests a broad area of dolomitization. The burial model is

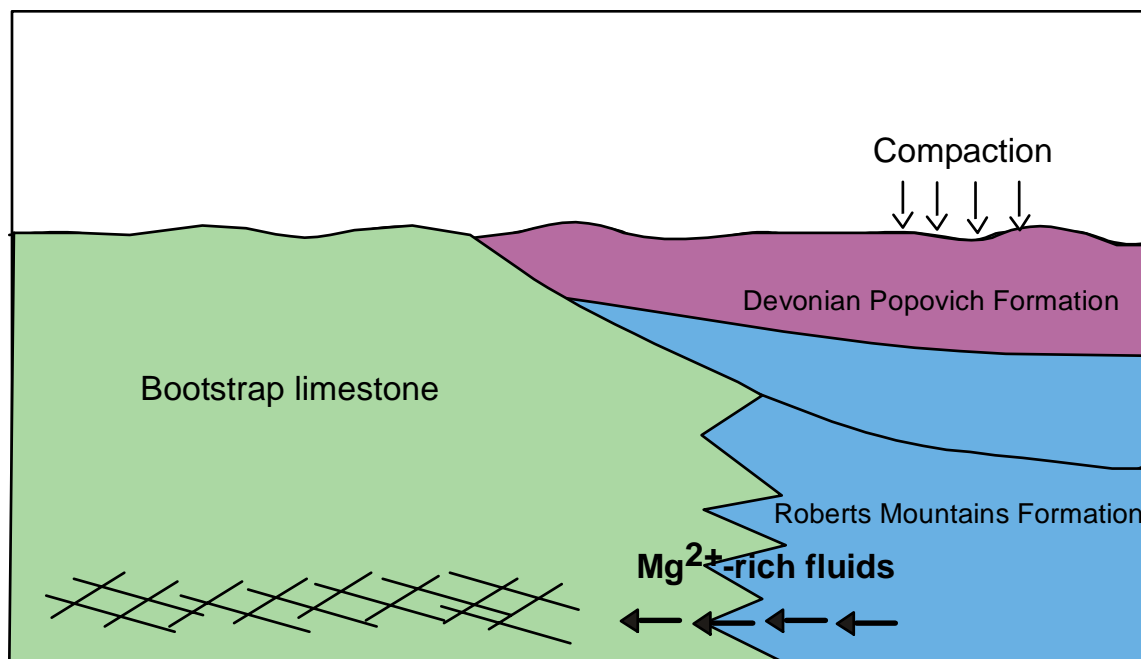


Figure 39: The burial compaction model applied to the study area showing the relationship of the mud-rich Roberts Mountain and Popovich Formations and dolomitizing  $\text{Mg}^{2+}$ -rich fluids relative to the Bootstrap limestone. The Roberts Mountains and Popovich Formations are mud-rich deposits along the slope of the shelf and in the adjacent basin and are the source of dolomitizing fluids. The fluids are expelled by tectonic compression and dolomitize the base of the Bootstrap limestone over a broad lateral area, but are limited vertically (modified from Tucker and Wright, 1990; Furley, 2001; Machel, 2005).



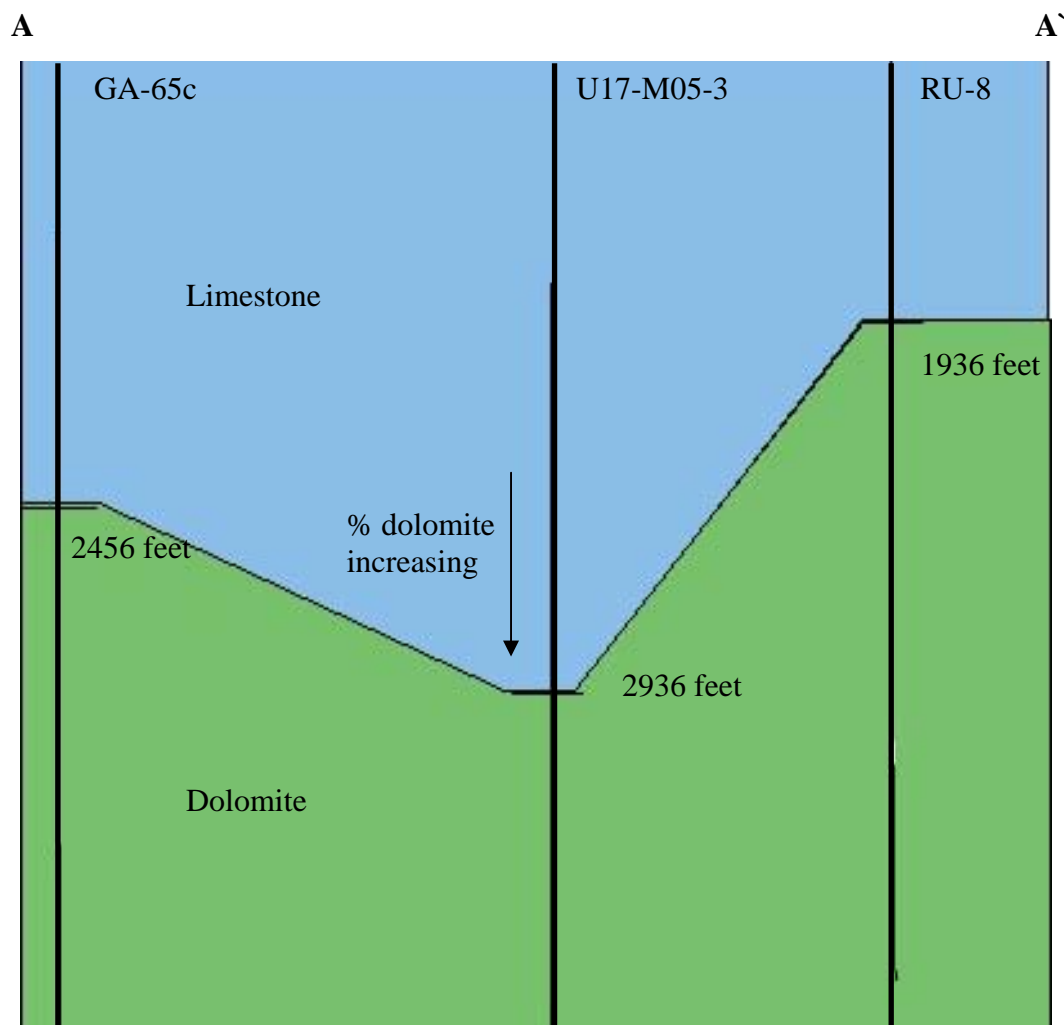


Figure 40. Schematic cross section with the top elevation of dolostone Bootstrap in GA-65c, U17-M05-3, and RU-8 relative to each other. The slow increase of dolomite percentage with depth as well as the uniform, regional nature of the dolostone horizon supports a burial compaction model for dolomitization. RU-8 has been interpreted as faulted by Armstrong et al. (1998), which may explain why the top contact of the dolostone is higher than in the other two drill holes. Upper and lower contacts of the Bootstrap limestone unit are not shown. Cross section location shown in figure 9.

also supported by the uniform CL luminescence of the dolostones. This indicates the fluid forming the dolomite had a relatively uniform chemical composition.

Isotopic data for diagenetic-planar dolomite samples show variations related to the degree of replacement by dolomite (Figure 41). Samples of complete dolomite replacement (Figure 41b) plot with the most enriched  $\delta^{18}\text{O}$  values, indicating a moderate fluid temperature. Using the dolomite fractionation equation from Land (1983), the average  $\delta^{18}\text{O}$  value for diagenetic-planar dolomite (-5.0 ‰PDB), and assuming the fluid composition near Devonian seawater values (0 to -1 ‰SMOW; Gao, 1993), the temperature of the dolomitizing fluids was between about 61 °C and 55 °C. This moderate fluid temperature supports a burial model (Muechez and Viaene, 1994).

Data for partial replacement of the limestone (Figure 41a) plot in the center of the data range, reflecting a physical mix of calcite and dolomite. Samples that are actually borderline saddle dolomite (or non-planar) have depleted  $\delta^{18}\text{O}$  values, probably reflecting a later hydrothermal fluid that is unrelated to the  $\text{Mg}^{2+}$ -rich fluids released from compaction of the adjacent basinal mudrocks.

### **Saddle and Ferroan Dolomite Interpretation**

The majority of non-planar dolomite in the study area is saddle dolomite, which is enriched in calcium with variable amounts of magnesium and iron; it typically forms between temperatures of 80-150 °C (Radke and Mathis, 1980). The dolomite mineral lattice has alternating layers of Ca and Mg cation sites with Ca substituting for Mg in the Mg layers of the crystal lattice in the formation of saddle dolomite. This substitution induces dislocations that form a warped lattice because Ca ions are larger than Mg ions.

Figure 41: Isotopic plot for planar dolomite values with photomicrographs illustrating the fabric variations. Photomicrographs (a) and (b) show the difference in  $\delta^{18}\text{O}$  values for partial replacement and complete replacement of limestone. The photomicrograph for (c) illustrates the correlation between depleted  $\delta^{18}\text{O}$  values and nonplanar fabric. (a) U17-M05-3, 785', Photomicrograph of partial planar-e dolomitization and calcite (stained pink); plane-polarized light; (b) RU-8, 3520', Photomicrograph of non-planar dolomite unrelated to burial dolomitization; crossed-polarized light; (c) U17-MO5-3, 1380', Photomicrograph of complete replacement; plane-polarized light.

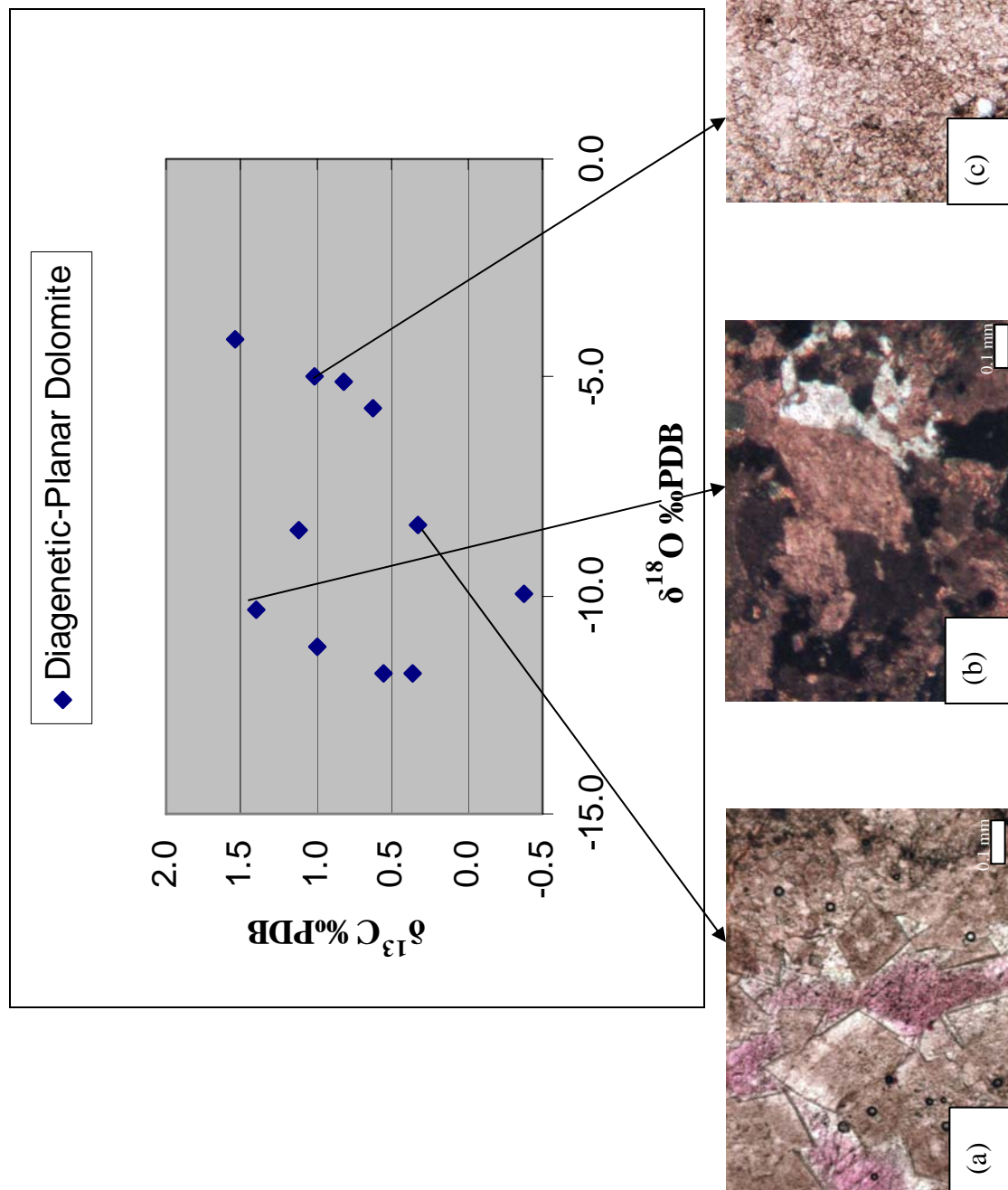


Figure 41

This warped lattice results in the curved crystal shapes and sweeping extinction that are characteristic of saddle dolomite (Searl, 1994). Saddle dolomite commonly occurs with solid bitumen and elemental sulfur, has depleted carbon isotope ratios and is commonly associated with Mississippi Valley-type Zn-Pb deposits (Machel, 2004). In the study area, saddle dolomite occurs as a replacement, as a cavity-fill, in veins, and as scattered rhombs.

Hydrocarbons and dissolved sulfate are thermochemically unstable together so sulfate is reduced by hydrocarbons via thermochemical sulfate reduction (Machel, 2004). The presence of dissolved sulfate inhibits the replacement reaction of calcite to dolomite (Baker and Kastner, 1981; Morrow and Abercrombie, 1994). The sulfate reduction reaction produces alkalinity, which promotes dolomitization and, with high temperatures, can result in the formation of saddle dolomite (Lippman, 1973).

Saddle dolomite takes up Ca, but Fe is closer in size to Mg, so Fe is preferentially partitioned into the dolomite lattice where available (Tucker and Wright, 1990; Searl, 1994). Where the amount of Fe partitioned into the dolomite lattice creates more than 2 mole %  $\text{FeCO}_3$ , it is considered ferroan dolomite. Ferroan dolomite forms under reduced conditions because only ferrous iron is partitioned into the carbonate lattice. This is because ferrous iron has the same valence state as the Mg ion it is replacing. Ferroan dolomite is relatively unstable and subject to dissolution (Purser et al., 1994); during dissolution, Fe is liberated for the sulfidation that accompanies gold mineralization.

Saddle dolomite in this study varies in terms of degree of lattice distortion. The samples with the greatest curved boundaries typically occur near Meikle and with high concentrations of organic matter. This is related to the Paleozoic base-metal

mineralization event and the role of hydrocarbons as discussed above. In the study area, saddle dolomite differs by deposit area, with the non-planar saddle dolomite occurring near Meikle and the planar-s to non-planar saddle dolomite occurring near Dee-Rossi.

Ferroan dolomite samples are similar to saddle dolomite sample in terms of texture and fabric. This is expected because of the similar relationship between the Ca and Fe ion substituting for Mg. Ferroan dolomite is not common in the drill holes examined in this study but occurs more rarely than saddle dolomite. Its relative rarity most likely reflects a lack of available Fe for formation of ferroan dolomite. The greatest difference between the saddle and ferroan dolomite samples is the affiliation of ferroan dolomite with high concentrations of quartz.

Cathodoluminescence images of saddle and ferroan samples are almost identical. Both are moderately luminescent and commonly have brightly luminescent calcite veining. The ferroan dolomite samples should have a dull luminescence, because significant amounts of Fe tend to quench the luminescence. However, the lack of royal blue stain on hand samples and moderate luminescence indicate Fe values are relatively low in the samples collected for this study.

Cathodoluminescence analysis also reveals that the saddle and ferroan dolomite samples have undergone significant dissolution. The unstable nature of these dolomites from cation substitution makes them susceptible to dissolution. This is one process that has created secondary porosity in the tight Bootstrap limestone unit.

Isotopic compositions of well-developed saddle dolomite samples are similar to the samples that do not have well-developed curved boundaries or sweeping extinction (Figure 42). The values that plot with depleted  $\delta^{13}\text{C}$  represent samples from near Meikle,

Figure 42: Isotopic data for saddle dolomite with photomicrographs show a relationship between isotope values and fabric variations. The samples with more enriched  $\delta^{18}\text{O}$  and  $\delta^{13}\text{C}$  values have non-planar-s crystals and weak sweeping extinction; samples with depleted isotopic values have increasing curved crystal boundaries and strongly developed sweeping extinction. (a) U17-M05-3, 116', Photomicrograph of non-planar saddle dolomite with strong sweeping extinction, crossed-polarized light; (b) D2-100-2, 150.3', Planar-s to non-planar, saddle dolomite with weak sweeping extinction; crossed-polarized light.



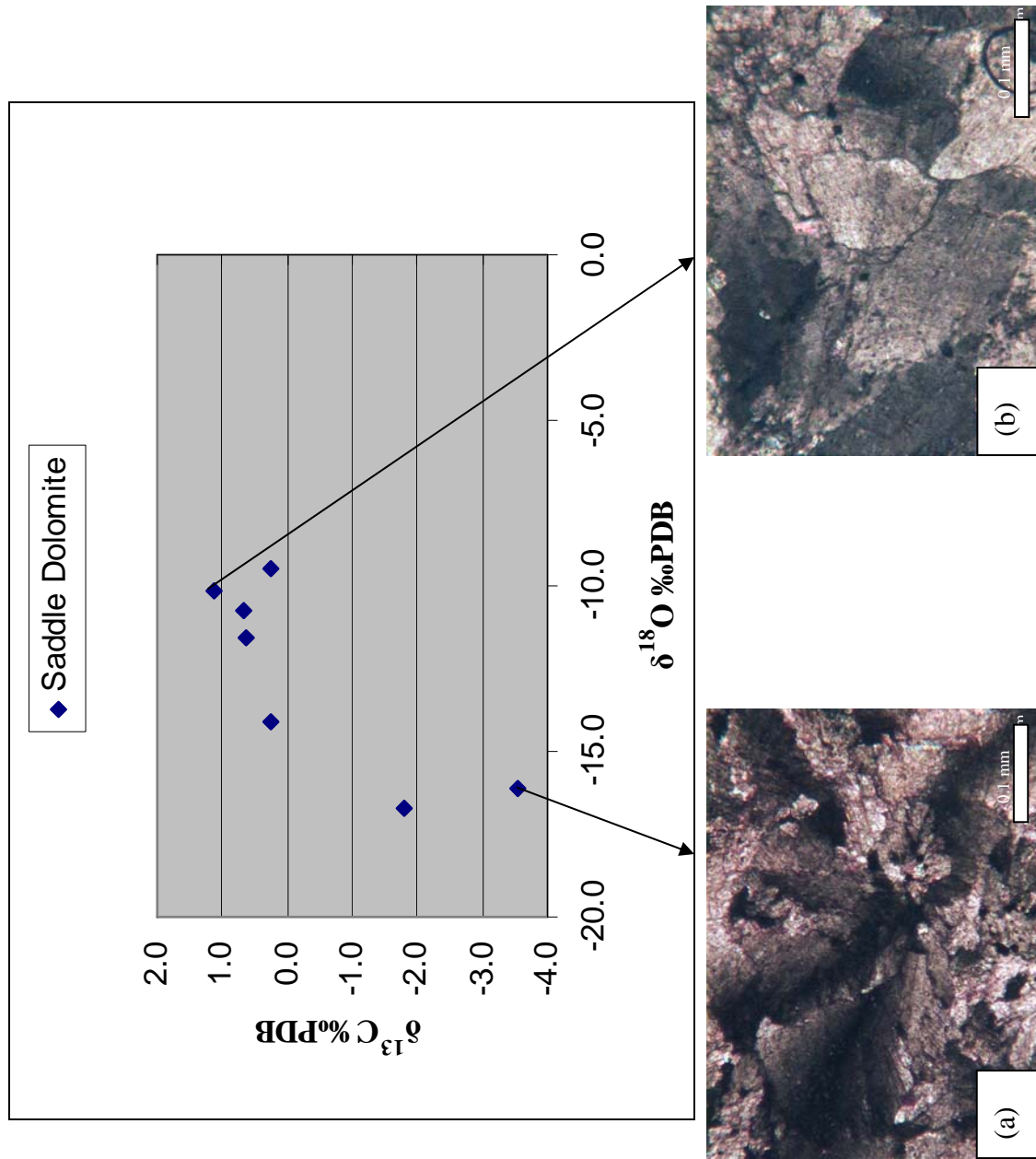


Figure 42

with higher concentrations of organic matter. There is an apparent relationship, based on this isotopic data, that the boundaries of saddle dolomite are increasingly curved if associated with hydrocarbon migration and base-metal mineralization, and this event is more pronounced in the area of Meikle than Dee-Rossi.

Ferroan dolomite isotopic values plot closely to saddle dolomite values, but display a trend toward lighter  $\delta^{13}\text{C}$  values that correlates to samples with more organic matter (Figure 43). The trend reflects the observation that organic matter makes more Fe available for substitution in the dolomite lattice and/or reduces sulfate, which encourages dolomite formation. These depleted  $\delta^{13}\text{C}$  ferroan dolomite samples are from near the Meikle deposit where the hydrocarbon event and base-metal mineralization are clearly recognized (Evans, 2000). Samples with depleted  $\delta^{13}\text{C}$  values are also those that stain bluer in hand sample, qualitatively indicating a higher Fe concentration. The differences in  $\delta^{13}\text{C}$  values for samples from Meikle and Dee-Rossi also suggest that the fluids responsible for dolomitization in each area resulted from two separate events. The  $\delta^{13}\text{C}$  and  $\delta^{18}\text{O}$  values for samples near Dee-Rossi are similar to the values for the limestone wall rock, suggesting that the dolomitizing fluids had extensive interaction with the host material. For saddle and ferroan dolomite,  $\delta^{18}\text{O}$  values are depleted, reflecting precipitation from higher temperature fluids.

The temperature at which saddle dolomite forms and the curved crystal boundaries can both indicate that saddle dolomite is formed by hydrothermal processes. Hydrothermal dolomite is traditionally defined as forming at a temperature 5-10 °C above the temperature of surrounding host rocks (Stearns et al., 1935; White, 1957). Calculation of the temperature of the dolomitizing fluids associated with the saddle, ferroan, and

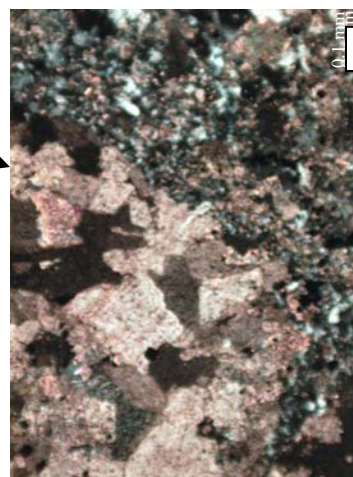
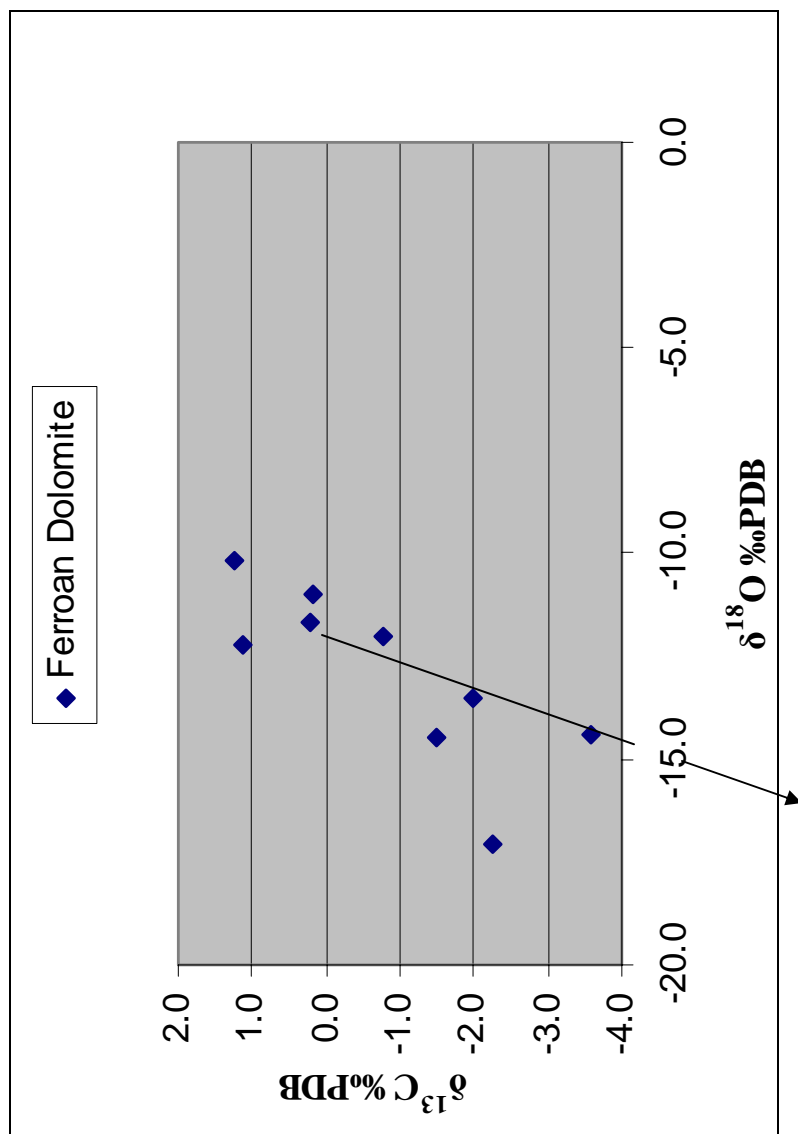


Figure 43: Plot of isotopic data for ferroan dolomite samples with photomicrograph of sample D2-100-2, 4', illustrating the relationship of ferroan dolomite, quartz, and the non-planar to planar-s fabric of ferroan dolomite; cross-polarized light.

zebra dolomites using isotopic data yielded temperatures ranging from 89 °C to 166 °C. Because the composition of the dolomitizing fluids is not known, a range of  $\delta^{18}\text{O}$  values from +2 to -2 ‰SMOW was assumed and the dolomite fractionation equation from Land (1983) was used. Even with a wide range of values used, the data support that this dolomitizing event was at least 20 °C warmer than the previously mentioned diagenetic-planar dolomite event that occurred at a maximum of 61 °C. A 20 °C difference between diagenetic and saddle, ferroan, and zebra dolomites clearly classifies these dolomites as hydrothermal. This calculated temperature difference is supported by the (1) proximity of saddle dolomite, ferroan dolomite, and zebra dolomite to igneous intrusions and faults; (2) the curved crystal boundaries and sweeping extinction of these dolomite types, as well as (3) the occurrence of associated sulfides.

### **Zebra Texture Dolomite Formation**

The alternating white and gray bands of saddle dolomite and ferroan dolomite that comprise the zebra textures in this study are similar in texture and fabric to the saddle and ferroan dolomites described above. This indicates similar conditions for dolomitization of all three types. Although samples in this study do not exhibit well-developed zebra textures or stain a royal blue in hand sample, the finely-crystalline gray bands are inferred to be ferroan dolomite based on work by Emsbo (1999), who found that the gray bands have 5-10 wt. % FeO, while the white bands contained only 0.01 to 1 wt %FeO. Dull luminescence of the gray bands in CL also supports the conclusion that the gray bands are ferroan. Cathodoluminescence observation also reveals that crystal edges of the white bands are brightly luminescent and extend into void space, indicating that the dolomite

crystals were growing into open space. Zebra textures are commonly associated with dolostone host rock. However, the fact that zebra texture dolomite is in direct contact with unaltered limestone, as well as recognition of the dolostone horizon near the base of the Bootstrap unit, is evidence that formation of dolostones before zebra texture is not necessary.

The pattern of alternating white and gray bands has several possible explanations, including precipitation within karst cavities (Horton and De Voto, 1990), early diagenetic environments (Fontboté and Amstutz, 1983), replacement of host rock (Wallace et al., 1994; Leach et al., 1996; Nielsen et al., 1998), or the pattern may represent displacive veins (Merino et al., 2006). Although karsting is common in the region and creates secondary porosity at the upper contact of the Bootstrap limestone, zebra texture does not seem to be filling karst cavities. Zebra texture is not formed early in the diagenetic history either, as demonstrated by unaltered limestone in sharp contact with zebra texture, and also because of the presence of saddle dolomite. Displacive veins may explain the texture forming in this area, but the lack of associated stylolites with zebra texture and the lack of evidence indicating that ferroan dolomite bands are veins discourage this model.

Data from this study support a model for zebra development involving replacement of host rock and/or displacive veins. Replacement can mimic original stratification of the host rock (Leach et al., 1996). However, this cannot be the case in the massive Bootstrap limestone that has no bedding features. Vugs that are in the center of the white bands indicate that the dolomite has filled into open pore space. Nielsen et al. (1998) suggested a model where the gray bands represent replacement and the coarsely crystalline white bands fill fractures related to tectonic compression. This model seems to

be supported by a sample from drill hole Ex-21c, in which finely crystalline ferroan dolomite with associated sulfides is cut by a coarsely crystalline, white saddle dolomite vein (Figure 44). Zebra textures in this area suggest that ferroan dolomitization occurs first and then undergoes saddle dolomite vein formation. Evans (2000) studied the zebra texture that occurs at the Meikle deposit and observed that the zebra texture did not fit current models, but neither did he suggest a model for their formation. The author did, however, relate formation of zebra texture to the alteration of the limestone by hydrothermal fluids associated with a base-metal mineralization event.

Isotopic data for samples displaying zebra textures correlate with the degree of development of the zebra texture (Figure 45). Heavier  $\delta^{13}\text{C}$  values are associated with a poor development of the texture near Dee-Rossi. Samples with strong zebra texture from near Meikle plot with lighter  $\delta^{13}\text{C}$  values (Figure 46). The depletion of  $\delta^{13}\text{C}$  values again correlates with a greater concentration of organic matter near Meikle, as well as substitution of Fe and Ca into the dolomite lattice. Values for the zebra texture plot very closely to the values for samples of saddle dolomite and ferroan dolomite, suggesting that the fluids responsible for creating all three dolomite types were closely related. Therefore, however zebra texture forms, it is not very different from saddle and ferroan dolomitization that does not form bands.

### **Calcite Generations**

There are at least two sparry calcite events that are not related to early diagenetic events. The first event overprints original texture and/or replaces skeletal grains in the limestone and is destroyed by hydrothermal precipitation of dolomite. The second is the

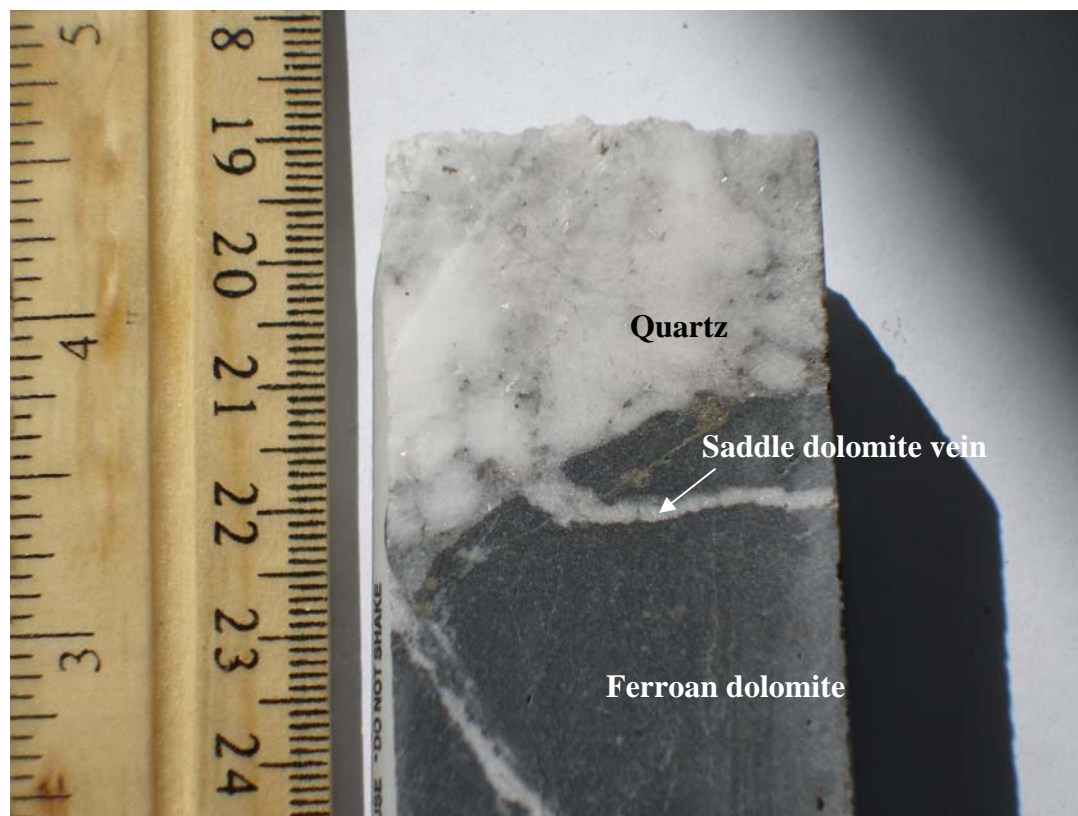


Figure 44: Core of Ex-21c, 1024' illustrating the cross-cutting relationship of a white saddle dolomite vein across finely crystalline, grey ferroan dolomite. This relationship may play a role in understanding how zebra textures form.



Figure 45: Isotopic data for zebra dolomite correlates with the development of the alternating bands and fabric. Reflecting data from saddle and ferroan dolomite samples, photomicrograph (a) illustrates the relationship between depleted isotopic values and non-planar crystal boundaries; photomicrograph (b) reflects the non-planar to planar-s dolomite crystal associated with more enriched isotopic values. (a) Ex-21c 1065', Photomicrograph of poorly developed zebra; crossed-polarized light; (b) D0-100-1, 312', Photomicrograph of well-developed zebra texture; crossed-polarized light.

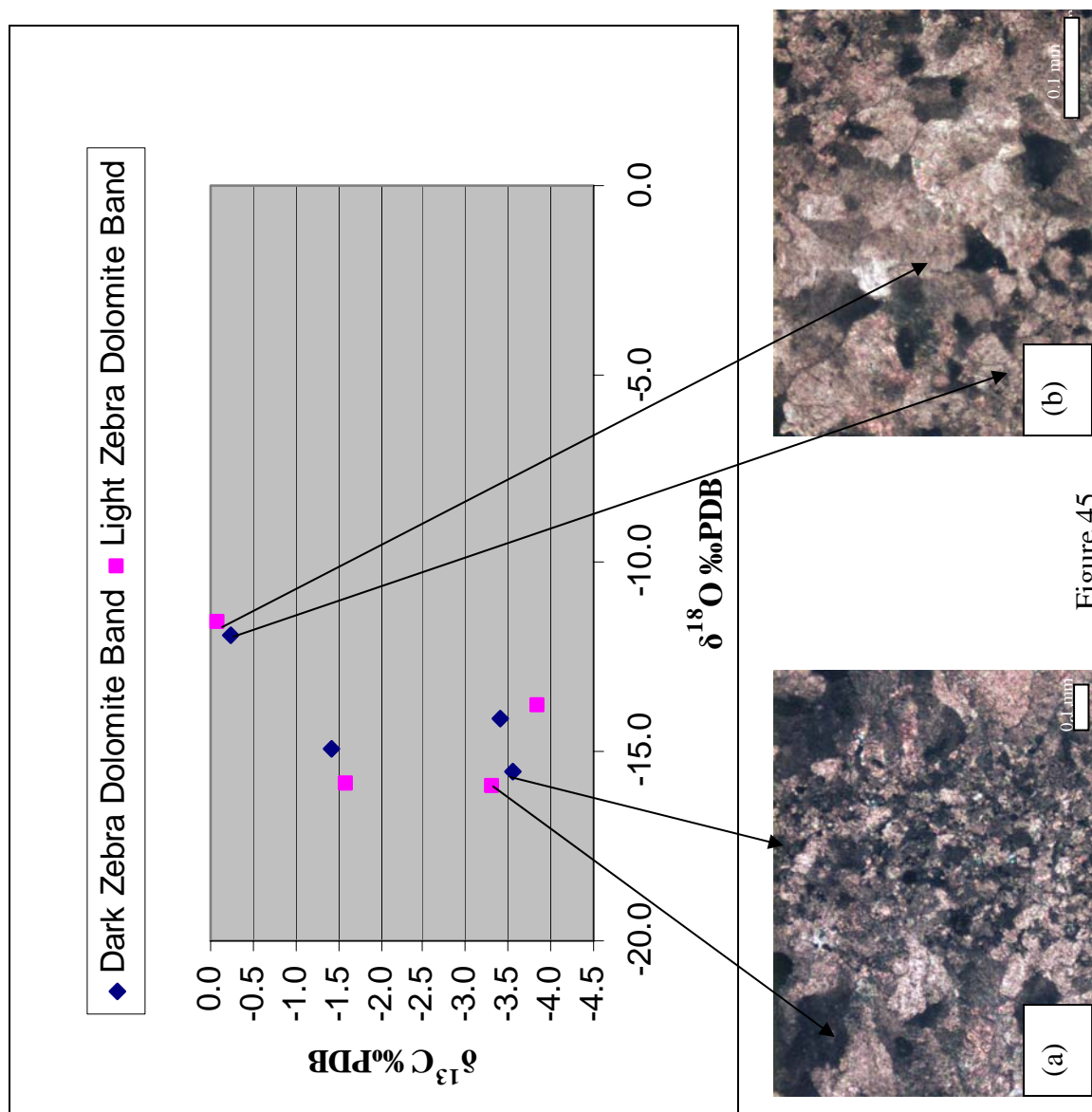
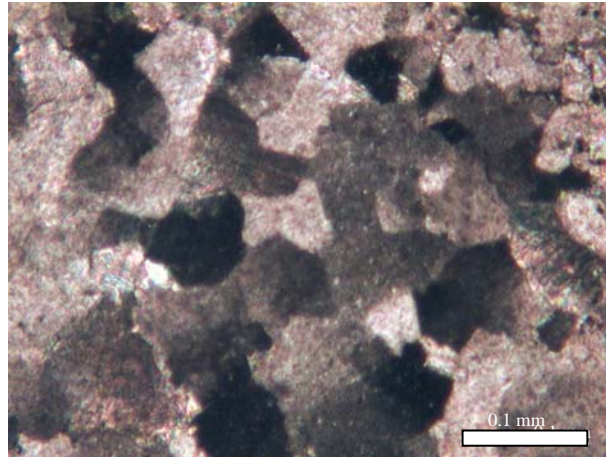
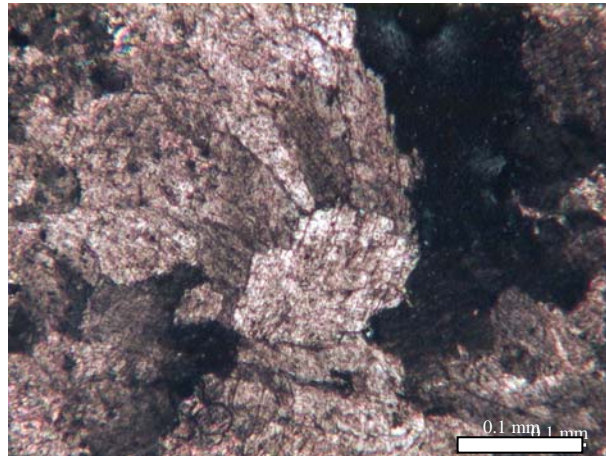


Figure 45



(a)



(b)

Figure 46: Photomicrographs of (a) D0-100-1, 312' and (b) Ex-21c, 1065' coarsely-crystalline white saddle dolomite bands in zebra texture emphasizing the difference in samples without a hydrocarbon association (a) and a sample that does occur with hydrocarbons (b). Sample (a) does not have as well as developed curved crystal boundaries or sweeping extinction as sample (b).

youngest hydrothermal event in the region and is related to the precipitation of coarsely crystalline calcite into voids, and cross-cuts hydrothermal dolomites. This young hydrothermal calcite also occurs in veins that clearly show zoning in CL. These veins can stain purple indicating elevated Fe concentrations, and they exhibit dissolution fabrics petrographically and in CL. The calcite events have a wide range of luminescence colors varying from bright reddish to bright orange. The late hydrothermal calcite is also responsible for calcification of saddle dolomite (dedolomitization). Most likely, the material necessary for both calcite events comes from dissolution of the host rock; this cycle of dissolution and precipitation continues to the present.

Isotopically, the early sparry cement is represented by moderate  $\delta^{18}\text{O}$  values relative to early diagenetic calcite cement, and the strongly depleted  $\delta^{18}\text{O}$  values (-20 to -30 ‰) represent the late void-filling sparry cement (Figure 47). The depleted values of vein- and void-filling calcite cements represent a very high temperature fluid. Using the Friedman and O'Neil (1977) calcite fractionation equation, assuming a depleted meteoric-derived fluid of -10‰ SMOW, and using the average of the second calcite generation (-25‰ PDB or 5.1‰ SMOW) yields a calculated temperature of 120 °C. This calculated temperature suggests the water source is deeply convecting meteoric water.

### **Generations of Silica Deposition**

There are several quartz-emplacement events recognized in this study, but the timing of silicification of the limestone is not well constrained. Quartz ranges from fine-grained to coarse-grained drusy crystals and occurs in veins as well as a destructive, massive flooding event. Observations from this study corroborate the two quartz events

Figure 47: Isotopic data for the two recognized calcite generations with associated photomicrographs. Sample (b) illustrates the destructive calcite veining common in limestones and sample (a) illustrates the second calcite generation of late calcite veins that post-date hydrothermal dolomitization and has severely depleted  $\delta^{18}\text{O}$  values. (a) D2-100-2, 266', Late calcite vein (stains purple) and saddle dolomite; plane-polarized light; (b) GA-65c, 3703, Crossing veins of late calcite (stained pink); crossed-polarized light

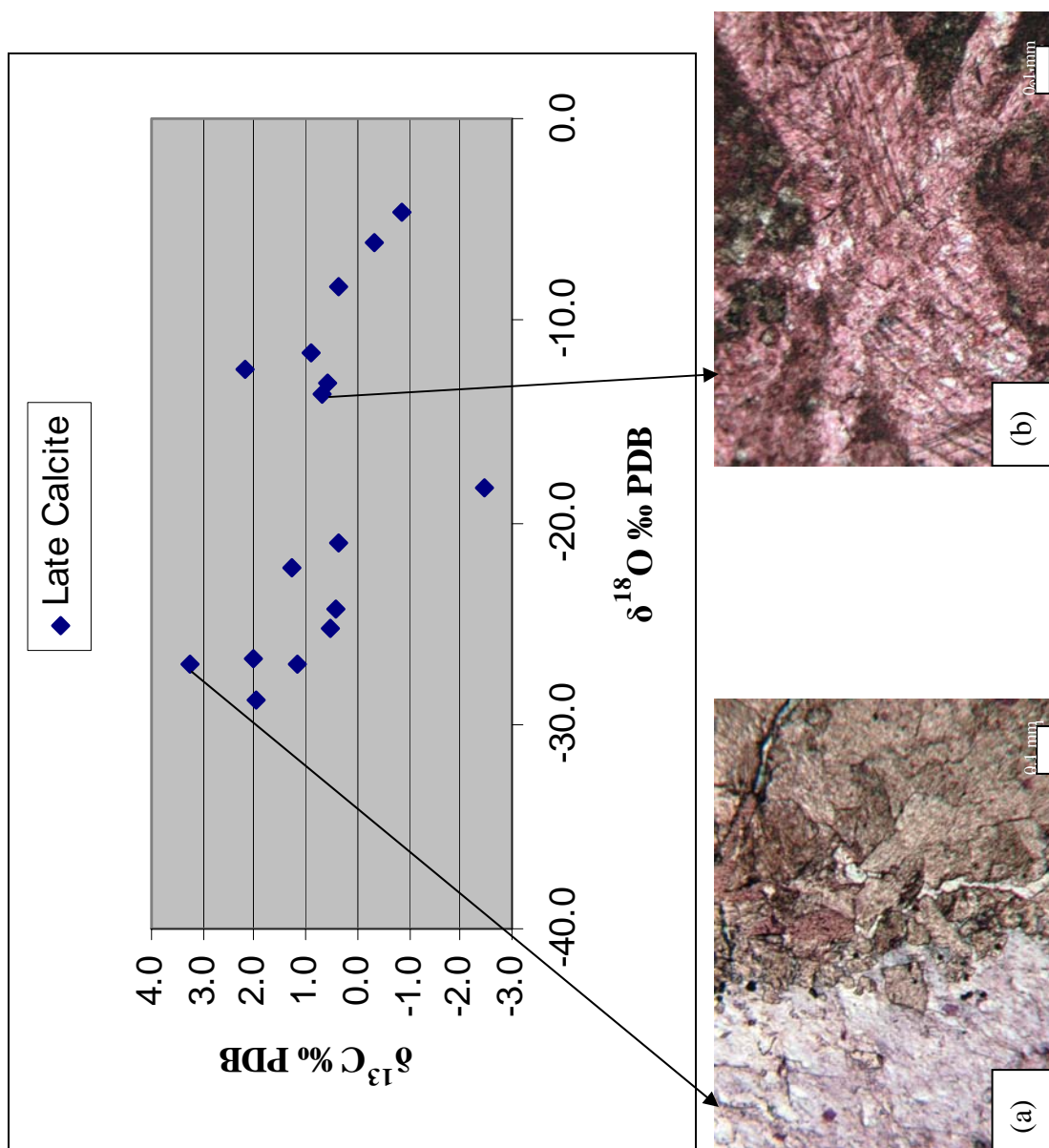


Figure 47

described by Evans (2000), with drusy quartz representing the later of the two. The quartz seems to have an important relationship to ferroan dolomite, as ferroan dolomite occurs with a high percentage of quartz. The majority of the timing relationships observed place the silicification event after ferroan dolomitization. The ferroan dolomite that occurs near quartz has dissolution features on the boundaries of crystals and in CL shows zoning.

### **Hydrocarbon Migration**

Bitumen is concentrated along stylolites in massive limestone and in pore spaces of dolomitized ooids; it is most evident in the samples from near Meikle, but is not recognized near Dee-Rossi or South Arturo. Timing of hydrocarbon migration may not be as well constrained as previously thought. Barnicoat et al. (2005) suggested hydrocarbon migration in the Jerritt Canyon and Screamer (directly south of Meikle on Barrick property) deposits occurred during Eocene mineralization, but Evans (2000) and Emsbo and Koenig (2005) showed paragenetic relationships that constrain hydrocarbon migration to the Paleozoic base-metal mineralization.

### **Paragenesis**

Detailed petrographic analysis provides a paragenetic sequence with respect to carbonate types and associated events (Figure 48). Early cementation of limestone is evident by the fabric of the calcite cement seen in the limestone samples and represents the first stage of diagenetic alteration of the Bootstrap limestone.

Diagenetic-planar dolomite predates and shows no genetic relationship to hydrothermal dolomitization. Diagenetic-planar dolomite is cut by stylolites, indicating it

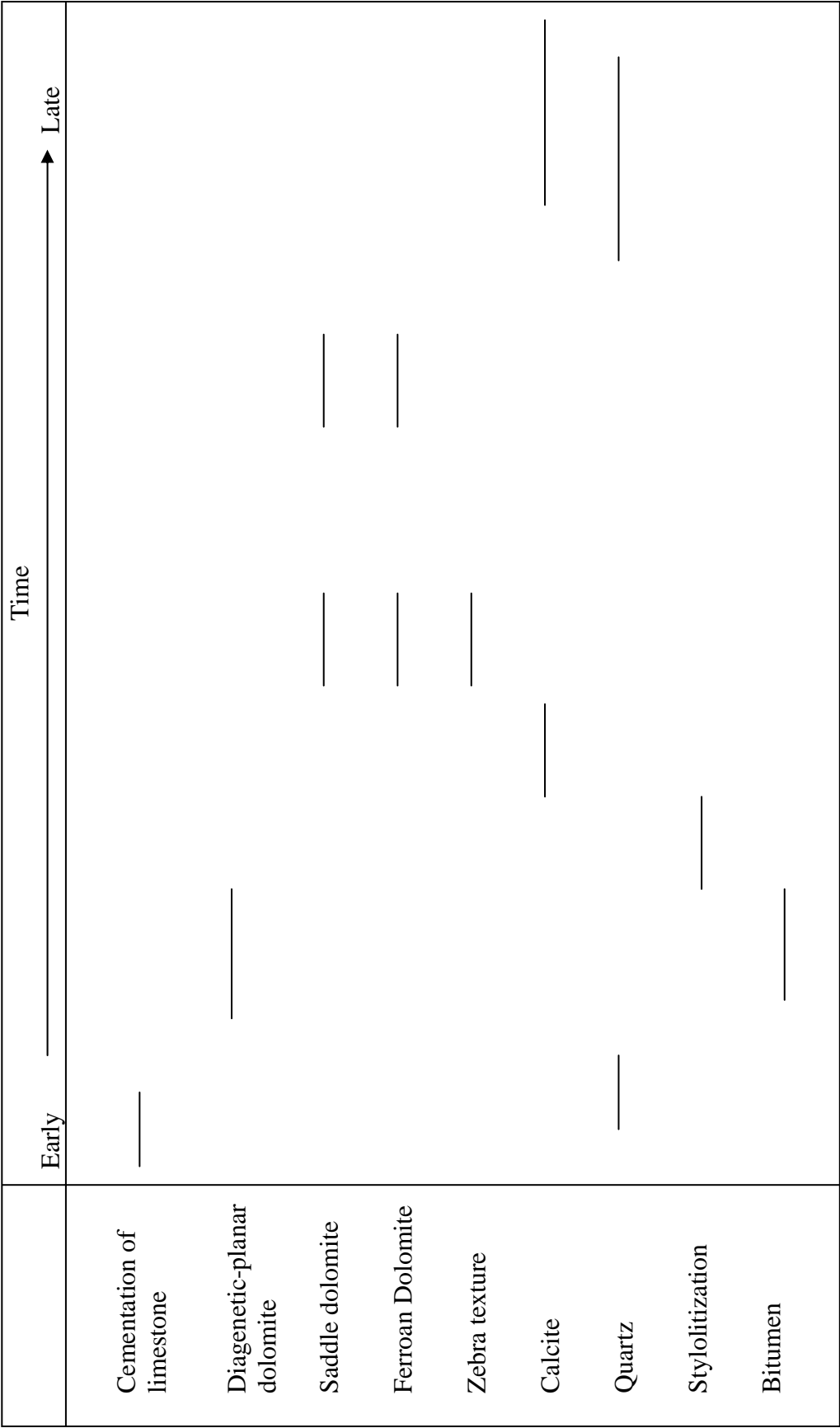


Figure 48: Paragenetic sequence of carbonate types and associated events. Time is relative to dolomitizing events, not absolute time, with early diagenesis occurring in the Mississippian. The first hydrothermal dolomite event occurs in the Paleozoic; the second hydrothermal dolomite event represents Jurassic to Tertiary time, and the late calcite event continuing until the present.



formed during an early dolomitization event. Furthermore, stylolites in the limestone and diagenetic-planar dolomite concentrate dolomite rhombs and bitumen. This relationship places hydrocarbon migration before stylolitization.

The brecciated nature of the saddle, ferroan, and zebra texture dolomite places clasts of these in sharp contact with limestone. These dolomites are destructive in nature, and saddle dolomite veins cut stylolites. The lack of stylolites and the similarity in texture and fabric of these three dolomite types constrains the timing of hydrothermal dolomitization to post-stylolitization events. The isotopic data indicate that there are two hydrothermal dolomitization events. The event associated with the saddle, ferroan, and zebra dolomites at Meikle is constrained by relationships observed by Evans (2000) to a Paleozoic base-metal mineralization event. The isotopic data for samples from near Dee-Rossi are closely related to the data for the host limestone. At the Storm Deposit (Dee-Rossi area), hydrothermal dolomite is associated with Jurassic igneous fragments in the silica-sulfide breccia that hosts ore. There also is a later brecciation event that contains Eocene basalt fragments and cross-cuts the limestone wall rock. The contact between the limestone wall rock and breccia is marked by a ferroan dolomite selvage (Dobak et al., 2002). In the Twin Creeks deposits, the iron for ferroan dolomite is interpreted to have a basaltic source (Fortuna et al., 2003). These relationships, in combination with the isotopic data, indicate a Jurassic to Tertiary hydrothermal dolomitization event at Dee-Rossi that was related to igneous activity.

Quartz and calcite both formed repeatedly through time beginning with early diagenesis. There are calcite events before and after hydrothermal dolomitization, and there are several pulses of quartz deposition after hydrothermal dolomitization as well.

### **Pattern of Dolomitization**

The areal extent of the various carbonate types was difficult to map. The areas with hydrothermal dolomites are clearly related to structures, breccia bodies, and igneous intrusions. Structural complexity and brecciation causes hydrothermal dolomitization to be recognized only in short, alternating intervals in the examined drill core. Figure 49 illustrates the distribution of limestone, dolostones, saddle dolomite, ferroan dolomite, and zebra texture dolomite as related to key drill holes in each deposit area. Distribution of the carbonate types is partially related to the original permeability of the limestone. The low porosity and permeability of the limestone prevented regional replacement of the limestone by hydrothermal dolomite. Dolomitizing fluids and late gold-bearing fluids were focused by the fabric of the limestone created by deposition and early diagenesis, and by secondary porosity in the limestone created by dissolution, brecciation, and faulting.

In the adjacent basinal rock units of the Roberts Mountains, Popovich and Rodeo Creek Formations, it can be assumed that the original porosity and permeability of the host rock was greater than in the Bootstrap limestone because of their mud-rich composition and debris flow sections. In the former units, dolomitizing fluids would have not been impeded to the same degree, allowing for a larger area over which dolomitization could occur. The age and the relationship of the units suggests that fluids responsible for dolomitizing the Bootstrap limestone were probably the same as those responsible for dolomitizing the basinal units.

For the hydrothermal dolomite types, it is predicted that if the Bootstrap had contained higher porosity and permeability at the time of Paleozoic base-metal

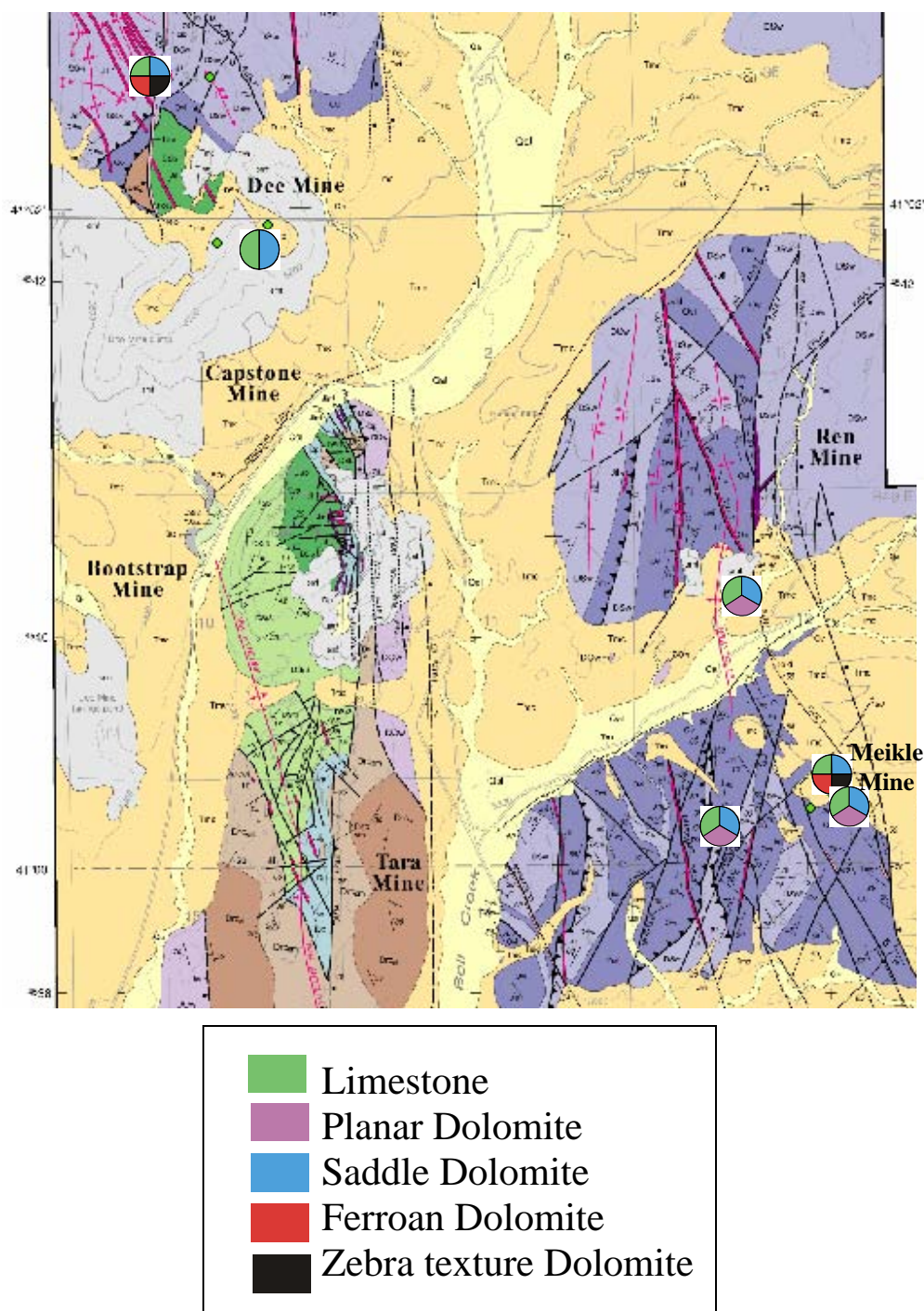


Figure 49: Map showing the occurrences of different carbonate types in key drill holes from each of the four deposits in this study. The map illustrates how restrictive the occurrence of ferroan and zebra dolomite can be. The wedges of each circle do not represent proportion of carbonate type recognized in the core, merely presence of the carbonate type.

mineralization, then the idealized dolomitization pattern away from a fluid pathways such as a fault would be as follows: ferroan dolomite, zebra texture dolomite, saddle dolomite, limestone (Figure 50). The reasoning for this pattern is that ferroan dolomite is more easily formed than saddle dolomite so the dolomitizing fluid would become quickly depleted in Fe as ferroan dolomite is formed. The depleted Fe-bearing fluid would then form saddle dolomite. If zebra texture is formed by saddle dolomite veins in ferroan dolomite, zebra texture would occur throughout ferroan dolomite. The saddle dolomite would become increasingly planar-s as the temperature of the fluid cooled and reached the farthest extent possible from the fluid pathway. This pattern would apply to the Jurassic to Tertiary hydrothermal dolomitization event as well, although the extent of dolomitization would be more limited than the dolomitization associated with the Paleozoic event. As demonstrated by samples in this study, diagenetic-planar dolomite is not recognized in areas with hydrothermal dolomite. No cross-cutting observations were made of the planar and hydrothermal dolomites, but the regional distribution of the diagenetic-planar dolomite indicates that these events were probably not time equivalent. The lack of diagenetic-planar dolomite in areas of hydrothermal dolomitization suggests that as the hydrothermal dolomitizing fluids moved through the host limestone, they must have experienced a decrease in the availability of  $Mg^{2+}$  before the fluids cooled to temperatures associated with diagenetic-planar dolomite formation.

The average isotopic values for each carbonate type show the relationships between all the carbonate types (Figure 51). The difference between limestone and dolomite falls within the anticipated 2 to 4‰  $\delta^{18}O$  enrichment described by Land (1980) and McKenzie (1984). Carbonate phases with negative  $\delta^{13}C$  values reflect carbon derived

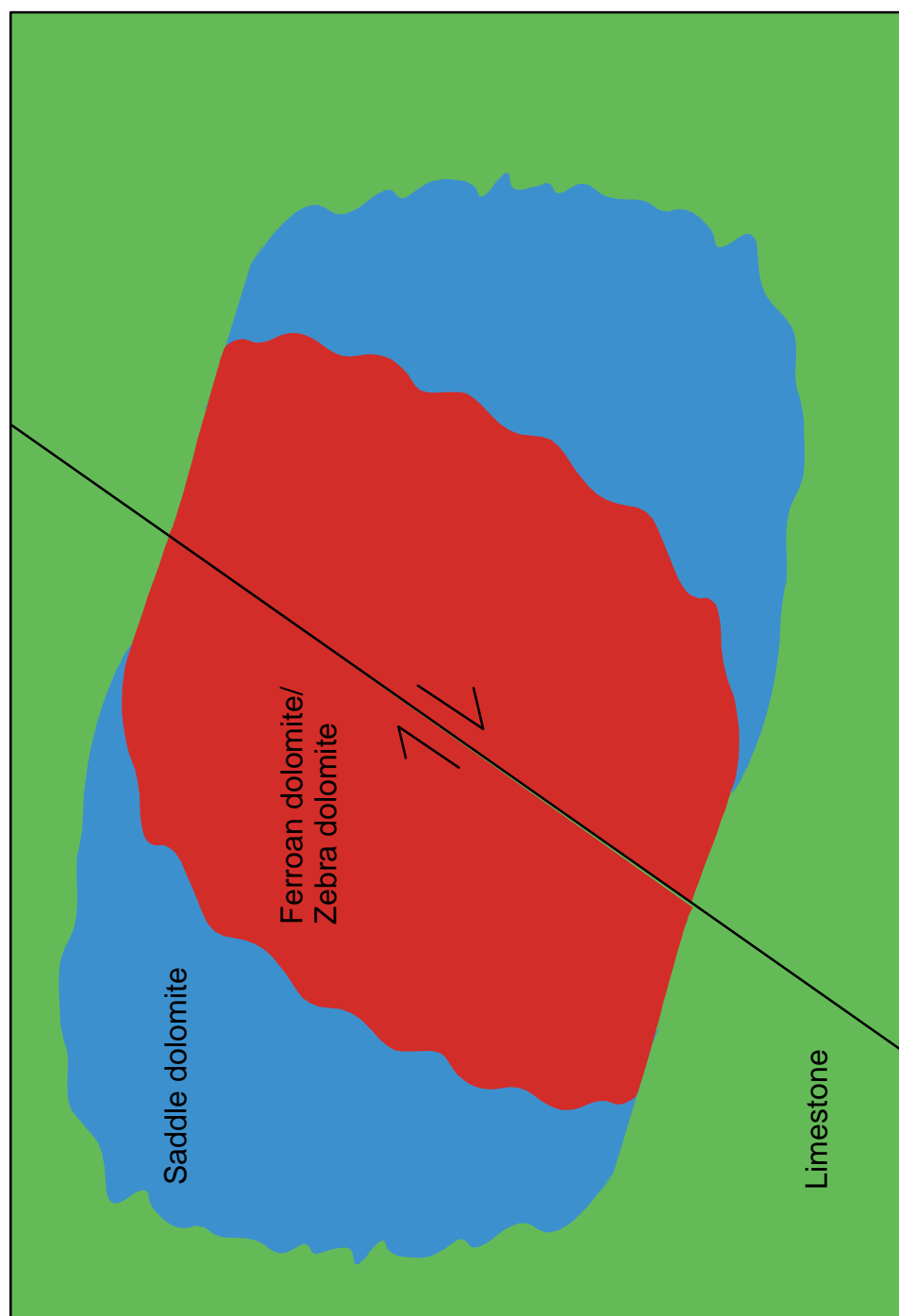


Figure 50: Schematic diagram illustrating the interpreted zonation of hydrothermal dolomitization away from a fault or other fluid pathway. The fluids are transported along a structure and then flow laterally through limestone with ferroan dolomite forming first, followed by saddle dolomite. If zebra texture is related to the veining of ferroan dolomite, then the zebra texture could develop at the transition between saddle and ferroan dolomite or extend throughout the entire ferroan dolomite halo.

Figure 51: Combined isotopic data for all carbonate types. The values plotted are the average end-member values for each type with the range of values marked by black lines extending from the average value. Saddle dolomite, ferroan dolomite, and zebra texture dolomite are separated into the average values for samples near Meikle and Dee-Rossi. The data show the burial trend from limestone to planar dolomite (yellow arrow) and the differences in  $\delta^{18}\text{C}$  values for samples from Dee-Rossi to samples from near Meikle (green arrow). The burial trend fits the anticipated 2 to 4 ‰  $\delta^{18}\text{O}$  enrichment predicted by Land (1980) and McKenzie (1982) for dolomite replacement of limestone. The trend from Dee-Rossi area to Meikle reflects depletion of  $\delta^{18}\text{C}$  values related to decomposition of organic matter and probably represents two separate dolomitization events.

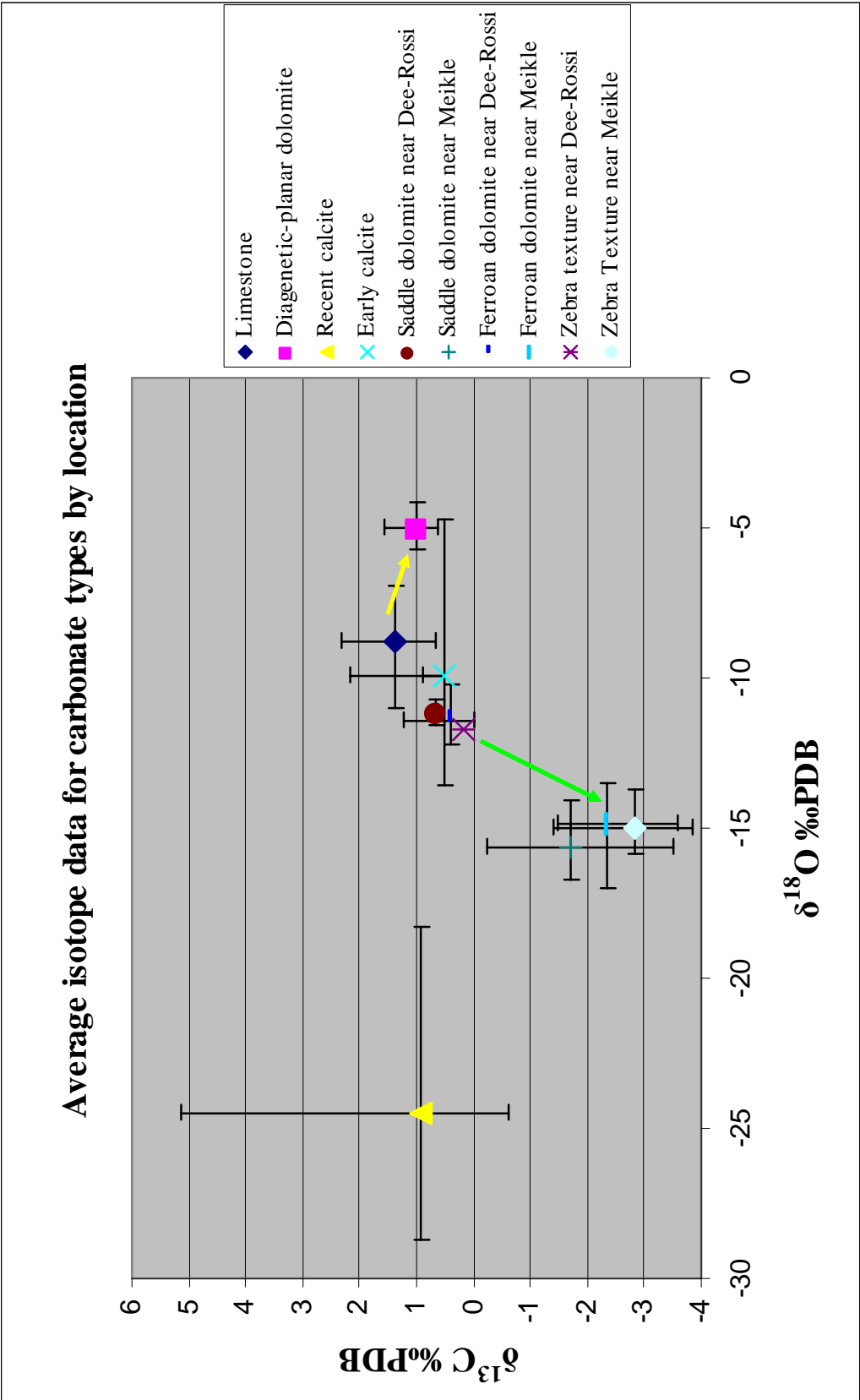


Figure 51

from decomposition of organic matter, whereas normal marine values are 0 to 3‰  $\delta^{13}\text{C}$  (Hoefs, 1997). On the plot of isotopic values, saddle dolomite, ferroan dolomite, and zebra dolomite are divided into two groups: samples near Dee-Rossi and samples near Meikle. This clearly shows the depletion of  $\delta^{13}\text{C}$  values in the area of Meikle. This reflects the high proportion of organic matter observed in that area. The organic matter is available for sulfate reduction, which, in turn, can drive dolomitization. The presence of organic matter, therefore, can influence the amount and/or ease of ferroan dolomitization. Ferroan dolomite, in turn, provides the Fe that reacts with sulfur in the gold-bearing fluids to form pyrite. The removal of reduced sulfur from the mineralizing fluid causes gold to deposit as the dissolved gold bisulfide complexes become unstable (Fortuna et al., 2003). Depleted  $\delta^{13}\text{C}$  values represent the Paleozoic base-metal event that is not well-developed in the area of Dee-Rossi. Therefore, the base-metal event influences the availability of Fe which partially controls the grade of gold deposits and it can be estimated that areas that experience the base-metal event will have greater potential to host large gold deposits



## SUMMARY AND CONCLUSIONS

The influence of different carbonate rock types on gold deposition in the Bootstrap limestone began with early diagenesis. Early cementation of the limestone decreased both the porosity and permeability, which created a unit that restricted fluid flow. Dolomitizing fluids were active at least three times. The first dolomitization event was due to a relatively low-temperature fluid (55 to 60°C) related to burial and compaction that dolomitized lower portions of the Bootstrap limestone on a regional scale. The second dolomitizing fluids were hydrothermal in nature and they directly dolomitized limestone near areas of increased porosity and permeability, such as faults and/or breccias. These fluids were responsible for a Paleozoic base-metal event. The third dolomitizing event is a hydrothermal fluid associated with Jurassic to Tertiary igneous activity in the region.

Separation of these events is possible from stable isotopic data. Values for the limestone and early, diagenetic-planar dolomite support a burial-compaction model for dolomite formation. Isotopic values for saddle dolomite, ferroan dolomite, and zebra texture dolomite samples are similar, indicating a similar fluid compositions and temperatures for the formation of all three. The  $\delta^{13}\text{C}$  values for saddle, ferroan, zebra texture dolomite samples near Dee-Rossi are similar and represent dolomitization associated with igneous activity.

The isotopic data, in combination with petrographic descriptions, also indicate a clear relationship at Meikle between hydrocarbons, well-developed hydrothermal dolomites, and a Paleozoic base-metal event. This relationship reflects the positive influence hydrocarbons and base-metal mineralization have on dolomitization. The

increase in dolomitization may also play a role in the size of the gold deposits with greater amounts of gold precipitation possible in areas that are more completely dolomitized. This is related to the concept that the higher the amount of Fe that is available for ferroan dolomite formation, the more it substitutes for Mg and distorts the crystal lattice; thus, there is more Fe available for sulfidation and resulting gold deposition. The extent of the Paleozoic base-metal related dolomitization is greater than the igneous-related dolomitization.

The data collected in this study, along with known properties of dolomitization, reveal a possible dolomitization pattern for Carlin-type gold deposits in the Bootstrap limestone or equivalent massive limestone units. Observations of the various hydrothermal dolomite phases indicate an outward change from the fluid source (a fault, fracture, or breccia) of ferroan dolomite to zebra texture dolomite to saddle dolomite, and finally to limestone.

Exploration strategies for Carlin-type gold deposits hosted in massive limestone should include considerations of the possible dolomitization methods discussed in this study. Diagenetic-planar dolomite has the largest distribution, but has no correlation to later gold mineralization. Saddle, ferroan, and zebra texture dolomites can all host gold mineralization. However, it is the hydrothermal dolomites associated with the Paleozoic base-metal event that are the most favorable hosts for gold mineralization because they can contain higher concentrations of Fe for later sulfidation than the hydrothermal dolomite associated with Jurassic to Tertiary igneous events. The presence of well-developed zebra dolomite is the best way to recognize the Paleozoic event in core. Otherwise, the degree of curvature of the dolomite crystals may separate Paleozoic and

Jurassic to Tertiary events, with the more curved boundaries representing the Paleozoic event. Isotopic values can also be a useful tool in identifying the dolomite events. The characteristics most useful in identifying the different dolomite types in core, thin-section, and isotopically are listed in Table 2. The Paleozoic dolomites will be depleted in  $\delta^{13}\text{C}$  and the Jurassic to Tertiary dolomites will have values similar to the limestone host rock.

Table 2: This table summarizes the three generations of dolomite: diagenetic-planar dolomite, Paleozoic hydrothermal dolomite, and Jurassic-Tertiary hydrothermal dolomite. Described and illustrated by photos are the most common properties used for recognizing each dolomite in core and thin-section as well as average isotopic values. The potential for each dolomite type as a host for gold mineralization is also listed with deposit examples.

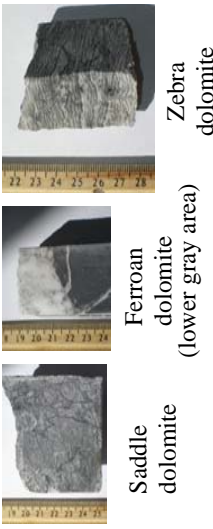

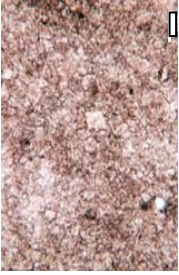


	Diagenetic-planar dolomite	Paleozoic hydrothermal dolomite (MVT related)	Jurassic-Tertiary hydrothermal dolomite (igneous related)
Core	Massive, medium gray, fossils less common in the diagenetic dolomite than limestone, but otherwise very similar to limestone, best distinguished by HCl	Off-white to gray in color Well-developed zebra dolomite (continuous banding) 	Off-white to gray to pink, pervasively fractured Poorly-developed zebra dolomite (discontinuous thin bands) 
Thin-section	Planar-e crystal boundaries 	Non-planar crystal boundaries, strong sweeping extinction under cross-polarized light 	Planar-s crystal boundaries; weak sweeping extinction under cross polarized light 
Isotope values	$\delta^{18}\text{O}$ average = -5.0 ‰PDB $\delta^{13}\text{C}$ average = 1.0 ‰PDB	Average of all 3 Paleozoic hydrothermal dolomite types: $\delta^{18}\text{O} = -15.2$ ‰PDB $\delta^{13}\text{C} = -2.3$ ‰PDB	Average of all 3 Jurassic-Tertiary hydrothermal dolomite types: $\delta^{18}\text{O} = -11.4$ ‰PDB $\delta^{13}\text{C} = 0.4$ ‰PDB
Mineralization potential	Low	High Example: Meikle	Moderate-high Example: Storm

Table 2

## REFERENCES CITED

- Arehart, G.B., Foland, K.A., Naeser, C.W., and Kesler, S.E., 1993,  $^{40}\text{Ar}/^{39}\text{Ar}$ , K/Ar, and fission track geochronology of sediment-hosted disseminated gold deposits at Post/Betze, Carlin trend, northeastern Nevada: *Economic Geology*, v. 88, p. 622-646.
- Arehart, G.B., Chakurian, A.M., Tretbar, D.R., Christensen, J.N., McInnes, B.A., and Donelick, R.A., 2003, Evaluation of radioisotope dating of Carlin-type deposits in the Great Basin, western North America, and implication for deposit genesis: *Economic Geology*, v. 98, p. 235-248.
- Armstrong, A.K., and Ward, P.L., 1991, Evolving geographic patterns of Cenozoic magmatism in the North American Cordillera: The temporal and spatial association of magmatism and metamorphic core complexes: *Journal of Geophysical Research*, v. 96, p. 13,201-13,224.
- Armstrong, A.K., Theodore, T.G., Oscarson, R.L., Kotlyar, B.B., Harris, A.G., Bettles, K.H., Lauha, E.A., Hipsley, R.A., Griffin, G.L., Abbott, E.W., and Cluer, J.K., 1998, Preliminary facies analysis of Silurian and Devonian autochthonous rocks that host gold along the Carlin trend, Nevada: U.S. Geological Survey Open-File Report 98-338, p. 38-68.
- Baker, P.A. and Kastner, M., 1981, Constraints on the formation of sedimentary dolomites: *Science*, v. 213, p. 214-216.
- Bakken, B.M., and Einaudi, M.T., 1986, Spatial and temporal relations between wall rock alteration and gold mineralization, main pit, Carlin gold mines, Nevada, U.S.A., *in* Macdonald, A.J., ed., *Proceedings of Gold '86, an International Symposium on the Geology of Gold*: Toronto, Canada, Konsult International, p. 388-403.
- Barnicoat, A.C., Phillips, G.M., Walshe, J.L., Lawrence, S.R., and Kenyon, A.K., 2005, Carbonaceous matter and gold in Carlin deposits: How intimate was the relationship, *Goldschmidt Conference Abstracts, Carbon and Gold*, p. A123.
- Barrick Gold Corporation, 2005, Barrick Goldstrike mine tour—November 2005: Internal Company Presentation.
- Barton, M.D., 1990, Cretaceous magmatism, metamorphism, and metallogeny in the East-Central Great Basin: *Geological Society of America Memoir*, v. 174, p. 283-302.
- Cantrell, D.L., and Walker, K.R., 1985, Depositional and diagenetic patterns, ancient oolite, Middle Ordovician, eastern Tennessee: *Journal of Sedimentary Petrology*, v. 55, p. 518-531.

- Cline, J.S., and Hofstra, A.H., 2000, Ore fluid evolution at the Getchell Carlin-type gold deposit, Nevada, USA: *European Journal of Mineralogy*, v. 12, p. 195-212.
- Cline, J.S., Hofstra, A.H., Muntean, J.L., Tosdal, R.M., and Hickey, Kenneth A., 2005, Carlin-type gold deposits in Nevada: Critical geologic characteristics and viable models, *in* Hedenquist, J.W., Thompson, J.F.H, Goldfarb, R.J., Richards, J.P., eds., *Economic Geology One Hundredth Anniversary Volume: Economic Geology*, v. 100, p. 451-484.
- Dobak, P.J., Arbonies, D., Hipsley, R., and Visser, M., 2002, Geology of the Storm gold deposit, *in* Thompson, T.B., Teal, L., Meeuwig, R.O., eds., *Gold Deposits of the Carlin Trend: Nevada Bureau of Mines, Bulletin 111*, p. 46-53.
- Drews-Armitage, S.P., Romberger, S.B., and Whitney, C.G., 1996, Clay alteration and gold deposition in the Genesis and Blue Star deposits, Eureka County, Nevada: *Economic Geology*, v. 91, p. 1383-1393.
- Dunham, R.J., 1962, Classification of carbonate rocks according to depositional texture: *American Association of Petroleum Geologists Memoir*, p. 108-121.
- Emsbo, P., 1999, Origin of the Meikle high-grade gold deposit from the superposition of late Devonian sedex and mid-Tertiary Carlin-type gold mineralization: Unpublished Ph.D. thesis, Golden, Colorado, Colorado School of Mines, 394 p.
- Emsbo, P., 2000, Gold in sedex deposits: *Reviews in Economic Geology*, v. 13, p. 427-437.
- Emsbo, P., Hofstra, A.H., Lauha, E.A., Griffin, G.L, and Hutchinson, R.W., 2003, Origin of high-grade gold ore, source of ore fluid components, and genesis of the Meikle and neighboring Carlin-type deposits, Northern Carlin Trend, Nevada: *Economic Geology*, v. 96, p.1069-1106.
- Emsbo, P., and Koenig, A.E., 2005, Discovery and significance of gold-rich bitumen in the Rodeo Deposit, northern Carlin trend, Nevada, *Goldschmidt Conference Abstracts, Carbon and Gold*, p. A123.
- Evans, J.G., 1980, Geology of the Rodeo Creek and Welches Canyon quadrangles, Eureka County, Nevada: *U.S. Geological Survey Bulletin 1473*, 81 p., 1:24,000 scale.
- Evans, D.C., 2000, Carbonate-hosted breccias in the Meikle mine, Nevada and their relationship with gold mineralization: Unpublished M.S. thesis, Golden, Colorado, Colorado School of Mines, 266 p.

- Farquharson, G., von Guttenberg, R., and Lechner, M., 2004, Technical report on the Ren property, Nevada for Centerra Gold Inc.: Strathcona Mineral Services Limited, 79 p.
- Fontboté, L., and Amstutz, G.C., 1983, Facies and sequence analysis of diagenetic crystallization rhythmites in strata-bound Pb-Zn-(Ba-F) deposits in the Triassic of central and southern Europe, *in* Schneider, H.J., ed., *Mineral Deposits of the Alps and of the Alpine Epoch in Europe*: Springer-Verlag, Berlin, p. 347-358.
- Fortuna, J., Kesler, S.E., and D.P., Stenger, 2003, Source of iron for sulfidation and gold deposition, Twin Creeks Carlin-type deposit, Nevada: *Economic Geology*, v. 98, p. 1213-1224.
- Friedmann, I., and O'Neil, 1977, Compilation of stable isotope fractionation factors of geochemical interests, *in* Fleisher, M., ed., *Data of Geochemistry*, Sixth ed., chapter KK, 12 p.
- Furley, R.A., 2001, Sequence stratigraphic framework for the Silurian-Devonian bootstrap limestone, Roberts Mountains, and Devonian Popovich formations, northern Carlin trend, Elko and Eureka counties, Nevada, Unpublished M.S. thesis, Golden, Colorado, Colorado School of Mines, 194 p.
- Gao, G, 1993, The temperature and oxygen-isotope composition of early Devonian waters: *Nature*, v. 361, p. 712-714.
- Henry, C.D., and Boden, D.R., 1998, Eocene magmatism: the heat source for Carlin-type gold deposits of northern Nevada: *Geology*, v. 26, p. 1067-1070.
- Hipsley, R., Dobak, P., and Arbonies, D., 2007, South Arturo, Nevada (abs), Society for Mining, Metallurgy, and Exploration Annual Meeting Proceedings.
- Hoefs, J., 1997, *Stable Isotope Geochemistry*, Springer-Verlag, Berlin, 201 p.
- Hofstra, A.H., Snee, L.W., Rye, R.O., Folger, H.W., Phinisey, J.D., Loranger, R.J., Dahl, A.R., Naeser, C.W., Stein, H.J., and Lewchuk, M., 1999, Age constraints on Jerritt Canyon and other Carlin-type gold deposits in the western United States—relationship to Mid-Tertiary extension and magmatism: *Economic Geology*, v. 94, p. 769-802.
- Hofstra, A.H. and Cline, J.S., 2000, Characteristics and models for Carlin-type gold deposits: *Reviews in Economic Geology*, v. 13, p. 163-220.
- Horton, Jr., R.A., and Devoto, R.H., 1990, Dolomitization and diagenesis of the Leadville Limestone (Mississippian) central Colorado, *in* Beatty, D.W., Landis, G.P., and Thompson, T.B., eds., *Carbonate-hosted sulfide deposits of the central Colorado Mineral Belt*, *Economic Geology Monograph* 7, p. 86-107.



- Ilchik, R.P., and Barton, M.D., 1997, An amagmatic origin of Carlin-type gold deposits: *Economic Geology*, v. 92, p. 269-288.
- James, N. P., and Choquette, P. W., 1990, Carbonate diagenesis on the modern and ancient sea floor, meteoric diagenesis and diagenesis in the zone of mixed waters: The Development of Porosity in Carbonate Reservoirs, Short Course Notes, p. 1.1-1.63.
- John, D.A., Hofstra, A.H., and Theodore, T.G., 2003, A special issue devoted to gold deposits in northern Nevada: Part 1. Regional studies and epithermal deposits. Preface: *Economic Geology*, v. 98, p. 225-234.
- Johnston, M.K., and Ressel, M.W., 2004, Controversies on the origin of world-class gold deposits, Pt. I: Carlin-type gold deposits in Nevada, II. Carlin-type and distal disseminated Au-Ag deposits: Related distal expressions of Eocene intrusive centers in north-central Nevada: *Society of Economic Geologists Newsletter* 59, p. 12-14.
- Jory, J., 2002, Stratigraphy and host-rock controls of gold deposits of the northern Carlin trend, *in* Thompson, T.B., Teal, L., Meeuwig, R.O., eds., *Gold Deposits of the Carlin Trend: Nevada Bureau of Mines, Bulletin 111*, p. 20-34.
- Ketner, K.B., 1977, Late Paleozoic orogeny and sedimentation, southern California, Nevada, Idaho, and Montana, *in* Stewart, J.H., Stevens, C.H., and Fritsche, A.E., eds., *Paleozoic paleogeography of the western United States: Pacific Section*, Society of Economic Paleontologists and Mineralogists, Pacific Coast Paleogeography Symposium 1, p. 363-369.
- Kuehn, C.A., and Rose, A.R., 1992, Geology and geochemistry of wall-rock alteration at the Carlin gold deposit, Nevada: *Economic Geology*, v. 87, p. 1697-1721.
- Land, L.S., 1980, The isotopic and trace element geochemistry of dolomite: the state of the art, *in* Concepts and models of dolomitization, Society of Economic Paleontologists and Mineralogists, Special Publication, no. 28, p. 87-110.
- Land, L.S., 1983, The application of stable isotopes to studies of the origin of dolomite and to problems of diagenesis of clastic sediments, *in* Arthur, M.A., and Anderson, T.F., eds., *Stable Isotopes in Sedimentary Geology*, Society of Economic Paleontology, Mineralogy Short Course No. 10, 4.1-4.22.
- Leach, D.L., Viets, J.G., Kozlowski, A., and Kibitlewski, S., 1996, Geology, geochemistry, and genesis of the Silesia-Cracow zinc-lead district, southern Poland, *in* Sangster, D.F., ed., *Carbonate-Hosted Lead-Zinc Deposits: Society of Economic Geologists, Special Publication No. 4*, p. 144-170.

- Lippman, F., 1973, *Sedimentary Carbonate Minerals*, Springer-Verlag, Berlin, 228 p.
- Lubben, J., 2004, Quartz as clues to paragenesis and fluid properties at the Betze-Post deposit, northern Carlin trend, Nevada: Unpublished M.S. thesis, Las Vegas, University of Nevada, 155 p.
- Machel, H.G., 2004, Concepts and models of dolomitization: a critical reappraisal, *in* C.J.R., Rizzi, G., and Darke, G., eds., *The geometry and petrogenesis of dolomite hydrocarbon reservoirs*, Braithwaite, Geological Society, Special Publication 235, p. 7-64.
- Machel, H.G., 2005, Investigations of burial diagenesis in carbonate hydrocarbon reservoir rocks: *Geoscience Canada*, v. 32, p. 103-128.
- McKenzie, J., 1984, Holocene dolomitization of calcium carbonate sediments from the coastal sabkhas of Abu Dhabi, UAE: A stable isotope study: *Journal of Geology*, v. 89, p. 228-245.
- Merino, E., Canals, A., and Fletcher, R.C., 2006, Genesis of self-organized zebra textures in burial dolomites: Displacive veins, induced stress, and dolomitization: *Geologica Acta*, v. 4, p. 383-393.
- Moore, S., 2002, Geology of the northern Carlin trend, *in* Thompson, T.B., Teal, L., Meeuwig, R.O., eds., *Gold Deposits of the Carlin Trend: Nevada Bureau of Mines, Bulletin 111*, plate 1.
- Morrow, D.W., and Abercrombie, H.J., 1994, Rates of dolomitization: the influence of dissolved sulphate, *in* Purser, B.H., Tucker, M.E., and Zenger, D.H., eds., *Dolomites—A volume in honor of Dolomieu*, International Association of Sedimentologists, Special Publications, v. 21, p. 377-386.
- Muchez, P., and Viaene, W., 1994, Dolomitization caused by water circulation near the mixing zone; an example from the lower Visean of the Campine Basin (northern Belgium), *in* Purser, B.H., Tucker, M.E., and Zenger, D.H., eds., *Dolomites—A volume in honor of Dolomieu*, International Association of Sedimentologists, Special Publications, v. 21, p. 155-166.
- Nielson, P., Swennen, R., Muchezm P.H., and Keppens, E., 1998, Origin of Dinantian zebra dolomites south of Brabant-Wales Massif, Belgium: *Sedimentology*, v. 45, p. 727-743.
- Palenik, C.S., Utsunomiya, S., Reich, M., Kesler, S.E., Wang, L., and Ewing, R.C., 2004, “Invisible” gold revealed: Direct imaging of gold nanoparticles in a Carlin-type deposit: *American Mineralogist*, v. 89, p. 1359-1366.

- Poole, F.G., Stewart, J.H., Palmer, A.R., Sandberg, C.A., Madrid, R.J., Ross, Jr., R.J., Hintze, L.F., Miller, M.M., and Wrucke, C.T., 1992, Latest Precambrian to latest Devonian time; Development of a continental margin, *in* Bruchfiel, B.C., Lipman, P.W., and Zoback, M.L., eds., *The Cordilleran Orogen: Conterminous U.S.: Boulder Colorado: Geological Society of America, The Geology of North American*, v. G-3, p. 9-56.
- Purser, B.H., Brown, A., and Aissaoui, D.M., 1994, Nature, origins and evolution of porosity in dolomites, *in* Purser, B.H., Tucker, M.E., and Zenger, D.H., eds., *Dolomites—A volume in honor of Dolomieu. International Association of Sedimentologists, Special Publications*, v. 21, p. 283-308.
- Radke, B.M., and Mathis, R.L., 1980, On the formation of saddle dolomite, *Journal of Sedimentary Petrology*, v. 50, p. 1149-1168.
- Reich, M., Kesler, S.E., Utsunomiya, S., Palenik, C.S., Chryssoulis, S., and Ewing, R.C., 2005, Solubility of gold in arsenian pyrite: *Geochimica et Cosmochimica Acta*, v. 69, p. 2781-2796.
- Ressel, M.W., Nobel, D.C., Henry, C.D., and Trudel, W.S., 2000, Dike-hosted ores of the Beast deposit and the importance of Eocene magmatism in gold mineralization of the Carlin trend, Nevada: *Economic Geology*, v. 95, p. 1417-1444.
- Rimstidt, J.D., 1997, Gangue mineral transport and deposition, *in* Barnes, H.L., ed., *Geochemistry of hydrothermal ore deposits: New York, John Wiley and Sons*, p. 487-515.
- Roberts, R.J., Hotz, P.E., Gilluly, J., and Ferguson, H.G., 1958, Paleozoic rocks of north-central Nevada: *American Association of Petroleum Geologists Bulletin*, v. 42, p. 2813-2857.
- Schafer, R.W., and Wilinon, W.H., eds., *Geology and Ore Deposits of the American Cordillera, Symposium Proceedings: Geological Society of Nevada, Reno, Nevada*, p. 25-45.
- Searl, E., 1994, Synthesis of dolomite and geochemical implications, *in* Purser, B.H., Tucker, M.E., and Zenger, D.H., eds., *Dolomites—A volume in honor of Dolomieu. International Association of Sedimentologists, Special Publications*, v. 21, p. 345-360.
- Seedorff, E., 1991, Magmatism, extension, and ore deposits of Eocene to Holocene age in the Great Basin-Mutual effects and preliminary proposed genetic relationships, *in* Raines, G.L., Lisle, R.E., Schafer, R.W., and Wilkinson, W.H., eds., *Geology and Ore Deposits of the Great Basin Symposium Proceedings: Geological Society of Nevada, Reno, Nevada*, p. 133-178.

- Sibley, D.F. and Gregg, J.M., 1987, Classification of dolomite rock textures: *Journal of Sedimentary Petrology*, v. 57, p. 967-975.
- Sillitoe, R.H., and Bonham, H.F., 1990, Sediment-hosted gold deposits: Distal products of magmatic-hydrothermal systems: *Geology*, v. 18, p. 157-161.
- Stearns, N.D., Stearns, H.T., and Waring, G.A., 1935, Thermal springs in the United States: US Geological Survey Water Supply Paper, 679-B, p. 59-191.
- Stenger, D.P., Kesler, S.E., Peltonen, D.R., and Tapper, C.J., 1998, Deposition of gold in Carlin-type deposits: The role of sulfidation and decarbonation at Twin Creeks, Nevada: *Economic Geology*, v. 93, p. 201-215.
- Stewart, J.H., 1980, *Geology of Nevada*: Nevada Bureau of Mines and Geology Special Publication 4, 136 p., 1 plate.
- Teal, L., and Branham, A., 1997, Geology of the Mike gold-copper deposit, Eureka County, Nevada: Society of Economic Geologists Guidebook Series, v. 28, p. 257-276.
- Teal, L. and Jackson, M., 1997, Geologic overview of the Carlin trend gold deposits and descriptions of recent deep discoveries, *in* Vitkre, P., Thompson, T.B., Bettles, K., Carlin-type Gold Deposits Field Conference: Society of Economic Geologists Guidebook Series, v. 28, p. 3-37.
- Teal, L., and Jackson, M., 2002, Geologic overview of the Carlin trend gold deposits, *in* Thompson, T.B., Teal, L., Meeuwig, R.O., eds., *Gold Deposits of the Carlin Trend*: Nevada Bureau of Mines, Bulletin 111, p. 9-19.
- Theodore, T.G., Berger, V.I., Singer, D.A. Harris, A.G., and Stevens, C.H., 2004, Synthrusting deposition of the Pennsylvanian and Permian Strathearn Formation, northern Carlin trend, Nevada: *Sedimentary Geology*, v. 165, P. 1-28.
- Thorman, C.H., Ketner, K.B., Brooks, W.E., Snee, L.W., and Zommermann, R.A., 1991, Late Mesozoic-Cenozoic tectonics in northeastern Nevada, *in* Raines, G.L., Lisle, R.E., Schafer, R.W., and Wilkinson, W.H., eds., *Geology and Ore Deposits of the American Cordillera*, Symposium Proceedings: Geological Society of Nevada, Reno, Nevada, p. 25-45.
- Tosdal, R.M., Wooden, J.L., and Kistler, R.W., 2000, Inheritance of Nevadan mineral belts from Neoproterozoic continental breakup, *in* Cluer, J.K., Price, J.G., Struhsacker, E.M., Hardyman, R.F., and Morris, C.L., eds., *Geology and Ore Deposits, 2000: The Great Basin and Beyond*: Geological Society of Nevada Symposium Proceedings, Reno, p. 451-466.

- Tucker, M.E., and Wright, V.P., 1990, Carbonate Sedimentology, Blackwell Scientific Publications, London, 482 p.
- Uzdowski, E., 1994, Synthesis of dolomite and geochemical implications, *in* Purser, B.H., Tucker, M.E., and Zenger, D.H., eds., Dolomites—A volume in honor of Dolomieu. International Association of Sedimentologists, Special Publications, v. 21, p. 133-153.
- Volk, J.A., Lauha, E., Leonardson, R.W., and Rhan, J.E., 1996, Structural geology of the Betze-Post and Meikle deposits, Elko and Eureka Counties, Nevada, *in* Green, S.M., and Struhsacker, E., eds., Geology and Ore Deposits of the American Cordillera, Field Trip Guidebook Compendium, p. 180-194.
- Wallace, M.W., Both, R.A., Ruano, S.M., Hach-Ali, P.F., and Lees, T., 1994, Zebra textures from carbonate-hosted sulfide deposits: sheet cavity networks produced by fracture and solution enlargement: Economic Geology, v. 89, p. 1183-1191.
- Wells, M.L., and Mullins, T.E., 1973, Gold-bearing arsenian pyrite determined by microprobe analysis, Cortez and Carlin gold mines, Nevada: Economic Geology, v. 68, p. 187-201.
- White, D.E., 1957, Thermal waters of volcanic origin: Geological Society of America Bulletin, v. 68, p. 1637-1658.
- Ye, Z., Kesler, S.E., Essene, E.J., Zohar, P.B., and Borhauer, J.L., 2002, Relation of Carlin-type gold mineralization to lithology, structure and alteration: Screamer zone, Betze-Post deposit: Mineralium Deposita, v. 38, p. 22-38.
- Zoback, M.L., McKee, E.H., Blakely, R.J., and Thompson, G.A., 1994, The Northern Nevada rift: Regional tectonomagmatic relations and middle Miocene stress direction: Geological Society of America Bulletin, v. 106, p. 371-382.

## APPENDIX A –GEOLOGIC MAP

Appendix A is located on the CD and contains the GIS files for the complete geologic map of the northern Carlin trend (Moore, 2002).

## APPENDIX B--DATA

Appendix B is a spread sheet of the log data collected during this study. The spread sheet is divided into B.1 and B.2. Appendix B.1 contains drill holes that were examined only in the available logs and photos. Appendix B.2 consists of the drill holes containing core that was logged in detail for this study.

Appendix B.1

Drill-hole	Northing	Easting	XUTM	YUTM	Elev	Top contact of Bootstrap limestone	Popovich Formation present	Ferroan Dolomite present	Dolomite present	Karst features present CB = collapse breccia CF = cavity fill	Nature of the top Bootstrap contact
BD-1	291628.7	271428.3	549428.17	4543208.44	5695		No, no rc	No	No	CB	
BD-11C	291492.3	272374.4	549717.08	4543171.57	5627.1		No, no rc	No	No	CF/CB	
BD-12c	291013.1	272052.8	549621.46	4543023.99	5584.8		Yes	No	No	CF	
BD-13	291978.7	272363.7	549711.41	4543319.69	5649		No, No			CF, mud matrix, bs clasts, ml, lm sil. Clasts	
BD-14cw	291977.2	271749	549524.14	4543316.21	5683.9		RC either?	No	Dol. Vnits	CB	
BD-16C	290500.1	271796	549545.77	4542866.42	5584.1		No, no RC	No	No	CF mentioned	
BD-18c	287285.4	271602.1	549502.59	4541886.07	5444.3	Yes, with sphalerite in CB?	No	No	No	CF, CB mentioned frequently	
BD-19c	291813.2	270214.2	549057.36	4543258.64	5833.3		Yes, over 100'	No		CF	Breccia on top of bs
BD-2	290397.3	271104.6	549335.64	4542831.69	5644		No				
BD-22	291674.2	268502.1	548536.44	4543207.83	5940.8		No	No	No	CF?	Breccias and Intrusives
BD-25	291700	267530	548240.16	4543210.88	5800		Maybe	No	Yes		Breccia with bs
BD-26	291520	268055	548400.99	4543158.65	5880		No	No	Yes in breccia		
BD-27	290800	268730	548610.19	4542942.62	5870		No	No	Yes, next in intrusives		
BD-28	291520	268065	548404.03	4543158.69	5880		No	Yes, weak in breccia	Yes, in breccia		
BD-30	291815	272220	549668.44	4543269.12	5700		No	No	No		
BD-31	291408.8	268190	548442.67	4543125.43	5879.8		No	No	No		
BD-32	291142.2	268335.6	548488.35	4543044.92	5900.1		No	No	No		



Appendix B.1 continued													
BD-34	291266	268249.2	548461.42	4543082.21	5902	1020	No	No	CF				
BD-35	290916.5	268439.7	548521.18	4542976.68	5887.7	990	No	In breccia				35' breccia on top of bs	
BD-40	291525	268055	548400.97	4543160.17	0	N/A							
BD-41	291160	268190	548443.9	4543049.63	5860	1170	No	No					
BD-42	290620	268415	548515.12	4542886.23	5820	915	No	No					
BD-43c	293400	264900	547430.5	4543715.79	5820	2628	No	No				Small amount breccia on top bs	
BD-45	291545	268065	548403.91	4543166.3	5880	(only 5' breccia this time)	No	No					
BD-48	290450	268340	548493.12	4542834.07	5794.8	875 20'						CF-850-875 described as poor recovery	
BD-49	290809.41	268290.97	548476.39	4542943.32	5850								
BD-51	291015	268845	548644.18	4543008.69	5872.2	925 20'	No						
BD-52	291510	268400	548506.14	4543157.3	5966.89	1253 no	Yes						
BD-54	291210	268430	548516.77	4543066.06	5960		Yes in the RC?		CF			Breccia on top of bs	
BD-57	291515	268400	548506.12	4543158.82	5980	1200	Yes	Yes				Breccia on top of bs	
BD-5c	291767.7	271988.6	549598.18	4543253.57	5710.2	1250--breccia	No	No					
BD-63	288475.6	272495.9	549769.02	4542253.1		maybe some in breccia	Zebra clasts in breccia		"Sandy fill", lots of no recovery in this hole--voids?				
BD-67	288218.2	271801	549558.58	4542171.24	5454.4	In and out in breccia							
BD-68	288986.5	271799.2	549554.23	4542405.3	5495.2	1705, starts in breccia either	no? no rc	In breccia maybe					
BD-69	289560	271600	549490.7	4542579.04	5500	1665	No rc either, maybe some rc in breccia	No					
BD-70	288640	271600	549495.26	4542298.76	5500	1985, all in breccia listed	Perhaps, but not listed	Weak	CF mentioned				

Appendix B.1 continued													
BD-71	287940	272275	549704.36	4542088.83	5460	N/A	N/A						
BD-8 c	291102.5	272807	549850.79	4543054.95	5517.1	N/A							
BD-200	0	0	468175.44	4453039.8	0	438	No	No	CF				Breccia on top of BS
BO341	289175	268572	548570.1	4542446.77	5875.6	Mixed in and out of Bootstrap and Vininni beccia							
BRS-1	295172	268599	548548.66	4544273.94	6023	2567	Yes	No	CF				
BRS-11	292040	267475	548221.72	4543314.2	5800	1580	Maybe	Yes					Bx at RC,P,Db contact
BRS-14b	292456.91	266864.34	548033.62	4543438.19	5958.72	N/A		Yes in frags					
BRS-16	305893	268349	548419.44	4547538.96	5795	N/A		Yes, in breccia					TD in RC?
BRS-17	292145.78	266714.88	547989.62	4543342.66	5926	1790	maybe	no	CF				Breccia on top of bs
BRS-18	291800.03	266502.25	547926.55	4543236.27	5861	N/A		Yes, in breccia					TD in cavity fill
BRS-19	291840.28	267588.94	548257.42	4543253.91	5798.8	1350	Maybe						Breccia on top of bs
BRS-20	302407	265145	547460.57	4546461.05	5625	N/A							TD in pop
BRS-21	298154.19	267369.41	548159.3	4545176.41	5783	3325	Maybe	No					
BRS-22	291988.41	268065.69	548401.93	4543301.39	5915.47	3325	Maybe	No					Breccia on top of bs
BRS-23A	299630	267490	548188.74	4545626.63	5700	3755	Yes	no					No breccia on top vuggy bs
BRS-25	292160.41	266714.28	547989.36	4543347.11	5925	1925	Maybe	no					breccia on top bs
BRS-27	291862	268258	548461.15	4543263.84	5927	1280	Yes	No					Breccia on top of bs
BRS-29c	292485	267660	548275.88	4543450.68	5799.31	1705	Yes	No					No breccia at top bs
BRS-2C	294055	269208.81	548739.97	4543936.66	5982	1939	Maybe	No	CF				
BRS-3	292759.72	271682.97	549500.15	4543554.27	5615	1397	Maybe	No	CF				
BRS-31	291884	266904	548048.53	4543263.84	5868	1485	Yes	Yes					Breccia on top of bs
BRS-34	292668	267241	548147.32	4543504.37	5896	2005	Yes	No					No breccia at top bs
BRS-35	292412.8	267676.5	548281.27	4543428.77	5802.9	1600	Maybe	No	CF				
BRS-36	297213.27	272333.47	549676.31	4544914.31	5707	2790	Yes	No					Breccia at bs contact
BRS-39	303286.1	264094.63	547136.21	4546723.69	5599	3675	Yes	no					Breccia at bs contact
BRS-41	298236	265383	547553.71	4545191.5	6030	N/A		Yes					TD in pop
BRS-4C	291940.4	268193.2	548441.02	4543287.4	5920.3	1365	Maybe	No	CF				

Appendix B.1 continued														
BRS-5	292471	271358	548402.58	4543464.7	5707	1450	Maybe	No	No				Breccia on top bs	
BRS-6c	291900	267860	548339.71	4543273.44	5910	955	Maybe	No	No				Breccia on top of bs	
BRS-7	295003	266810	548004.47	4544213.61	5836	N/A							TD in RC?	
BRS-8c	292337	266696	547982.92	4543400.83	5936	2163	No	No	Yes			CF--big area on top of		
BRS-9	296966.22	269782.25	548900.27	4544826.43	5741	N/A	Yes					Bootstrap		
D93023	2290900	267877.2	537928.52	5152274.57	5640.5	615	No						TD in Pop	
DC-95-03	289616.81	266070.31	547805.75	4542568.99	5574	2738	Yes	No	No					
RS001	293108.72	2.7132E+10	500000	-9997887.29	5712.65	Maybe none (calling								
RS003	-3462	10785	471477.26	4452037.77	5709	989	Maybe	No	No				No breccia at top bs	
RS004	-2568	9212	470993.8	4452302.43	5831	N/A	Maybe							
RS010	293021.44	267564.72	548244.2	4543613.63	5850	N/A	Maybe							
RS011	292828.38	267380.88	548189.15	4543553.91	5854	N/A	Maybe							
RS012	292636.69	267559.03	548244.37	4543496.4	5810	Maybe POP								
RS013	292627.56	267362.94	548184.67	4543492.65	5864	Maybe none (calling	Maybe							
RS014	292611.16	267821.81	548324.55	4543489.92	5859	Bootstrap limey mud)								
RS015	292415	267565.94	548247.57	4543428.89	5792.65	Maybe none (calling								
RS016	292224.88	267537.13	548239.73	4543370.82	5787	Bootstrap limey mud)	1620	Maybe	No	No			No breccia at top bs?	
RS017	292424.47	267369	548187.52	4543430.8	5861	Maybe none (calling	Maybe							
RS019	292831.66	267142.88	548116.62	4543553.74	5913	Bootstrap limey mud)	Maybe							
RS024	293429.41	266963	548058.86	4543734.96	5895	N/A	Maybe							
RS025	293227.34	266967.66	548061.28	4543673.42	5914	N/A	Maybe							

Appendix B.1 continued											
RS026	292920.53	297261.75	557292.29	4543729.81	5886		2069	Maybe	No	No	Muddy Is breccia at top BS
RS027	293447.44	267377.78	548185.13	4543742.51		Probable with argillite contamination?					
RS030	292831.31	266760.67	548000.18	4543551.75	5931		2250	Maybe			No breccia
RS031	292419.5	267157.9	548123.23	4543428.24	5291.65	N/A					TD in RC?
RS032	292627.9	266171.88	547821.8	4543486.85	5829	N/A					TD in RC?
RS034	292432.38	266962.06	548063.51	4543431.19	5952	N/A					TD in cave
RS035	292644.28	266764.09	548002.14	4543494.78	5953		1830	Maybe	No	No	TB at top bs
RS036	292245.56	266940.28	548057.8	4543374.17	5934.65		2031	Maybe	No	CF with bedding	Breccia keeps BS coming in and out
RS037	294022.59	267156.25	548114.8	4543916.63	5875		2092.5	Maybe	No	No	TB at top bs
RS038	291718.28	266966.25	548068.31	4543213.67	5810.64		1513	Yes	No	No	TB at top bs
RS039	3940	8244	470667.28	4454279.99	5886	N/A					TD in RC?
RS040	292647.5	266950.13	548058.81	4543496.68	5955		2080	Maybe	No	No	TB at top bs
RS041	293137.41	237064.81	538951.68	4543498.1	5928.65	N/A					TD in RC?
RS042	291747.28	266757.5	548004.58	4543221.46	5884.65		1866	Maybe	No	No	CB
RS043	291536.75	266813.5	548022.68	4543157.6	5833.65		1717	Maybe	No	No	
RS044	291190.88	266800.19	548020.33	4543052.16	5807		1590	Maybe	No	CF	
RS047	-3496.56	8810.79	470876.11	4452017.65	5816.39	N/A		Maybe			
RS048	-3290	8811.64	470875.36	4452080.56	5863.53	N/A					
RS050	-2385.4	8713.4	470841.04	4452355.63	5937.2		2284	Maybe	No	No	CB
RS051	-3339.15	8598.3	470810.62	4452064.57	5900.17	N/A		Maybe		CB	TD in breccia with oolitic Is clasts
RS052	-1923.7	7478.9	470462.78	4452490.25	5724.9		2574	Maybe	No	No	
RS053	-3241.56	8678.18	470834.47	4452094.68	5901.4		1610	Maybe	No	No	
								Yes			
								(maybes should be yes)			No breccia above the BS
RS054	-1011.5	9028.2	470930.23	4452775.63	5948.4		2308	yes	No	No	
RS064	293450.63	267147.81	548115.07	4543742.34	5919		2247.5	Maybe	No	No	
RS066	292461.78	266395.31	547890.7	4543437.35	5893.37		2056	Maybe	No	No	
RS068	294524.41	266654.03	547959.31	4544067.03	5845		2840	Maybe	No	No	No breccia above BS

Appendix B.1 continued													
RS069	293839.19	266778.5	548000.63	4543858.88	5888	N/A	Maybe (sharp contact)	No	No				
RS074	292606.34	268220.78	548446.13	4543490.42	5927		1575	No	No				
RS075	292596.34	268641.69	548574.41	4543489.46	5823		1425	No	No				
RS076	292647.5	269043.22	548696.48	4543507.03	5768		1355	No	No				
RS077	292581.66	269445.59	548819.4	4543488.96	5891		1415	No	No	CB?			
RS078	292619.16	269812.97	548931.13	4543502.21	5966		1459	No	No	CB			
RS079	292197.81	267750.88	548304.99	4543363.64	5820		1420	No	No				
RS080	1155	13750	472357.91	4453458.49	5591		1555	No	No	CB above Bootstrap-- sphalerite			
RS081	292076.66	267870.72	548342.1	4543327.32	5866.65	N/A							
RS084	291106.94	266371.38	547890.11	4543024.47	5813	4079?	Maybe	No	Yes			No breccia above bs	
RS093	291620.88	267114.31	548113.91	4543184.72	5748.4	N/A	Yes						
RS094	292054	268016.5	548386.62	4543321.13	5908		1390	No	No	Solution cavity at top of Bootstrap			
RS096	-3100	9290	471020.14	4452140.77	5802		1285	No	Yes, below 1305			No breccia at top of bs, massive sphalerite in bs	
RS097	-3132	9297	471022.43	4452131.05	5802		1545	No	Yes			No breccia at top of bs, dolomitized though	
RS099	293226.28	266870.63	548031.72	4543672.61	5912		2335	No	No				
RS100	-3436	8380	470744.6	4452034	5915	N/A		No	No	CB			
RS101	-2069	8380	470737.95	4452450.38	5889		2365	No	No				
RS102A	292182.8	266495.65	547922.64	4543352.86	5899	N/A							
RS106	0	0	468175.44	4453039.8	0	N/A							
RS108	292290.88	267646.75	548272.8	4543391.48	5861	N/A	Maybe						
RS110	291641.5	266945.5	548062.37	4543190.17	5811.64	N/A	Maybe						
RS113	-3320	9122	470970.04	4452072.95	5781		1011	No	No				
RS114	292194.59	267983.84	548375.97	4543363.81	5892		1430	No	No	No breccia, but no recovery either			
RS116	-1829	8531	470782.78	4452524.21	5887	N/A	Yes			TD in breccia			
RS117	292407	266175	547823.85	4543419.57	5839		2343.5	No	No	TB			
RS118	-2457.2	8895.8	470896.94	4452334.64	5891.2		2101	No	No	SB			

Appendix B.1 continued

RS120	-2559.5	1201.15	471846.45	4452318.63	5882.8		1510	Maybe	No	No		No breccia at top of bs?
RS122	-2433.31	8799.87	470867.61	4452341.45	5520.08	N/A			No	No		
RS123	291649.25	267293.84	548168.47	4543194.25	5741		1070	Yes	No	No	Limestone Breccia	
RS126	2411	8803	470844.99	4453817	5920		2152	Maybe	No	No	CF	
RS127	-3392.26	8467.5	470771.04	4452047.75	5914.54		1855	Maybe	No	No	TB	
RS128	292325	266358	547880	4543395.5	5873.4	N/A		Yes				TD in breccia
RS130	-3545	8896.44	470902.43	4452003.32	5782.91		1245.8	Yes	No	No	CB with pop in it and sphalerite	
RS132	290685.31	268734.59	548612.16	4542907.7	5746		1705	Yes	No	No	Voids	
RS133	-2801.11	7592.24	470501.57	4452223.55	5772.06		2428	Yes	No	No	IB	
RS135	292808.9	265752.25	547693.06	4543539.93	5699.08		2880	Maybe	No	No	LB/IB	
RS139	290874.47	266618.88	547966.65	4542954.86	5801.6		1820	Maybe	No	No	CB?	
RS140	1940.56	7127.51	470336.94	4453665.55	5704.11	N/A		Maybe				

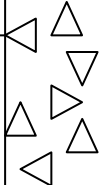
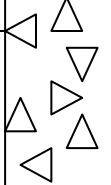
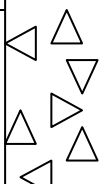
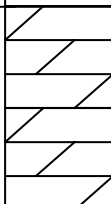

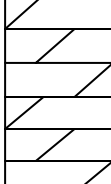
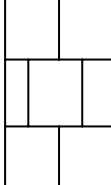

Appendix B.2												
Logged and sampled drill holes												
Hole	Northing	Easting	XUTM	YUTM	Elev	Bootstrap limestone present	Popovich Formation present	Ferroan Dolomite present	Dolomite present	Karst features present	Nature of the top Bootstrap contact	
BD-131	288289.45	269509.92	548860.22	4542181.62	5713	Yes	N/A	No	Yes	Yes		
BD-177	268465.55	268985.04	548798.31	4536139.48	5713	Yes	N/A	No	No	Yes		
BD-178	288449.59	268478.2	548545.12	4542225.31	5846.09	Yes	N/A	No	Yes	Yes		
BD-181	288764.89	269430.05	548833.55	4542326.07	5758	Yes	N/A	No	Yes	Yes		
BD-52	291510	268400	548506.14	4543157.3	5966.89		1253	Yes	Yes			
CD-16	16350.1	1799.4	548863.27	4541941.23	5451.8							
D0-100-1			548178.84	4543166.4	4888.7	Yes	N/A	Yes.	Yes			
D1-100-4			548180.84	4543180.62	4884.5	Yes	N/A	Zebra	Yes			
D2-100-2			548182.36	4543195.68	4874.6	Yes	N/A	Yes	Yes			
EX-21c	20391.7	8483.6	551988.11	4539132.46	5500.9	Yes		Yes	Yes			
GA-65c	19702.1	6291.3	551398.19	4538928.86	5521.8	Yes	Yes	No	Yes			
GB-788c	15759.1	10192	552594.72	4537735.54	5377.3		No	No	No			
MST-1	20112.8	8142	551884.6	4539046.79	5532.9				Yes			
NBC-54c	21937	8504.9	552068.04	4539614.34	5532.4	2898?		No	Yes		Breccia	
RU-8	24011.8	6623.6	551490.61	4540242.63	5436		N/A	No	Yes			
U17-M05-3	20136	8519	552076.04	4539065.68	3668	Yes	N/A	No	Yes			

## APPENDIX C—CORE LOGS

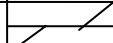
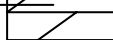
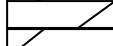
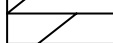
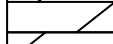
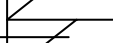
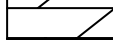
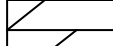
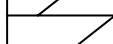
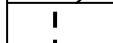


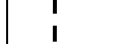
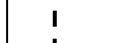
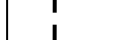
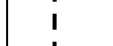
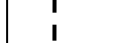
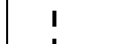
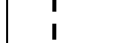
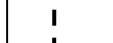



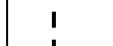
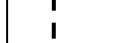
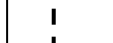
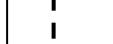
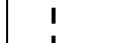
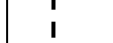
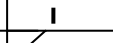
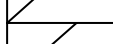
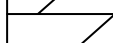
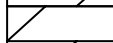
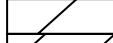
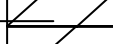
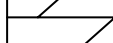

Appendix C is representative core logs constructed for the drill holes that were used in this study. The logs are generalized to show lithology, overall descriptions, and list samples taken for petrographic and isotopic analysis.



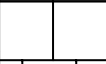
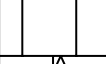






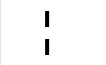
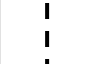

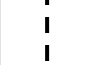

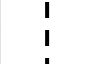
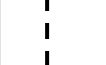
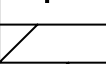
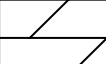
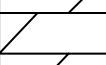
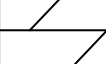
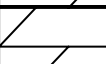
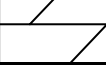
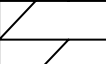
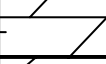
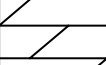
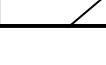



**Appendix C.4: BD-52c**

Depth (ft)	Lith	Description
1210		Silicified breccia, pyrite is present, some desilicification, box-work vugs until 1238'
1220		
1230		
1240		
		1302' Medium gray limestone with late calcite veining, dark fractures, occasional stylolites, end logging at 1340'
1300		
		
1310		
		Thin sections prepared from samples taken at 1222'; 1238.2'; 1317'


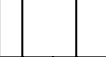
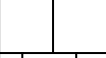
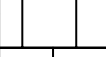
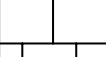
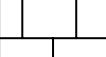
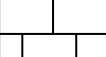

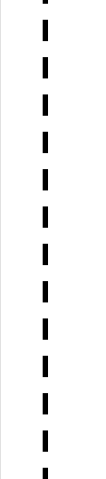
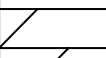
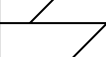
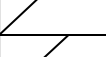
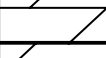
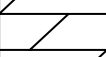
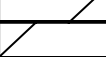
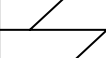
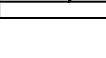
### Appendix C.3: EX-21C

Depth (ft)	Lith	Description
940		Medium gray dolomite with light red oxide, thin stylolites; core is poorly preserved and occurs in broken, small pieces Occasional monzonite porphyry intrusions about 10 ft thick
		
		
		
950		Zebra textures begins at 959' as small occurrences, dolomite and calcite veining of ferroan dolomite begins at 1013' as well as decalcification; At 1065' solid zebra dolomite with occasional areas of silicified breccia and calcite veining. Ended logging at 1280'
		
		
		
		
		
		
		
		
		
		
		
		
		
		
		
		
		
		
		
		
		
		
		
		
		
		
		
		
		
		
		
		

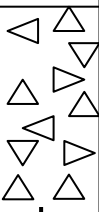
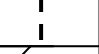
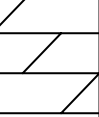




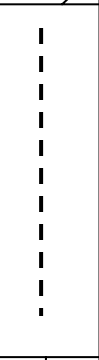


**Appendix C.1: U17-M05-3**

Depth (ft)	Lith	Description
0		Massive, medium to light gray limestone with occasional preserved crinoids and ooids; common area of brecciation; very common calcite veining and filling of vugs; occasional monzonite porphyry intrusion; occasional stylolites
		
		
		
10		
		
		
		
		
		
780		785' Medium gray dolomite with rare preservation of original ooids, occasional stylolites and fractures
		
		
		
		
		
		
		
		
		
800		Thin sections prepared from samples taken at 6, 116, 122.5, 255, 291.9, 382.9, 397.9, 405.8, 484.3, 580.9, 656.5, 732.3, 785, 820.5, 864, 898.7, 974.85, 1144, 1146.5, 1380.35', 1065', 1584', 1624, and 1845'
		
		
		
		
		
		
		
810		

**Appendix C.2: GA-65c**

Depth (ft)	Lith	Description
1620		Massive, medium to light gray limestone with occasional stylolites and common calcite veining
		
		
1630		
		
		
		
		
		
3040		3044' Medium gray dolomite with occasional stylolites, calcite veining and common areas of brecciation—ends at 3718; TD 3748'
		
		
3060		Thin sections prepared from samples taken at 1605', 1825', 2138', 2314.5', 3081', 3511.6', 3650', and 3703.7'
		
		
306		
		

### Appendix C.5: DO-100-1

Depth (ft)	Lith	Description
0		Silicified breccia with medium gray sub-angular dolomite clasts, dark gray matrix, vuggy until 48.5'
50		
60		Silicified, white dolomite with pervasive fracturing (fraction of a mm wide); stains purple; ends at 60'
60		Silicified gray breccia with occasional white dolomite areas until 103'
100		
100		103' pinky-tan dolomite with pervasive fractures with sooty fill, low quartz content, occasional stylolites; occasional pyrite-rich areas
110		140' dolomite is more gray to tan in color and more silicified, areas of brecciation, possible cavity fill, and sulfides occurring with the dark breccia
340		209' Medium gray dolomite, late calcite veining, 231' to 247' poor recovery of core, pyrite veinlets followed by massive gray dolomite until 258.5' where limestone begins to appear in sections 1 to 2 feet long and alternating with the dolomite
340		Poorly developed zebra texture at 312' with dolomite and limestone immediately below (starting at 313') ; all limestone at 344.3'
350		Thin sections prepared from samples taken at 109', 219.5', 312', and 258.5'

## APPENDIX D—STABLE ISOTOPE DATA

Appendix D consists of a spread sheet containing the  $\delta^{13}\text{C}$  and  $\delta^{18}\text{O}$  isotopic data collected in this study.

## Appendix D

Sample	Drill Hole	Depth (ft)	Lithology	$\delta^{13}\text{C}$	$\delta^{18}\text{O}$
CM 1	U17-M05-3	291.9	Limestone	-2.617	-6.060
CM 2	U17-M05-3	291.9	Dolomite	0.600	-21.842
CM 3	U17-M05-3	785	Dolomite	0.550	-11.807
CM 4	U17-M05-3	1380.35	Dolomite	0.334	-8.406
CM 5	U17-M05-3	116	Saddle Dolomite	1.006	-4.996
CM 6	D2-100-2	352.9	Limestone	-3.527	-16.132
CM 7	D2-100-2	276.4	Dolomite	2.549	-16.714
CM 8	D2-100-2	150.3	Saddle Dolomite	1.197	-24.559
CM 9	D2-100-2	150.3	Late calcite overprint	0.622	-11.596
CM 10	D2-100-2	4	Ferroan Dolomite	0.370	-21.012
CM 11	D2-100-2	266.4	Ferroan Dolomite	0.193	-11.009
CM 12	D2-100-2	266.4	Late calcite	1.141	-12.214
CM 13	GA-65c	1825	Saddle dolomite vein	3.256	-26.993
CM 14	MST-1	1214.8	Late Calcite	0.992	-11.164
CM 15	BD-177	1133.5	Limestone	-0.881	-4.688
CM 16	BD-177	1160.4	Limestone	0.798	-11.034
CM 17	GA-65c	2138	Dolomite	1.575	-6.961
CM 18	GA-65c	3081	Dolomite	0.354	-11.752
CM 19	BD-178	1436.5	Late calcite	-0.384	-9.987
CM 20	RU-8	4086	Dolomite	-0.320	-6.124
CM 21	RU-8	3520	Dolomite	1.548	-4.158
CM 22	RU-8	3520	Saddle Dolomite	1.394	-10.301
CM 23	Ex 21c	1584	Saddle Dolomite	1.133	-10.186
CM 24	NBC-54c	2976	Dolomite	0.829	-5.129
CM 25	D0-100-1	258.5	Saddle Dolomite	0.686	-10.740
CM 26	D0-100-1	258.5	Limestone	1.019	-27.378
CM 27	Ex-21	1024	Ferroan Dolomite	-2.269	-17.032
CM 28	Ex-21	1024	Ferroan Dolomite	-3.588	-14.387
CM 29	BD-52	1238.2	Ferroan Dolomite	1.229	-10.201
CM 30	D0-100-1	109	Ferroan Dolomite	-0.790	-11.996

Appendix D continued									
CM 31	D0-100-1	219.5	Ferroan Dolomite					0.197	-11.655
CM 32	D0-100-1	312	Dark Zebra					-0.231	-11.935
CM 33	D0-100-1	312	Light Zebra					-0.086	-11.486
CM 34	Ex 21c	1065	Dark Zebra					-3.550	-15.552
CM 35	Ex 21c	1065	Light Zebra					-3.304	-15.863
CM 36	RU-8	3502	Late Calcite					0.896	-11.507
CM 37	RU-8	3502	Dolomite					1.122	-8.486
CM 38	U17-M05-3	580.9	Late Calcite					0.385	-8.308
CM 39	BD-177	1133.5	Late Calcite					0.673	-13.567
CM 40	GA-65c	3703.7	Late Calcite					0.588	-13.100
CM 41	BD-131	1482	Late Calcite					1.259	-22.180
CM 42	Ex-21	1024	Saddle Dolomite					-1.809	-16.706
CM 43	U17-M05-3	116	Dolomite					-3.147	-16.238
CM 44	MST-1	1217.8	Saddle Dolomite					0.258	-14.072
CM 45	GA-65c	3081	Saddle Dolomite					0.272	-9.480
CM 46	BD-178	1436.5	Limestone					0.259	-16.695
CM 47	U17-M05-3	6	Limestone mixed with Late Cal					0.785	-10.472
CM 48	U17-M05-3	122.5	Late calcite					0.501	-25.187
CM 49	D2-100-2	260.5B	Late Calcite mix					2.159	-12.386
CM 50	U17-M05-3	656.5	Limestone and Dolomite Mix					-0.103	-6.954
CM 51	BD-181	1022	Limestone and Dolomite Mix					1.273	-21.867
CM 52	RU-8	3090	Limestone and Dolomite Mix					1.454	-5.976
CM 53	Ex 21c	1845	Limestone and Late Calcite Mix					1.166	-8.256
CM 54	MST-1	1089	Ferroan Dolomite					-1.493	-14.476
CM 55	BD-178	1318.5	Late Calcite					1.972	-28.742
CM 56	RU-8	3090	Limestone and Dolomite Mix					1.436	-6.122
CM 57	RU-8	3090	Late cal, dolomite, limestone					1.224	-6.886
CM 58*	Ex 21c	1845	Limestone and Late Calcite Mix					1.086	-8.491
CM 59*	BD-177	1160.4	Limestone					1.523	-7.175
CM 60*	U17-M05-3	656.5	Limestone and Dolomite Mix					-0.041	-6.519
CM 61	Evans (2000)	Hand sam	Holocene calcite					0.419	-24.227
CM 62	Evans (2000)	MH 17.627	Holocene calcite					1.149	-26.948
CM 63	Evans (2000)	MH-17.661	Ferroan Dolomite					-1.980	-13.501



Appendix D continued					
CM 64	Evans (2000)	MH 17,655	Light Zebra	-3.840	-13.732
CM 65	Evans (2000)	MH 17,655	Dark Zebra	-3.399	-14.103
CM 66	Hitzman	Meikle	Light Zebra	-1.592	-15.810
CM 67	Hitzman	Meikle	Dark Zebra	-1.409	-14.910
CM 68	Evans (2000)	MH 17 646	Limestone	1.621	-8.692
CM 69a	Evans (2000)	MH 17 645	Limestone	1.365	-9.020
CM 69b	Evans (2000)	MH 17 645	Limestone	1.341	-12.386
CM 70	BD-177	877	Late calcite	-2.490	-18.269
CM 71	BD-52	1317	Late calcite	1.768	-9.885
CM 72	Ex 21c	1624	Late calcite	1.220	-9.432
CM 73	GA-65c	2314.5	Limestone	2.299	-9.334
CM 74	U17-M05-3	1146.5	Dolomite	0.635	-5.727
CM 75	D2-100-2	260.5A	Late calcite	2.024	-26.635
CM 76	BD-178	1282.5	Ferroan Dolomite	1.641	-25.469
CM 77	BD-178	1282.5	Ferroan Dolomite	4.337	-25.698
CM 78	BD-178	1282.5	Limestone	0.662	-7.665

\* denotes duplicate sample

Half Range		
$\delta^{13}\text{C}$	$\delta^{18}\text{O}$	$\delta^{18}\text{O}$
1.166	1.086	-8.491
0.798	1.523	-7.175
-0.103	-0.041	-6.519

Mean Half Range	
$\delta^{13}\text{C}$	$\delta^{18}\text{O}$
0.592	0.755